UNIVERSIDADE DE SÃO PAULO
INSTITUTO DE FÍSICA DE SÃO CARLOS

Thalyta Tavares Martins

Studies of microscopic nonequilibrium stochastic dynamics in optical tweezers

São Carlos

2024

Thalyta Tavares Martins

Studies of microscopic nonequilibrium stochastic dynamics in optical tweezers

Thesis presented to the Graduate Program in Physics at the Instituto de Física de São Carlos da Universidade de São Paulo, to obtain the degree of Doctor in Science.

Concentration area: Theoretical and Experimental Physics

Advisor: Prof. Dr. Sérgio Ricardo Muniz

Corrected version
(Original version available on the Program Unit)

São Carlos
2024

I AUTHORIZE THE REPRODUCTION AND DISSEMINATION OF TOTAL OR PARTIAL COPIES OF THIS DOCUMENT, BY CONVENTIONAL OR ELECTRONIC MEDIA FOR STUDY OR RESEARCH PURPOSE, SINCE IT IS REFERENCED.

Tavares Martins, Thalyta
Studies of microscopic nonequilibrium stochastic dynamics in optical tweezers / Thalyta Tavares Martins; advisor Sérgio Ricardo Muniz - corrected version -- São Carlos 2024.
128 p.

Thesis (Doctorate - Graduate Program in Theoretical and Experimental Physics) -- Instituto de Física de São Carlos, Universidade de São Paulo - Brasil , 2024.

1. Stochastic Thermodynamics. 2. Optical Tweezers. 3. Optimal Protocols. 4. Feedback Optical Traps. 5. Classical-quantum Interface. I. Muniz, Sérgio Ricardo, advisor. II. Title.

ACKNOWLEDGEMENTS

I would like to express my gratitude to my family, especially my parents Robson and Lucia, my loved sister Maria Vallentina, my stepmother Adriana and her mother Shirley, and my grandparents Altair, João, Maria, and Baltazar, for their education, affection, love, and support in all my professional and personal choices. I would not have reached this point without all of you. I also extend my thanks to my aunts, especially Heliana and Adriana, and all my cousins for all the good moments we shared.

I also acknowledge my advisor, Sérgio Muniz, for the years of guidance, filled with patience and enthusiasm. I appreciate the discussions and assistance, the freedom I always had to choose my research interests, and the support throughout this journey. I extend my gratitude to my co-advisors, Sergio Ciliberto, Benjamin Besga, and Artyom Petrosyan, and the hospitality of ENS de Lyon for hosting me during my Exchange program. I am deeply grateful for all I learned during that time; the inspiring discussions and all assistance were crucial for finishing this doctoral research. I am thrilled to have had the opportunity to collaborate with you all.

My acknowledgements to the entire structure of IFSC: Oficina de Óptica, Oficina mecânica, Seção Técnica de Informática, and Laboratório de Instrumentação Eletrônica, especially to João, who always assisted me in several moments. I also thank Angela Giampedro, from Centro Cultural USP-São Carlos, for the careful revision of this text. This structure and those people make research at the institute viable and were crucial during my time there.

My special thanks to Prof. Leonardo Maia, Prof. Eduardo Azevedo, Prof. Sebastião Pratavieira and all members of the institute who were always available when I needed help, whether to explain things I did not understand, discuss important issues, or lend equipment whenever necessary. I always felt very welcomed at that institute because of the good people who belong to it.

I especially thank Charlie, André, and Kamizaki, who, besides friendship and support, were essential for the development of this research, from their assistance in my first steps in the laboratory to exciting discussions about physics. I also thank Pedro Paraguassu for all the theoretical support and important exchanges in the last moments of my research.

Thanks also to the friends from the laboratory - Guincho, Lilo, Gabs, Larissa, Pedro, Mário, Artur, and Brunos - and those who became part of it – Adriane (and Ruben), Rogério, Bia, Didi, Cláudio, Gustavo, Cris, Konaka, and Nicolas. The conversations, jokes, mutual support, and coffee at any time of the day were fundamental for my developing this thesis with some sanity. I would also like to thank the friends Lyon gave me and made my stay so rich - Elena, Silvia, Nicolas, Karol, Elisa, Naju, Raiza, Pedro, Tamara, Milena, Clara, P2, Carole and Lila. In light of the long list of names, I also thank the volleyball friends in São Carlos and Lyon and the old friends who, fortunately, are always close even with the physical distance - Dafny, Johnny, and Juli. Then, I could not finish the acknowledgements without thanking Aloja CAASO for welcoming me for all these last months.

Finally, I acknowledge funding agencies Capes, CNPq, and Fapesp for having financed my research since the Master's degree, and, clearly, the Brazilian people, the genuine financiers of my entire journey, which, since elementary school, has been carried out in public educational institutions.

Thank you all very much!

ABSTRACT

MARTINS, T. T. **Studies of microscopic nonequilibrium stochastic dynamics in optical tweezers**. 2024. 128p. Thesis (Doctor in Science) - Instituto de Física de São Carlos, Universidade de São Paulo, São Carlos, 2024.

This thesis addresses the development of studies on stochastic thermodynamics using optical tweezers, ranging from classical to quantum regimes. Initially, the application of out-of-equilibrium processes is explored with Brownian particles, and their thermodynamic quantities are computed through trajectories obtained from an ensemble of realizations. Microscopic thermodynamic laws and fluctuation theorems, such as Jarzynski's equality and Crooks's relation, are checked by implementing compression and expansion protocols via beam intensity control. The results show good agreement with theoretical expectations and our experimental system's robustness. Subsequently, experimental verification of optimal protocols (minimizing the average dissipated work) for trap compression and simulations for moving potentials are demonstrated. The experiments revealed the best energetic efficiency of optimal processes, i.e. they presented lower average work than linear (suboptimal) ones, which is consistent with the analytical solution. Towards efficient protocols, a feedback system was implemented for converting information to energy inspired by Maxwell's demon idea. Despite experimental challenges, feedback protocols returned lower average work values than those with no feedback, and efficiency can be explored by altering the demon's criteria. Finally, initial results are provided aiming at explorations of stochastic thermodynamics at the classical-quantum interface through investigation of trapped optically active particles (formed by quantum dots). The analysis of the particle recoil revealed that Langevin dynamics must be extended to describe our system precisely.

Keywords: Stochastic thermodynamics. Optical tweezers. Optimal protocols. Feedback optical traps. Classical-quantum interface.

RESUMO

MARTINS, T. T. **Estudos da dinâmica estocástica microscópica fora do equilíbrio em pinças ópticas**. 2024. 128p. Tese (Doutorado em Ciências) - Instituto de Física de São Carlos, Universidade de São Paulo, São Carlos, 2024.

Esta tese aborda o desenvolvimento de estudos sobre termodinâmica estocástica usando pinças ópticas, abrangendo desde regimes clássicos até quânticos. Inicialmente, a aplicação de processos fora do equilíbrio é explorada com partículas brownianas, e suas quantidades termodinâmicas são computadas através de trajetórias obtidas a partir de um conjunto de realizações. Leis termodinâmicas microscópicas e teoremas de flutuação, como a igualdade de Jarzynski e a relação de Crooks, são verificados através da implementação de protocolos de compressão e expansão via controle de intensidade do feixe. Os resultados mostram boa concordância com as expectativas teóricas e a robustez do nosso sistema experimental. Subsequentemente, é demonstrada a verificação experimental de protocolos ótimos (minimizando o trabalho dissipado médio) para compressão de armadilha e simulações para potenciais móveis. Os experimentos revelaram a melhor eficiência energética de processos ótimos, ou seja, apresentaram trabalho médio inferior ao dos lineares (subótimos), o que é consistente com a solução analítica. Em direção a protocolos eficientes, um sistema de *feedback* foi implementado para converter informação em energia, inspirado na ideia do demônio de Maxwell. Apesar dos desafios experimentais, os protocolos com *feedback* retornaram valores de trabalho médio inferiores aos sem *feedback*, e a eficiência pode ser explorada alterando os critérios do demônio. Finalmente, são fornecidos resultados iniciais visando explorações da termodinâmica estocástica na interface clássico-quântico através da investigação de partículas opticamente ativas presas (formadas por *quantum dots*). A análise do recuo das partículas revelou que a dinâmica de Langevin deve ser estendida para descrever nosso sistema com precisão.

Palavras-chave: Termodinâmica estocástica. Pinças ópticas. Protocolos ótimos. Armadilhas ópticas de *feedback*. Interface clássico-quântica.

LIST OF FIGURES

Figure 1 – Basic scheme of the beam's trajectory (black lines) during reflection and refraction and resulting forces, i.e., radiation pressure and trapping force, respectively. Gravitational force, generally negligible, is also represented. The thicker and thinner arrows indicate the position-dependent intensity of the Gaussian beam. 34

Figure 2 – Simplified description of the Setup IFSC-USP. The trapping system comprises a 1064 nm infrared laser controlled by an AOM. A telescope decreases the beam waist to increase the AOM efficiency, and another enlarges it again to fill the objective entrance. A 532 nm probing laser is aligned with the trapping laser in the detection system and a condenser collects the green scattered light, directs it through a lens to reduce its size, and then sends it to the QPD. Additionally, a white LED and a CCD camera are used for visualizations of the particle. Mirrors and dichroic filters guide the beams. Inset is shown the type of cell used in the experiment in order to acquire long measurements. 36

Figure 3 – Simplified description of the Setup ENS-Lyon. The trapping system comprises a 1064 nm infrared laser connected to a set of two perpendicular AODs and a telescope enlarges the beam waist and fills the objective entrance. A 785 nm probing laser is aligned with the trapping laser in the detection system and a condenser collects the red scattered light, directs it through a lens to reduce its size, and then sends it to the QPD. A white LED and a CCD camera are used for the visualization of the particle. Mirrors and dichroic filters guide the beams. 37

Figure 4 – Normalized power of the infrared laser *versus* voltage applied on the amplitude input control of RF driver. A ramp from -1 V to $+1$ V was applied in the amplitude channel of the RF driver. Data obtained by Setup ENS-Lyon. 38

Figure 5 – Position of the trapped bead during the application of an input voltage from -1 V to $+1$ V in the frequency of the RF driver that is equivalent to a deviation from -2 MHz to $+2$ MHz. The frequency of modulation is 0.1 Hz. Since the camera calibration is 109 nm/pixel, the calibration of the modulated laser displacement is 971.2 ± 0.4 nm/MHz for 10 trajectories. A 2 μm trapped silica was used. Data obtained by Setup ENS-Lyon. 39

Figure 6 – Scheme of the QPD functioning (left) and QPD signal *versus* displacement of the trapping beam position (right). An input voltage from -1 V to $+1$ V was applied in the frequency of the RF driver, which is equivalent to a deviation from -2 MHz to $+2$ MHz. The calibration result from the fit, in green, is 3.698 ± 0.007 V/μm for 10 trajectories. A 2 μm trapped silica was used. Data obtained with Setup ENS-Lyon. 40

Figure 7 – Position histograms from time series data (left) and resulting potentials (right) corresponding to a 2 μm silica bead trapped with three different force constants ($\kappa_1 > \kappa_2 > \kappa_3$), from highest to lowest in blue, orange, and green, respectively. The fit (solid line) results in $\kappa_U = 21.54 \pm 0.03$, 12.69 ± 0.07 and 7.51 ± 0.07 pN/μm for the potential curve. Average curves of 10 acquisitions collected at 100 kHz for 30 s are presented. . . 43

Figure 8 – Autocorrelation (left) and mean squared displacement (right) corresponding to a 2 μm silica bead trapped with three different force constants ($\kappa_1 > \kappa_2 > \kappa_3$), from highest to lowest in blue, orange, and green, respectively. The fit (solid line) results in $\kappa_C = 22.6 \pm 0.1$, 13.08 ± 0.02 and 7.170 ± 0.003 pN/μm and $S_C = 3.659 \pm 0.014$, 3.510 ± 0.004 and 3.4656 ± 0.0011 V/μm for the autocorrelation and $\kappa_{MSD} = 22.379 \pm 0.003$, 13.048 ± 0.002 and 7.1711 ± 0.0014 pN/μm and $S_{MSD} = 3.888 \pm 0.002$, 3.6123 ± 0.0011 and 3.5001 ± 0.0011 V/μm for the mean squared displacement. Average curves of 10 acquisitions collected at 100 kHz for 30 s. Both graphs are rescaled considering the amplification factor obtained for each curve. 44

Figure 9 – Power spectrum density analysis corresponding to a 2 μm silica bead trapped for three different force constants ($\kappa_1 > \kappa_2 > \kappa_3$), from highest to lowest in blue, orange, and green, respectively. The fit (solid line) results in $\kappa_{PSD} = 25.195$, 12.589 and 6.710 pN/μm and $S_{PSD} = 4.029$, 3.709 and 3.560 V/μm. Average curves of 10 acquisition files collected at 100 kHz for 30 s each. The length of the Fast Fourier Transform (FFT) is $N_{FFT} = 8\ 10^5$. The graphs are rescaled considering the amplification factor obtained for each curve. 46

Figure 10 – Calibration curves for trap stiffness (right) and amplification factor (left) as a function of PD voltage, which is linearly proportional to the trapping beam intensity. For trap stiffness curves, one has the equipartition method in blue, potential analysis in orange, mean squared displacement in green, autocorrelation function in red and power spectrum density in purple. For the amplification factor, the mean squared displacement is blue, the autocorrelation function is orange, and the power spectrum density is green. The uncertainties are smaller than the dots. 47

Figure 11 – Scheme of a piston with two different volumes and analogy with a particle trapped in a harmonic potential with two different trap stiffnesses. 50

Figure 12 – Time evolution of $w(t)$ for $\Delta\lambda = 10\lambda_i$, $\lambda_i = 1.5\, pN/\mu m$, and $\tau_P = 0.1\tau_R$, where $\tau_R = \gamma/\lambda_i \approx 12$ ms is the relaxation time in the state λ_i. 52

Figure 13 – Calibration curves for trap stiffness (left) and amplification factor (right) from PSD fits as a function of PD voltage. The PD voltage is linearly proportional to the trapping beam intensity. The slope is $m_{TS} = 24.89 \pm 0.14$ (pN/μm)/V and y-intercept is $b_{TS} = 0.09 \pm 0.04$ pN/μm for the trap stiffness calibration. The slope is $m_S = 1.17 \pm 0.05$ (V/μm)/V and y-intercept is $b_S = 3.333 \pm 0.014$ V/μm for the amplification factor calibration. 53

Figure 14 – Theoretical control parameter $\lambda_{theo}(t)$ (left) for a procedure with a compressing (forward) protocol, in blue, followed by an expanding (reverse) one, in orange, and corresponding voltage applied in the amplitude of RF's driver (right). Firstly, the particle is thermalized for an equilibrium time, τ_{eq}, in green, and then the linear protocol is applied in a time duration τ_P, in red. Here, $\tau_{eq} = 20$ ms, $\lambda_i = 1.5\ pN/\mu m$, $\Delta\lambda = 10\lambda_i$, and $\tau_P = 2\tau_R$, where $\tau_R = \gamma/\lambda_i \approx 12$ ms is the relaxation time in the state λ_i. 53

Figure 15 – Estimated trap stiffness (top) and 500 trajectories (bottom) for a compressing linear protocol with $\tau_{eq} = 20$ ms, $\lambda_i = 1.5\ pN/\mu m$, $\Delta\lambda = 10\lambda_i$ and different protocol times: $\tau_P = 0.1\tau_R$ (left) and $\tau_P = 2\tau_R$ (right), where $\tau_R = \gamma/\lambda_i \approx 12$ ms is the relaxation time in the state λ_i. 55

Figure 16 – Position histograms at different instants of a compressing linear protocol: $t = -\tau_{eq}$ (beginning of the equilibrium process) in blue, $t = -\tau_{eq}/2$ (middle of the equilibrium process) in orange, $t = 0$ ms (end of the equilibrium process and beginning of the protocol) in green, and $t = \tau_P$ (end of the protocol). The positions were obtained from 10^4 positions with $\tau_{eq} = 20$ ms, $\tau_P = 0.1\tau_R$, $\lambda_i = 1.5\ pN/\mu m$, $\Delta\lambda = 10\lambda_i$, where $\tau_R = \gamma/\lambda_i \approx 12$ ms is the relaxation time in the state λ_i. 56

Figure 17 – Typical values for $\lambda_{j+1} - \lambda_j$ for linear protocols with $\tau_{eq} = 20$ ms, $\lambda_i = 1.5\ pN/\mu m$, $\Delta\lambda = 10\lambda_i$ and $\tau_P = 0.1\tau_R$, where $\tau_R = \gamma/\lambda_i \approx 12$ ms is the relaxation time in the state λ_i. 57

Figure 18 – Temporal evolution of work in blue, heat in orange, and internal energy difference in green during compressing linear protocols with $\tau_{eq} = 20$ ms, $\lambda_i = 1.5\ pN/\mu m$, $\Delta\lambda = 10\lambda_i$ and different protocol times: $\tau_P = 0.1\tau_R$ (left) and $\tau_P = 2\tau_R$ (right), where $\tau_R = \gamma/\lambda_i \approx 12$ ms is the relaxation time in the state λ_i. 57

Figure 19 – Probability distribution of work (left), heat, and internal energy difference (right) for 10^4 trajectories of compressing linear protocols with $\tau_{eq} = 20$ ms, $\lambda_i = 1.5\ pN/\mu m$, $\Delta\lambda = 10\lambda_i$, and $\tau_P = 0.1\tau_R$, where $\tau_R = \gamma/\lambda_i \approx 12$ ms is the relaxation time in the state λ_i. The black dashed line represents the free energy difference. 58

Figure 20 – Probability distribution of work (left), heat, and internal energy difference (right) for 10^4 trajectories of compressing linear protocols with $\tau_{eq} = 20$ ms, $\lambda_i = 1.5\ pN/\mu m$, $\Delta\lambda = 10\lambda_i$, and $\tau_P = 2\tau_R$, where $\tau_R = \gamma/\lambda_i \approx 12$ ms is the relaxation time in the state λ_i. The black dashed line represents the free energy difference. 58

Figure 21 – Protocol time dependency of the average values of work, in blue, heat, in orange, and internal energy difference, in green, for 10^4 trajectories of compressing linear protocols with $\tau_{eq} = 20$ ms, $\lambda_i = 1.5\ pN/\mu m$ and different modulation amplitudes $\Delta\lambda = \lambda_i$ (left) and $\Delta\lambda = 10\lambda_i$ (right), where $\tau_R = \gamma/\lambda_i \approx 12$ ms is the relaxation time in the state λ_i. The black dashed line represents the free energy difference, solid lines denote theoretical predictions, and dots correspond to experimental results. Note that here, the solid curves for work and heat are the same, and the uncertainties are smaller than the dots. 59

Figure 22 – Experimental (dots) and theoretical (solid lines) energetics dependency on modulation amplitude obtained from 10^4 trajectories of linear protocols with $\tau_{eq} = 20$ ms, $\lambda_i = 1.5\ pN/\mu m$ and $\tau_P = 0.145\tau_R$, where $\tau_R = \gamma/\lambda_i \approx 12$ ms is the relaxation time in the state λ_i. Average work in blue, heat in orange, and internal energy difference in green. The uncertainties are smaller than the dots. 60

Figure 23 – Protocol time dependency of energetics variance obtained from 10^4 trajectories of linear protocols with $\tau_{eq} = 20$ ms, $\lambda_i = 1.5\ pN/\mu m$ and different modulation amplitudes $\Delta\lambda = \lambda_i$ (left) and $\Delta\lambda = 10\lambda_i$ (right), where $\tau_R = \gamma/\lambda_i \approx 12$ ms is the relaxation time in the state λ_i. Variance of work in blue, heat in orange, and internal energy difference in green. The uncertainties are smaller than the dots. 60

Figure 24 – Protocol time dependency of $\langle W\rangle - \langle Q\rangle - \langle \Delta E\rangle$ for 10^4 trajectories of compressing linear protocols with $\tau_{eq} = 20$ ms, $\lambda_i = 1.5\ pN/\mu m$ and different modulation amplitudes $\Delta\lambda = \lambda_i$ in blue, $3\lambda_i$ in orange, and $10\lambda_i$ in green, where $\tau_R = \gamma/\lambda_i \approx 12$ ms is the relaxation time in the state λ_i. The solid red line denotes the theoretical prediction, and the dots correspond to the experimental results. 61

Figure 25 – On the left is the convergence of $\langle e^{-W/k_BT}\rangle$ *versus* number of experimental protocols run for $\Delta\lambda = \lambda_i$ and different protocol times, $\tau_P = 0.1\tau_R$, $0.45\tau_R$ and $2\tau_R$, in blue, orange, and green respectively. On the right are the final results of $\langle e^{\Delta F-W/k_BT}\rangle$ *versus* protocol time for different modulation amplitudes: $\Delta\lambda = \lambda_i$, $3\lambda_i$, and $10\lambda_i$ in red, purple, and brown, respectively. Results for compressing linear protocols with $\tau_{eq} = 20$ ms, and $\lambda_i = 1.5\ pN/\mu m$, where $\tau_R = \gamma/\lambda_i \approx 12$ ms is the relaxation time in the state λ_i. The black continuous line represents the expected value, and the dashed lines denote the uncertainties. 62

Figure 26 – Probability distribution of work (left) and results from the testing of Jarzynski's equality (right) for 10^4 trajectories of an expanding linear protocol. Here, we see the convergence of $\langle e^{-W/k_BT}\rangle$ *versus* number of protocols run for $\Delta\lambda = 10\lambda_i$, $\tau_P = 0.1\tau_R$, $\tau_{eq} = 20$ ms, and $\lambda_i = 1.5\ pN/\mu m$, where $\tau_R = \gamma/\lambda_i \approx 12$ ms is the relaxation time in the state λ_i. The black continuous line represents the expected value of $\langle e^{-\Delta F/k_BT}\rangle$ and the dashed lines denote the uncertainties. 63

Figure 27 – Probability distributions of work $P_F(W)$ in blue, $P_R(W)$ in orange, and $P_R(-W)$ in green for different modulation amplitudes: $\Delta\lambda = \lambda_i$ (top) and $\Delta\lambda = 10\lambda_i$ (bottom). Results from 10^4 trajectories with $\tau_{eq} = 20$ ms, $\lambda_i = 1.5\ pN/\mu m$, and $\tau_P = 0.1\tau_R$, where $\tau_R = \gamma/\lambda_i \approx 12$ ms is the relaxation time in the state λ_i. The free energy difference is represented by the black dashed line. 65

Figure 28 – Verification of Crooks theorem for different modulation amplitudes: $\Delta\lambda = \lambda_i$ (left) and $\Delta\lambda = 10\lambda_i$ (right). The results were calculated by Eq. 4.20 from 10^4 trajectories with $\tau_{eq} = 20$ ms, $\lambda_i = 1.5\ pN/\mu m$, and different protocol times: $\tau_P = 0.1\tau_R$ in blue, $0.45\tau_R$ in orange, and $2\tau_R$ in green, where $\tau_R = \gamma/\lambda_i \approx 12$ ms is the relaxation time in the state λ_i. 66

Figure 29 – Optimal protocols for the moving laser trap case obtained for $\lambda_f = 500$ nm and different protocol times. The black dashed line represents the linear protocol. Trap stiffness $\kappa = 1$ pN/μm was used for all curves. 69

Figure 30 – Optimal protocols for the time-dependent trap stiffness case obtained for different parameters. Here, $\Delta\lambda = (\lambda_f - \lambda_i)$ with $\lambda_i = 1.5$ pN/μm. The black dashed line represents the linear protocol. 70

Figure 31 – Simulated probability distribution of work from 10^5 trajectories. Results for linear protocols, in blue, and optimal ones, in orange, where $T = 300$ K, $\Delta t = 10^{-5}$ s, $\lambda_f = 100$ nm, $\kappa = 1$ pN/μm, $\tau_P = 0.5\tau_R$, and $\gamma = 6\pi\eta R$, being $\eta = 0.001$ Nsm^{-2} and $R = 1\ \mu$m. 72

Figure 32 – Comparison of the simulated average work for linear protocols, in blue, and optimal ones, in orange. The results refer to fixed $\tau_P = 0.5\tau_R$ and different values of λ_f (left) and fixed $\lambda_f = 100$ nm and different protocol times τ_P (right). Here, 10^5 trajectories were simulated with the following parameters: $T = 300$ K, $\Delta t = 10^{-5}$ s, $\kappa = 1$ pN/μm, and $\gamma = 6\pi\eta R$, being $\eta = 0.001$ Nsm^{-2} and $R = 1$ μm. 73

Figure 33 – Jarzynski test. Comparison of simulated $\langle e^{-W/k_BT}\rangle$ for linear protocols, in blue, and optimal ones, in orange. Results refer to fixed $\tau_P = 0.5\tau_R$ and different values of λ_f (left) and fixed $\lambda_f = 100$ nm and different protocol times τ_P (right). Here, 10^5 trajectories were simulated with the following parameters: $T = 300$ K, $\Delta t = 10^{-5}$ s, $\kappa = 1$ pN/μm, and $\gamma = 6\pi\eta R$, being $\eta = 0.001$ Nsm^{-2} and $R = 1$ μm. The black dashed line represents $e^{-\Delta F/k_BT} = 1$. 74

Figure 34 – Estimated trap stiffness (left), λ_j, and its derivative (right), $\lambda_{j+1} - \lambda_j$, (data from PD and input signal) for linear protocols with $\tau_{eq} = 20$ ms, $\lambda_i = 1.5$ $pN/\mu m$, $\Delta\lambda = 10\lambda_i$ and $\tau_P = 0.1\tau_R$ for a single loop, where $\tau_R = \gamma/\lambda_i \approx 12$ ms is the relaxation time in the state λ_i. 75

Figure 35 – Temporal evolution of work for 10 trajectories of optimal protocols with $\tau_{eq} = 20$ ms, $\lambda_i = 1.5$ $pN/\mu m$, $\Delta\lambda = 10\lambda_i$ and different protocol times: $\tau_P = 0.1\tau_R$ (left) and $\tau_P = 2\tau_R$ (right), where $\tau_R = \gamma/\lambda_i \approx 12$ ms is the relaxation time in the state λ_i. 75

Figure 36 – Work probability distributions (solid lines) and their corresponding average values (dashed lines) for different modulation amplitudes $\Delta\lambda = \lambda_i$ (top), and $\Delta\lambda = 10\lambda_i$ (bottom). Results from 10^4 trajectories for linear protocols, in blue, and optimal ones, in orange. Here, $\tau_{eq} = 20$ ms, $\lambda_i = 1.5$ $pN/\mu m$, $\tau_P = 0.1\tau_R$, where $\tau_R = \gamma/\lambda_i \approx 12$ ms is the relaxation time in the state λ_i. 76

Figure 37 – Experimental measurements of the average (stochastic) work for an ensemble of 10^4 trajectories in function of protocol time. Experimental results are represented by dots and theoretical predictions are denoted by solid lines. Values obtained from linear protocols, in blue, and optimal ones, in orange, with $\tau_{eq} = 20$ ms, $\lambda_i = 1.5$ $pN/\mu m$ and different modulation amplitudes $\Delta\lambda = \lambda_i$ (left), and $\Delta\lambda = 10\lambda_i$ (right), where $\tau_R = \gamma/\lambda_i \approx 12$ ms is the relaxation time in the state λ_i. The uncertainties are smaller than the dots. 77

Figure 38 – Experimental measurements of the average (stochastic) work for an ensemble of 10^4 trajectories in function of the modulation amplitude. Experimental results are represented by dots and theoretical predictions are denoted by solid lines. Values obtained from linear protocols, in blue, and optimal ones, in orange, with $\tau_{eq} = 20$ ms, $\lambda_i = 1.5\ pN/\mu m$ and $\tau_P = 0.145\tau_R$, where $\tau_R = \gamma/\lambda_i \approx 12$ ms is the relaxation time in the state λ_i. The black dashed line represents the free energy difference. The uncertainties are smaller than the dots. 78

Figure 39 – Protocol time dependency of work variance for $\Delta\lambda = 10\lambda_i$ (left) and amplitude modulation dependency of work variance for $\tau_P = 0.145\tau_R$ (right). Values obtained from linear protocols, in blue, and optimal ones, in orange, from 10^4 trajectories with $\tau_{eq} = 20$ ms, $\lambda_i = 1.5\ pN/\mu m$, where $\tau_R = \gamma/\lambda_i \approx 12$ ms is the relaxation time in the state λ_i. The uncertainties are smaller than the dots. 79

Figure 40 – Jarzynski verification for experiments with optimal protocols. Final results of $\langle e^{\Delta F - W/k_BT} \rangle$ for different protocol times and modulation amplitudes: $\Delta\lambda = \lambda_i$, $3\lambda_i$, and $10\lambda_i$ in red, purple, and brown, respectively. The black continuous line represents the expected value. Results for $\tau_{eq} = 20$ ms, and $\lambda_i = 1.5\ pN/\mu m$, where $\tau_R = \gamma/\lambda_i \approx 12$ ms is the relaxation time in the state λ_i. 79

Figure 41 – Scheme of the feedback implementation. It starts with the preparation of the particle in state λ_i for an equilibrium time τ_{eq} and the bead's position is then acquired for switching the state to λ_f when $|x| < x_S$. . 83

Figure 42 – Scheme of the switch in the particle's state when $|x| < x_S$. The initial state, λ_i, is represented by the solid line and the final state, λ_f, is denoted by the black dashed line. 83

Figure 43 – Histogram of the time interval between acquisitions, Δt, for 1000 protocols. The histogram has 100 bins. 85

Figure 44 – Trajectories for 100 protocols with different threshold values $x_S = 107$, 53, 21 nm (from top to bottom). The black dashed line corresponds to the laser's detection moment of the switch. 86

Figure 45 – Probability distributions of work and their average values (vertical solid lines) for the step protocol without feedback (A) and with feedback - W_- (B) and W_+ (C). The protocols with feedback were applied for different threshold values: $x_S = 107$, 64 and 21 nm in blue, orange and green, respectively. The Black dashed line represents the free energy difference. The original histograms have 1000 bins obtained from $3 \cdot 10^4$ trajectories. Here $\lambda_i = 1$ pN/μm, $\lambda_f = 2\lambda_i$ and $\tau_{eq} = 40$ ms. 87

Figure 46 – Average work for W_-, in blue, and W_+, in orange, for different threshold values. Each point corresponds to the average of $3 \cdot 10^4$ trajectories. Here, $\lambda_i = 1$ pN/μm, $\lambda_f = 2\lambda_i$ and $\tau_{eq} = 40$ ms. The black dashed line represents the free energy difference. The uncertainties are smaller than the dots. 89

Figure 47 – Convergence of Jarzynski equality for different thresholds $x_S = 107$, 64 and 21 nm in blue, orange, and green, respectively (left). Points represent values obtained from $\langle \exp\left(\frac{\Delta F - W_-}{k_B T}\right)\rangle$ and crosses from $\langle \exp\left(\frac{\Delta F - W_+}{k_B T}\right)\rangle$. Dependency of α in the threshold x_S (right) obtained from $3 \cdot 10^4$ trajectories for $\langle \exp\left(\frac{\Delta F - W_-}{k_B T}\right)\rangle$ in blue and $\langle \exp\left(\frac{\Delta F - W_+}{k_B T}\right)\rangle$ in orange. . . . 89

Figure 48 – TEM image for super-crystals of many SQWs of different sizes and scheme of a single SQW structure (inset). Here, the CdS is in blue, and the CdSe is in orange, and typically $r = 1.3$ nm, $l = 1.7$ nm and $R = 3.4$ nm. 92

Figure 49 – Absorption and emission spectra of super-crystals formed by SQWs (CdS/CdSe/CdS). 93

Figure 50 – Diagram of the pulsed laser temporal profile showing the periods when the laser is on and off. Here, T is the repetition time and τ is the pulse duration. 94

Figure 51 – Simplified description of the experimental setup described in Sec. 3.1.2, with the addition of the 640nm pulsed laser. A high focal length lens increases the beam's diameter in the trapping position and a set of ODs and one polarizer control the pulsed laser power. The inset shows the scheme of the beams' alignment after the objective with the trapping laser in orange, the probe laser in dark red, and the excitation laser in fuchsia. 97

Figure 52 – Image of the microscopic super-crystal formed by SQWs and its contour. The resulting radius is approximately 2.4 μm. 98

Figure 53 – Position histogram (left) and PSD (right) for x and y directions. The trap stiffnesses are $\kappa_x = 1.5$ pN/μm and $\kappa_y = 1.6$ pN/μm. Results from measurements of the time series position of a trapped particle with 2.4 μm radius for $t = 100$ s with a $f = 100$ kHz acquisition rate. . 99

Figure 54 – PSD in y direction. First, the region $f_e - 100$ Hz $< f < f_e + 100$ Hz is zoomed to obtain the peaks and the thermal noise (left). The peaks region is then zoomed in the frequency range used in the integration, I (Eq. 7.12), around the frequency of excitation in blue, $f_e = 16.1$ kHz, and frequency of modulation in orange, $f_m = 16.09$ kHz. The black dashed line represents the thermal noise, $\langle F_{th}^2 \rangle$. Here, the pulsed laser operates at a 16.1 kHz frequency (excitation) and the trapping laser position is controlled at a 16.09 kHz frequency (modulation). Data were collected at 100 kHz for 100 s and $N_{FFT} = 10^7$. 100

Figure 55 – Frequency control. Average power dependency of optical force (left) and modulation force (right) from $f_e = 16.1$ kHz to 45.1 kHz and $f_m = f_e - 10$ Hz. Experimental values (dots) and linear fit on *loglog* scale (solid lines) in blue and theoretical predictions in orange. 101

Figure 56 – Width control. Average power dependency of optical force (left) and modulation force (right) from $\tau = 5$ ns to 39 ns. Experimental values (dots) and linear fit on *loglog* scale (solid lines) in blue and theoretical predictions in orange. 101

Figure 57 – Polarizer control. Average power dependency of optical force (left) and modulation force (right) for different polarizer's angular positions. Experimental values (dots) and linear fit on *loglog* scale (solid lines) in blue and theoretical predictions in orange. 102

Figure 58 – Typical PD voltage signal (original one in blue and filtered one in orange) as a function of the sample number for linear (left) and optimal (right) protocols with $\tau_{eq} = 20$ ms, $\lambda_i = 1.5\ pN/\mu m$, $\Delta\lambda = 10\lambda_i$ and $\tau_P = 0.1\tau_R$, where $\tau_R = \gamma/\lambda_i \approx 12$ ms is the relaxation time in the state λ_i. 121

Figure 59 – Typical differential of the PD voltage signal for linear (left) and optimal (right) protocols as a function of sample number, with $\tau_{eq} = 20$ ms, $\lambda_i = 1.5\ pN/\mu m$, $\Delta\lambda = 10\lambda_i$ and $\tau_P = 0.1\tau_R$, where $\tau_R = \gamma/\lambda_i \approx 12$ ms is the relaxation time in the state λ_i. The peaks corresponding to the identification of the forward process are crossed in orange, and the reverse processes are crossed in green. 122

Figure 60 – Typical PSD (left) and position histogram with 1000 bins (right) for original data in blue and filtered data in orange. Measuring time is $t = 30$ s and data were acquired at a $f = 100$ kHz acquisition rate for a 2 μm silica trapped particle. 123

Figure 61 – Calibration curves for trap stiffness (right) and amplification factor (left) from PSD fits. The angular coefficient is $m_{TS} = 2.60 \pm 0.03$ (pN/μm)/V and y-intercept is $b_{TS} = 0.01 \pm 0.04$ pN/μm for the trap stiffness calibration. The average of 10 files was calculated from PSD curves, and the interval 0 Hz $< f <$ 2 kHz was used for the fit. 124

LIST OF ABBREVIATIONS AND ACRONYMS

AC	Autocorrelation function
AOM	Acousto-optic modulator
AOD	Acousto-optic deflector
FFT	Fast Fourier Transform
FPGA	Field Programmable Gate Array
MSD	Mean squared displacement
OD	Optical density
PD	Photodetector
PSD	Power Spectrum density
QPD	Quadrant photodiode
RF	Radiofrequency
SQW	Spherical Quantum Well
TEM	Transmission Electron Microscopy

CONTENTS

1 INTRODUCTION . . . 23

2 CONTEXTUALIZATION . . . 25

2.1 Thermodynamics . . . 25

2.2 Stochastic Thermodynamics . . . 27

2.3 Thermodynamics of a trapped Brownian particle . . . 29

2.3.1 The Langevin equation . . . 29

2.3.2 Fokker-Planck equation . . . 31

2.3.3 Energetics of stochastic trajectories . . . 31

3 OPTICAL TWEEZERS . . . 33

3.1 Experimental apparatuses . . . 34

3.1.1 Setup IFSC-USP . . . 34

3.1.2 Setup ENS-Lyon . . . 35

3.1.3 Modulation system . . . 37

3.1.4 Tracking system . . . 39

3.2 Calibration techniques . . . 41

3.2.1 Equipartition theorem of energy . . . 41

3.2.2 Position histrogram analysis . . . 42

3.2.3 Autocorrelation function and mean squared displacement analysis . . . 43

3.2.4 Power spectrum density analysis . . . 45

3.2.5 Comparison between calibration techniques . . . 46

4 ENERGETICS OF THERMODYNAMIC PROCESSES . . . 49

4.1 Isothermal compression in optical tweezers . . . 49

4.1.1 Linear protocol description . . . 50

4.2 Protocol application . . . 52

4.3 Experimental results . . . 54

4.3.1 Verification of the First Law of Thermodynamics . . . 57

4.3.2 Verification of Jarzynski equality . . . 60

4.3.3 Verification of Crooks relation . . . 63

4.4 Conclusions . . . 64

5 OPTIMAL PROCESSES . . . 67

5.1 Prediction for finite-time protocols . . . 67

5.1.1 Moving laser trap . . . 68

5.1.2 Time-dependent trap stiffness . . . 69

5.2 Simulations for the moving potential 71
5.3 Experimental results for the compressing protocol 74
5.4 Conclusions 77

6 INFORMATION-TO-ENERGY CONVERSION 81
6.1 Maxwell's demon 81
6.2 Proposed feedback protocol 82
6.3 Work calculation and time delay 84
6.4 Protocol application and experimental results 85
6.5 Conclusions 89

7 STUDY OF OPTICALLY ACTIVE SUPER-CRYSTALS IN A TRAP 91
7.1 CdS/CdSe/CdS quantum dots colloids 92
7.2 Mechanical dynamics in the trap 93
7.3 Experimental system and sample preparation 96
7.4 Characterization of the optical trap 97
7.5 Experimental Results 98
7.6 Conclusions 102

8 THESIS EVOLUTION AND CONCLUSIONS 105

REFERENCES 111

APPENDIX 119

APPENDIX A – PROTOCOL'S STARTING POINT 121

APPENDIX B – CHARACTERIZATION OF THE SYSTEM'S NOISE123

APPENDIX C – MECHANICAL DISPLACEMENT IN THE TRAP 125

1 INTRODUCTION

Thermodynamics is the scientific discipline that studies work, heat, and temperature, establishing fundamental laws that rule all processes involving the exchange of different forms of energy (1–3). Its extensive study has made contributions that range from the development of macroscopic thermal machines, assisting the advent of the Industrial Revolution, to the understanding of natural and artificial microscopic systems, hence, the emergence of innovative technologies.

Nevertheless, many conceptual questions regarding smaller scales remain open. In this regime, fluctuations of thermodynamic quantities become non-negligible and should be taken into account, thus requiring the implementation of a statistical approach (4). In this scenario, the so-called stochastic thermodynamics has emerged as the framework that studies the thermodynamic behavior of microscopic systems towards answering several of those issues (5–7).

Colloidal physics combined with optical tweezer technology enables the demonstration of numerous stochastic thermodynamics and statistical physics results (8–9). Benefiting from its versatility, we have built an optical tweezer system to perform out-of-equilibrium tasks on the mesoscopic scale in the classical regime and expand our investigations to the classical-quantum interface for assessing the validity of classical stochastic thermodynamics in this limit.

This thesis is structured as follows:

- Chapter 2 discusses general aspects of thermodynamics and stochastic thermodynamics, providing a big picture in which this thesis is inserted. Specifically, the focus is on the thermodynamic description of the system under study, namely, a Brownian particle trapped in a harmonic potential. Understanding the dynamics of such a system and how to extract thermodynamic quantities from its trajectories are crucial for our subsequent analyses.

- Chapter 3 delves into our experimental apparatuses, detailing how to control the parameters of the trap and acquire data. Essential calibrations for the characterization of the optical potential and tracking acquisition device are discussed, laying the groundwork for our investigations into stochastic thermodynamics.

- Chapter 4 introduces compression and expansion finite-time protocols and their experimental implementation. The protocols are studied to validate our experimental setup's robustness by testing thermodynamic laws and fluctuation theorems, such as Jarzynski's equality and Crooks's theorem.

- Chapter 5 describes experiments exploring optimal control. First, it presents analytical solutions for minimizing mean work injected into the system for moving traps and compressing protocols. Afterwards, numerical simulations of the first case and experimental findings of the second one are discussed, comparing optimal curves with linear (suboptimal) ones and verifying their consistency with Jarzynski equality.

- Chapter 6 focuses on the implementation of feedback control. Inspired by Maxwell's demon idea, the way information translates into generalized Jarzynski equality is discussed and experimental results from protocols with and without feedback are presented.

- Chapter 7 explores the classical-quantum interface by trapping optically active particles formed by quantum dots. It also outlines necessary experimental modifications and theoretical expectations regarding optical effects present in the system. Then, it is discussed the initial experimental findings related to the coupling between particle recoil and expected quantum effects.

- Finally, Chapter 8 reflects on the challenges encountered and the significant results achieved throughout this thesis while also proposing avenues for future research.

2 CONTEXTUALIZATION

This chapter discusses general aspects of thermodynamics and stochastic thermodynamics that are important for contextualizing the present research and provides the thermodynamic description of the target system, i.e., a Brownian particle trapped in a harmonic potential.

This chapter offers a comprehensive overview of the key principles of thermodynamics and stochastic thermodynamics, which are crucial for understanding the context of the present research. It delves into the thermodynamic behavior of the specific system under study, namely a Brownian particle confined within a harmonic potential, and provides a detailed theoretical framework for analyzing its dynamics.

2.1 Thermodynamics

Thermodynamics emerged in the 17th century as a phenomenological and empirical field of study for describing and improving mechanical heat engines. Over the years, the area has gained ground and evolved into one of the most successful and robust physical theories in history (10).

Chronologically, the definitions start with the traditional macroscopic thermodynamics (2, 11), which describes large systems whose internal structure can be neglected. Here, the description is based on measurable macroscopic variables such as pressure (P), volume (V), and temperature (T) and the system's states are always in equilibrium or near equilibrium, i.e., with fixed and well-defined thermodynamic quantities.

Once the state of equilibrium has been defined, the system can be taken from one coordinate in the phase space to another in a near-equilibrium thermodynamic process. Despite the change in the state perturbing the configuration, if the process is quasi-statically performed, the system can be considered weakly disturbed by the infinitesimal changes and remains in equilibrium. Such transformations and possible interactions of the thermodynamic system with other objects and their surroundings are described and constrained by the so-called Laws of Thermodynamics.

Since systems at different temperatures eventually reach thermal equilibrium, the zeroth law states if two systems are individually in thermal equilibrium with a third, they are all in thermal equilibrium. This first introductory statement also brings up the idea of energy exchange between systems, and the First Law of Thermodynamics ensures the conservation of that quantity.

For a more comprehensive understanding of the First Law, let us define the internal energy E of the system, which is the energy contained in it and depends on its macroscopic variables. When the system changes from a state A to a state B, the variation of the state function $\Delta E = E_B - E_A$ depends only on initial and final conditions. Therefore, for a cyclic process, ΔE is zero and if the system is isolated, i.e., it does not interact with other objects, the internal energy is kept constant.

The energy exchanges can be distinguished into two types, namely heat (Q) and work (W). The first one results from the system's internal configuration change when two bodies with different temperatures are in thermal contact and the second originates from a disturbance applied when the thermodynamic coordinates are changed. In other words, the complete relation for infinitesimal changes in energy dE is given by

$$dE = \delta Q + \delta W, \tag{2.1}$$

where δ represents inexact differentials, since those variables are not state functions, i.e., they depend on the system's trajectory. Therefore, a change in the system's state through two possible paths will result in different values for work and heat; however, the variation in the internal energy will be the same. Such a relationship between infinitesimal work (δW) and heat (δQ) is the basis of the First Law of Thermodynamics.

Despite the possibility of transforming those two quantities into each other, the Second Law of Thermodynamics states a conversion limit, basically restricting the amount of heat that can be effectively converted into work and establishing the concepts of entropy and irreversibility.

Clausius theorem (12) for cyclic and reversible (quasi-static) processes states,

$$\oint \frac{\delta Q}{T} = 0, \tag{2.2}$$

where T is the bath temperature. For Eq. 2.2 to be valid, the value $\delta Q/T$ must be a state function, where its integral does not depend on the path. Therefore, the quantity

$$dS \equiv \frac{\delta Q}{T} \tag{2.3}$$

is defined here as entropy. For a change from state A to state B, the variation in entropy is given by (2)

$$\Delta S = S_B - S_A = \int_A^B \frac{\delta Q}{T}. \tag{2.4}$$

The sum of the entropy of the system ΔS_{system} and its surroundings $\Delta S_{reservoir}$ for a given process is identified as the entropy of the universe, such that $\Delta S_{universe} = \sum \Delta S = \Delta S_{system} + \Delta S_{reservoir} = 0$.

However, the consideration of irreversible processes leads to the following general inequalities

$$\Delta S_{system} \geq \int_A^B \frac{\delta Q}{T} \text{ and } \Delta S_{universe} \geq 0, \tag{2.5}$$

i.e., the universe's entropy never decreases – it either increases or remains fixed. This quantity is closely related to the concept of the arrow of time, since all macroscopic processes occurring in nature show a positive entropy production.

Given the Helmholtz free energy defined as $F = U - TS$ for isothermal processes, the second law can be expressed as

$$\delta W \geq dF. \tag{2.6}$$

That inequality states the minimum work performed - or maximum work received - is lower bounded by the difference between the free energies of final and initial equilibrium states.

Finally, the Third Law of Thermodynamics mathematically relates the entropy value with temperature – as temperature decreases, reaching absolute zero, entropy converges to a constant value even for different macroscopic quantities.

2.2 Stochastic Thermodynamics

Although macroscopic thermodynamics provides a robust description of nature, investigating the microscopic scale's behavior in physical systems has been a natural path. The development of statistical mechanics has provided a stronger basis for the thermodynamic theory, and the proposal of the linear response regime has enabled the modelling of processes slightly out of thermodynamic equilibrium. In this scenario, stochastic thermodynamics has emerged and progressed to studies of more general microscopic systems and finite-time protocols.

On a mesoscopic scale, the energy exchanges are of the order of $k_B T$, where k_B is the Boltzmann constant and T is the system's absolute temperature. In this regime, the thermodynamic quantities exhibit an inherent stochasticity that plays an important role in the resulting dynamics.

Towards clarifying the source of those fluctuations, let us consider a box containing an ideal monoatomic gas consisting of N particles in thermal contact with a bath of temperature T. According to the equipartition theorem, the average energy of the gas is given by $\langle U \rangle = 3Nk_BT/2^*$. Moreover, the ratio between its average energy and variance σ_U^2 is inversely proportional to the number of particles, i.e., $\langle U \rangle / \sigma_U^2 \propto 1/N$. Since N typically reaches magnitudes of 10^{23} in macroscopic systems, whereas the average energy is significantly large, the ratio tends towards zero. However, if N decreases considerably, the energy distribution starts to widen for a set of systems, and such fluctuations must be considered in thermodynamic analyses.

---

* In this thesis, $\langle . \rangle$ stands for the ensemble average.

Therefore, for every single trajectory in the phase space for an ensemble of identical systems (or a unique system performing a set of equal processes), the resulting work, heat, and entropy values must be treated as stochastic variables. Fluctuation Theorems have emerged in such a scenario, proposing mathematical relations between the probability distributions of those quantities.

As an example, let us consider a system in thermal equilibrium at temperature T. Applying a classical control parameter λ that takes the particle from the prepared state equivalent to λ_i to the final one λ_f, work is given by (13)

$$W = \int_{\lambda_i}^{\lambda_f} \frac{\partial H(\lambda, x)}{\partial \lambda} d\lambda, \tag{2.7}$$

considering $H(\lambda)$ the system's parameterized Hamiltonian. The heat and internal energy difference can also be defined as

$$Q = \int_{x_i}^{x_f} \frac{\partial H(\lambda, x)}{\partial x} dx, \tag{2.8}$$

$$\Delta E = H(\lambda_f, x_f) - H(\lambda_i, x_i). \tag{2.9}$$

From the work values for an ensemble of trajectories, the so-called Jarzynski equality (14), which is an important Fluctuation Theorem, states

$$e^{-\Delta F/k_B T} = \langle e^{-W/k_B T} \rangle, \tag{2.10}$$

where ΔF is the Helmholtz free energy difference between initial (λ_i) and final (λ_f) equilibrium states. This equilibrium quantity is given by

$$\Delta F = F_f - F_i = -k_B T(\log Z_f - \log Z_i), \tag{2.11}$$

with Z_i and Z_f equal to initial and final partition functions.

Interestingly, the theorem relates a thermodynamic quantity that depends on the particle's trajectory in the phase space on the right side to a state function that depends only on initial and final states on the left side. Such equality enables estimating the free energy difference, an equilibrium property, from nonequilibrium measurements.

Using Jensen's inequality (15), $\langle e^x \rangle \geq e^{\langle x \rangle}$, one has

$$\langle W \rangle \geq \Delta F, \tag{2.12}$$

which is a generalization of Clausius inequality that considers work a stochastic variable. Although the average value for work always obeys the Second Law of Thermodynamics, individual trajectories can provide work values smaller than the free energy difference. It is important to mention that when the system's size increases, the work distributions approximate a delta function, thus returning to the classical macroscopic behavior.

Crooks proposed a relationship between forward and reverse protocols through their work probability distributions. Considering probability P_F for a protocol $\lambda_i \to \lambda_f$ and P_R for $\lambda_f \to \lambda_i$, this second Fluctuation Theorem is given by (16):

$$\frac{P_F(W)}{P_R(-W)} = e^{(W-\Delta F)/k_BT}. \tag{2.13}$$

According to the theorem, the probability of observing work W in the forward process is more likely than observing $-W$ in the reverse one. However, if the process is performed quasi-statically, work equals the free energy difference, and the probabilities are the same.

It is also natural that Jarzynski equality derives from Eq. 2.13:

$$\int dW P_R(-W) e^{-W/k_BT} = e^{-\Delta F/k_BT} \int dW P_F(W) \Rightarrow e^{-\Delta F/k_BT} = \langle e^{-W/k_BT} \rangle. \tag{2.14}$$

Such a wide range of theoretical results and the constant technological advances, which have encouraged studies of increasingly smaller systems, have led to the experimental realization of several of the aforementioned proposals and a growing interest in the area of stochastic thermodynamics (6,13,17–19). Using several types of platforms, the first experimental realizations were made in classical and quantum systems of Maxwell's Demon (20–21), Szilard's engine (22–23), Landauer's Principle verification (24–26), and tests of Fluctuation Theorems such as Jarzynski (27–30) and Crooks (31). On the other hand, many questions are still open, especially regarding a regime of structures with greater complexity, such as those of several biological systems (32–37), or when quantum properties become relevant and should be considered in the field coined quantum thermodynamics (38–40).

2.3 Thermodynamics of a trapped Brownian particle

After this brief contextualization of the big scenario in which this research is immersed, this section addresses the thermodynamics of the specific system of interest, consisting of a Brownian particle confined in an approximately harmonic potential.

2.3.1 The Langevin equation

A particle with mass m_P immersed in a liquid at absolute temperature T undergoes continuous random motion due to collisions with the fluid molecules, a phenomenon known as Brownian motion (41). The one-dimensional dynamics of a particle in thermal equilibrium with the fluid obeys the Langevin equation (42):

$$m_P \ddot{x} = -\gamma \dot{x} + F_{th}, \tag{2.15}$$

where F_{th} is a Gaussian white noise present in the system due to its contact with the thermal reservoir and $\gamma = 6\pi\eta R$ is the particle friction coefficient, where η is the medium viscosity and R is the particle radius. The thermal random noise has the following properties: $\langle F_{th}(t)\rangle = 0$ and $\langle F_{th}(t)F_{th}(t')\rangle = 2\gamma k_B T\delta(t-t')$, where δ is the Dirac delta function.

For a particle trapped in a harmonic potential, $U(x) = \kappa x^2/2$, with a force constant, κ, Eq. 2.15 becomes:

$$m_P\ddot{x} = -\gamma\dot{x} - \kappa x + F_{th}. \tag{2.16}$$

Considering measurement interval times longer than the characteristic time $\tau_C = m_P/\gamma$, the inertial term can be dropped, thus resulting in the overdamped Langevin Equation:

$$\gamma\dot{x} = -\frac{dU}{dx} + F_{th} = -\kappa x + F_{th}. \tag{2.17}$$

Although Eq. 2.17 is enough to describe small particles typically trapped in optical tweezers, the modified Langevin Equation is considered in this thesis (43):

$$m_p\ddot{x}(t) = -\kappa x(t) - \int_{-\infty}^{\infty} dt'\gamma(t-t')\dot{x}(t') + F_{\text{th}}(t), \tag{2.18}$$

where $-\int_{-\infty}^{\infty} dt'\gamma(t-t')\dot{x}(t')$ is the retarded friction force that can take into account hydrodynamic interaction. This description is required so that the dynamics of bigger particles like the ones presented in Chapter 7 can be described.

Besides the particle dynamics in the time domain, the particle position must be computed in the frequency domain, $\tilde{x}(\omega)$. Therefore, a Fourier transform of Langevin Equation is performed (Eq. 2.18)† (43):

$$\begin{aligned} -\omega^2 m_p\tilde{x}(\omega) &= -\kappa\tilde{x}(\omega) - i\omega\tilde{\gamma}(\omega)\tilde{x}(\omega) + \tilde{F}_{\text{th}}(\omega) \\ \tilde{x}(\omega) &= \tilde{\chi}(\omega)\tilde{F}_{\text{th}}(\omega) \end{aligned} \tag{2.19}$$

with susceptibility given by

$$\tilde{\chi}(\omega) = \frac{1}{\kappa - \omega^2 m_p + i\omega\tilde{\gamma}(\omega)}. \tag{2.20}$$

A modification of Stoke's force is used so that hydrodynamic effects are considered and the correction in the frequency-dependent friction coefficient is given by (43):

$$\tilde{\gamma}(\omega) = 6\pi\eta R(1 + \sqrt{i\omega\tau_f}) + i\omega m_f/2. \tag{2.21}$$

The vortex diffusion time, $\tau_f = R^2\rho_f/\eta$, considers a sphere of radius R that dislocates a fluid with density ρ_f. The last term can be interpreted as effectively increasing the particle's mass by half the displaced fluid's mass, $m_f = 4\pi R^3\rho_f/3$.

---

† Here, notation $\tilde{p}(\omega) = \int dt e^{i\omega t}p(t)$ is used.

2.3.2 Fokker-Planck equation

Another way to describe the system dynamics is by considering the probability density function $P(x,t)$, which quantifies the probability of observing a particle in a position x at an instant t. For conditions equivalent to Eq. 2.17, the Fokker-Plank equation is given by

$$\frac{\partial P(x,t)}{\partial t} = \frac{1}{\gamma}\frac{\partial}{\partial x}\left[\frac{dU(x)}{dx}P(x,t) + k_B T\frac{\partial P(x,t)}{\partial x}\right]. \tag{2.22}$$

A complete description of Eq. 2.22 can be found in (42).

2.3.3 Energetics of stochastic trajectories

From Eq. 2.17, the trajectory for a small dx is given by

$$-\left(-\gamma\dot{x} + F_{th}(t)\right)dx = \frac{\partial U(x)}{\partial x}dx. \tag{2.23}$$

According to Sekimoto (44), Eq. 2.23 can be related to heat $dQ = -\left(-\gamma\dot{x} + F_{th}(t)\right)dx$, resulting from the force exerted by the bath, and the internal energy difference of the system $(\partial U(x)/\partial x)dx$.

If the bead is exposed to a time-dependent potential due to the application of an external control parameter $\lambda(t)$, as discussed previously, then

$$dQ = \frac{\partial U(x)}{\partial x}dx. \tag{2.24}$$

Since $dU = (\partial U/\partial x)dx + (\partial U/\partial\lambda)d\lambda$, Eq. 2.24 becomes

$$dQ + dU = \frac{\partial U}{\partial\lambda}d\lambda. \tag{2.25}$$

Therefore, by changing control parameter $\lambda(t)$, the resulting stochastic work received by the system along a trajectory $x(t)$ is

$$W = \int_0^t dt'\dot{\lambda}\frac{\partial U(x,\lambda)}{\partial\lambda}. \tag{2.26}$$

and the stochastic heat dissipated by the system is

$$Q = \int_0^t dt'\left[-(-\gamma\dot{x} + F_{th}(t))\dot{x}\right]. \tag{2.27}$$

Alternatively, the heat can also be calculated by Eq. 2.8.

The present description enables the computation of the complete energetics of a trapped Brownian particle exposed to a dynamic control parameter, which, for harmonic potentials, can be the equilibrium position or the stiffness of the trap, for example. For that, only the precise potential felt by the particle and its trajectories are necessary.

3 OPTICAL TWEEZERS

As the name suggests, optical tweezers consist of an optical device that uses a light source, typically a highly focused laser, capable of trapping and manipulating particles on a micro or nanometric scale. Due to its numerous applications in biology (45–48), chemistry (49–50), nanotechnology (51), and physics (52–55), its creator, Arthur Ashkin, was laureated with the 2018 Nobel Prize nearly 50 years after having developed the first prototypes (56–58).

Although the basic experimental setup can be simple, i.e., based on a laser source coupled to a high numeral aperture lens, the theory behind the process can be very complex depending on the target particle. Whereas the most general theory explains the trapping force through a Mie scattering process (59), more humble approaches focus on two size regimes, namely, geometric optics for particles bigger than the light wavelength (8, 56), and Rayleigh limit for smaller ones (60).

A complete description of the phenomenon can be found in (8); however, for larger particles, it can be briefly explained with geometric optics considerations. Therefore, let us consider a ray of light scattering in a particle with a refractive index, n_p, different from the medium around it, n_m. If the particle does not have absorption effects, the ray will only reflect and refract (several times) on the particle surface, changing its trajectory in space. Since the photons carry momentum, a force must act on the particle to ensure the total conservation of the quantity, as schematically shown in Fig. 1.

For a set of light rays, reflection causes a push in the bead in the direction of the beam's propagation, known as radiation pressure, which is the base of the functioning of the first traps with counterpropagating beams proposed by Ashkin in (57) and still in use (61–62). However, refraction generates an attracting or repealing force to the region with a bigger gradient of intensity, called gradient force. Regarding a focalized Gaussian beam, the target region is the focus position and if $n_p > n_m$, the force is attractive. For small particle displacements, typical in the Brownian regime, one has an approximately harmonical potential, like a mass-spring system, whose trap stiffness is related to particle confinement. Besides the optical forces, since the bead has a mass, it will be affected by gravity and the balance of the three forces will result in a 3D trapping of the bead around an equilibrium position close to the laser focus (58).

Apart from simple trapping, a system that dynamically manipulates the particle over time and extracts bead information is required for studies of stochastic thermodynamics. Therefore, this chapter describes our experimental apparatuses, focusing on the implementation of modulation and tracking systems, and presents the standard calibra-

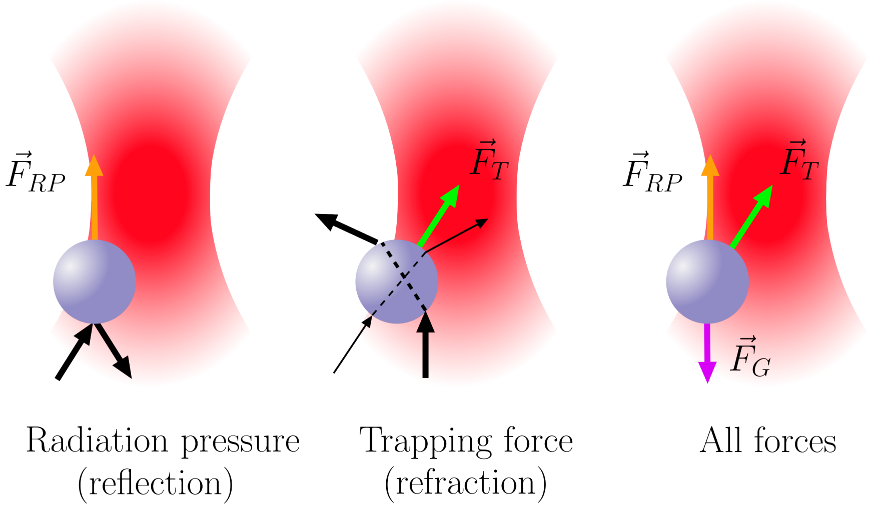

Figure 1 – Basic scheme of the beam's trajectory (black lines) during reflection and refraction and resulting forces, i.e., radiation pressure and trapping force, respectively. Gravitational force, generally negligible, is also represented. The thicker and thinner arrows indicate the position-dependent intensity of the Gaussian beam.

Source: By the author.

tion techniques (8) and the final calibration curves fundamental for characterizing our systems.

3.1 Experimental apparatuses

This research was developed with the collaboration of two laboratories: one at Instituto de Física de São Carlos at the University of São Paulo (Setup IFSC-USP) and the other at Laboratoire de Physique from École Normale Supérieure de Lyon (Setup ENS-Lyon). The chapter presents both experimental systems and their particularities. Although data were collected partially in the two setups, the same sample was used to characterize the system and explore stochastic thermodynamics in Chapters 4, 5 and 6. It consists of microsized spheres of silica of 2 μm diameter and 2 g/cm^3 density immersed in water. The concentration of the particle is very low for avoiding collisions so that only one particle can be found in an area of approximately hundreds of squared micrometres. The last Chapter 7 details a different sample that was studied.

3.1.1 Setup IFSC-USP

The Setup IFSC-USP is a homemade system built during the author´s Master's research (63), which has been improved over the last few years. Starting with the trapping path, a Mephisto 2000NE 1064 nm infrared laser was collimated and size-reduced with a two-lens telescope to approximately 1 mm diameter for increasing the efficiency of the acoustic-optic modulator (AOM) that follows it. An AOM IntraAction ATM-901A2 fed by a homemade voltage-controlled oscillator (VCO) circuit that generates and amplifies the input radiofrequency (RF) signal was used. The first order of diffraction is guided to an Olympus UPlanFL (NA = 1.3) 100x oil immersion objective focusing on the sample. A telescope is then placed between them to magnify and collimate the beam and fill the objective entrance (6 mm diameter) benefitting from its high numerical aperture. Part of the light is deviated and focalized in a homemade photodetector (PD) to monitor the beam intensity and a high-pass filter is placed before it to avoid undesired light. Since the distance between the PD and the AOM is sufficiently high, only the first order is monitored.

After the exit of the objective, a sample holder coupled to a Thorlabs NanoMax 3003D nanopositioning stage controls the position of the sample, which fills a "U-type cell" shown (inset) in Fig. 2. The cell consists of a slide sealed with a coverslip that uses a Gene Frame to control the thickness of the chamber. The slide is glued to a glass cylinder to decrease the height of the central region where the particle is trapped. This avoids collisions of the trapped particle with other beads and enables long measurements with no interruptions.

A Firefly MV USB CCD camera (bright field imaging) and a white LED are used for the visualization of the particles of interest. Since high-speed particle tracking is required, a Thorlabs PDQ80A quadrant photodiode detector (QPD) was added. A low power 532 nm probe laser aligned in the optical path with the aid of a dichroic mirror illuminates the particle in the acquisition system and a telescope collimates and decreases the original beam to approximately 1 mm for minimising possible optical forces. The green light passes through the objective and the outgoing light is collected by an Olympus Plan N (NA = 0.25) 10x condenser and aligned in the centre of the QPD. A lens placed between the condenser and the QPD controls the beam size and a filter blocks the trapping laser light, allowing only the probe laser to reach the detection device.

A high-speed multi-function data acquisition (DAQ) board from National Instruments, PCI6259, performs both AOM control and QPD and PD reading.

3.1.2 Setup ENS-Lyon

The Setup ENS-Lyon scheme, shown in Fig. 3, is similar to the previous one and its subtle differences are described in what follows.

The FORTE 02163 1064-SLM (supply 93580 LD 3000 Laser Quantum) trapping laser also has a 1064 nm wavelength; however, it passes through two perpendicular acousto-optic deflectors (AODs). It is used here the Optoelectronic DTSXY model, which is fed by two RF signals generated by the function generator Tektronix AFG3102. Its external channels enable the control of the RF signal's amplitude and frequency, which, before entering the AODs, are amplified in a homemade circuit. The objective is a 63× immersion Leica Germany HCX PL APO (NA = 1.32) and a Mikrotron MC 1310 cam-

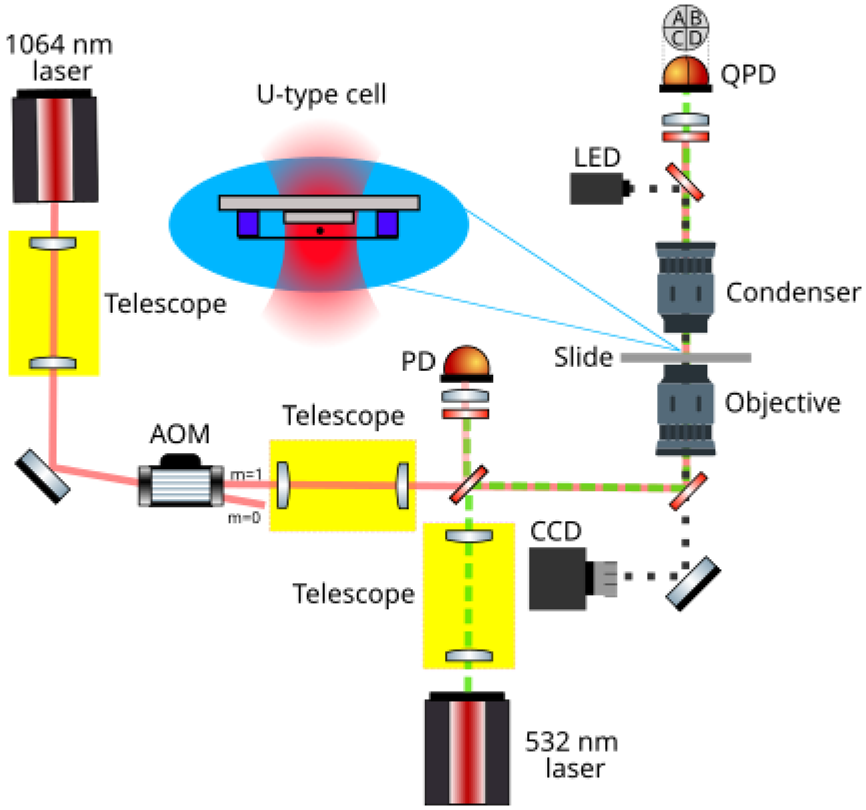

Figure 2 – Simplified description of the Setup IFSC-USP. The trapping system comprises a 1064 nm infrared laser controlled by an AOM. A telescope decreases the beam waist to increase the AOM efficiency, and another enlarges it again to fill the objective entrance. A 532 nm probing laser is aligned with the trapping laser in the detection system and a condenser collects the green scattered light, directs it through a lens to reduce its size, and then sends it to the QPD. Additionally, a white LED and a CCD camera are used for visualizations of the particle. Mirrors and dichroic filters guide the beams. Inset is shown the type of cell used in the experiment in order to acquire long measurements.

Source: By the author.

era and a homemade QPD are used for tracking system. For the QPD functioning, the Thorlabs LP785 probe laser with 785 nm wavelength and the condenser Leica 521500 (NA = 0.53) are aligned in the optical path. A high-speed multi-function data acquisition (DAQ) board, PXI 4472, was employed to read and control the system. No extra telescopes were necessary since lenses coupled in the laser optical fibre outputs collimate and control the beam sizes. The dichroic mirror responsible for joining both lasers is a low-pass filter, and an interferometric filter avoids trapping light from reaching the QPD. A high-pass filter blocks the detection beam in the PD entrance.

The following sections detail the functioning and calibration of the modulation and tracking systems. Since both experimental configurations are similar, the calibration curves for Setup ENS-Lyon are shown to prevent redundancy.

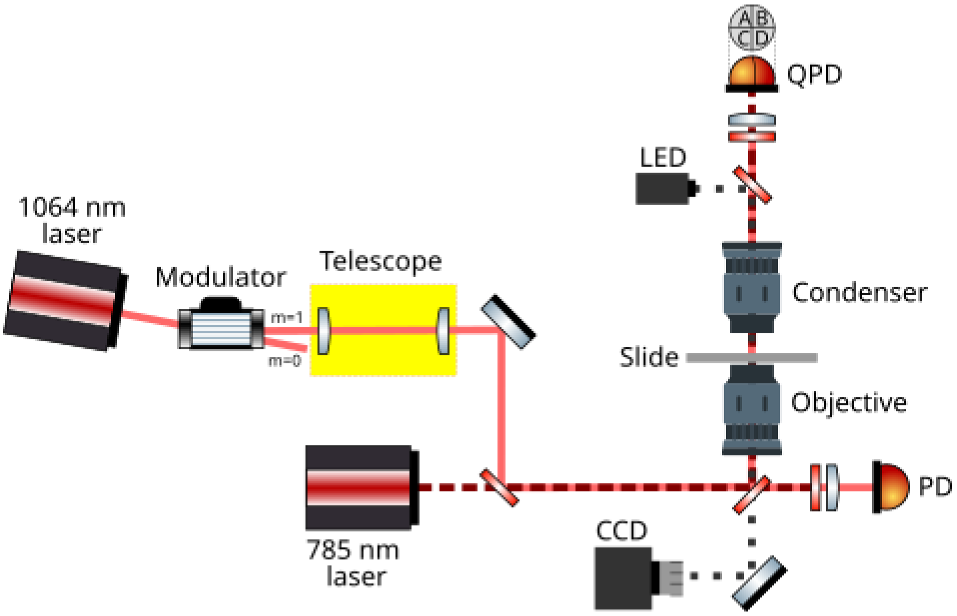

Figure 3 – Simplified description of the Setup ENS-Lyon. The trapping system comprises a 1064 nm infrared laser connected to a set of two perpendicular AODs and a telescope enlarges the beam waist and fills the objective entrance. A 785 nm probing laser is aligned with the trapping laser in the detection system and a condenser collects the red scattered light, directs it through a lens to reduce its size, and then sends it to the QPD. A white LED and a CCD camera are used for the visualization of the particle. Mirrors and dichroic filters guide the beams.

Source: By the author.

3.1.3 Modulation system

As addressed in the previous section, an AOM is used in the Setup IFSC-USP, and a set of two perpendicular AODs is employed in the Setup ENS-Lyon for modulating the trapping laser beam. In such modulators, an RF signal feeds a piezoelectric actuator coupled to a crystal, which induces the propagation of acoustic waves through the material and the establishment of standing waves. When the laser light passes perpendicularly through this device, it diffracts (64).

By controlling the modulator's alignment in the optical path, one lets the biggest intensity in the first order of diffraction ($m = \pm 1$) since this beam has the biggest energetic efficiency and can be modulated by controlling the RF driver. Basically, its intensity can be decreased through the control of the power output of the signal and its angular position can be slightly deviated through the modulation of its frequency. Whereas AOD is designed for a precise spatial control of the output beam, AOM focuses on a precise control of the beam intensity. However, an AOM and an AOD are intrinsically the same, depending only on how the RF driver is manipulated. In both experimental setups, the amplitude and frequency of RF can be controlled and the response is approximately the same. The main difference is that two AODs enable the control of the beam's angular position in two directions, namely, x and y, whereas a single AOM has only one modulation direction, x.

To characterize the modulators' response to the intensity control, a voltage is applied in the amplitude channel of the RF, which feeds one of the AODs, and the PD output is simultaneously acquired. Here, 10 ramps from -1 V to $+1$ V were applied in the input for avoiding noisy curves[*]. Fig. 4 was obtained from the average of those curves and the data were normalized, i.e., the values were divided by their maximum. The beam could (almost) continuously decrease its intensity until it had been completely turned off in a sinusoidal curve. Therefore, the corresponding laser power (proportional to the PD voltage) for a given input in the amplitude control of the RF can be estimated from a fit without further calibrations.

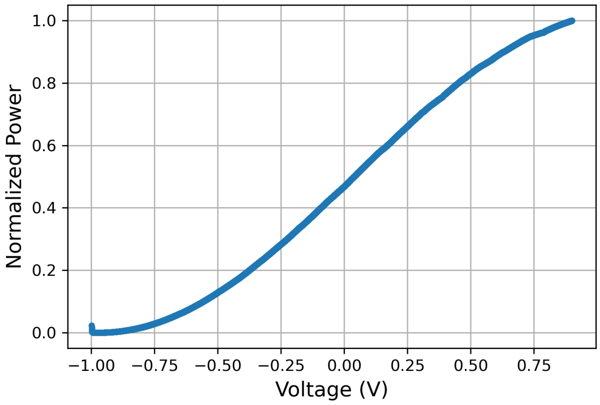

Figure 4 – Normalized power of the infrared laser *versus* voltage applied on the amplitude input control of RF driver. A ramp from -1 V to $+1$ V was applied in the amplitude channel of the RF driver. Data obtained by Setup ENS-Lyon.
Source: By the author.

Since the angular deviation of the first-order beam changes the equilibrium position of the trap, its response in the objective's focal plane can be characterized by tracking a trapped bead while an input signal is applied in the frequency of the RF driver that feeds one of the AODs. A calibrated camera enables estimating the displacement of the particle in the corresponding direction, as shown in Fig. 5[†]. Here, a triangular signal from -1 V to $+1$ V, corresponding to -2 MHz to $+2$ MHz, instead of a ramp, was applied for avoiding discontinuities in the trajectory. The signal was applied in low frequency, 0.1 Hz so that the fluid viscosity would not affect the displacement. A linear regression was performed from the resulting curve of half period of the triangular signal (Fig. 5), and averaging the results for 10 trajectories, one has a calibration factor equal to 971.2 ± 0.4 nm/MHz.

---

[*] The modulating zone for the Setup IFSC-USP ranges from -2 V to -1 V.

[†] To calibrate the camera, we used a glass plate with a grating of 200 lines per millimetre (200 lines/mm). Capturing an image of the central portion of the glass plate and analyzing the distance between the lines in the image, we determined the calibration factor to be 109 nm/pixel.

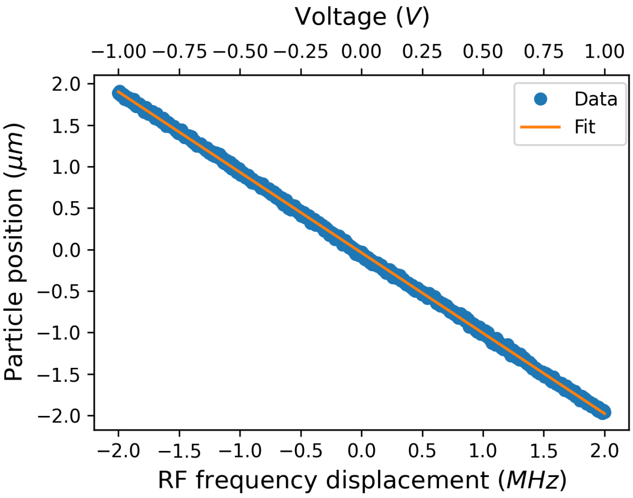

Figure 5 – Position of the trapped bead during the application of an input voltage from -1 V to $+1$ V in the frequency of the RF driver that is equivalent to a deviation from -2 MHz to $+2$ MHz. The frequency of modulation is 0.1 Hz. Since the camera calibration is 109 nm/pixel, the calibration of the modulated laser displacement is 971.2 ± 0.4 nm/MHz for 10 trajectories. A 2 μm trapped silica was used. Data obtained by Setup ENS-Lyon.

Source: By the author.

3.1.4 Tracking system

Although a CCD camera is essential for viewing the sample and tracking the particle, its acquisition rate - in the range of hundreds of frames per second - is considerably slow for stochastic thermodynamics experiments. Therefore, a QPD was implemented to increase both time and spatial resolutions. This device acquires the particle's position up to 150 kHz[‡].

As discussed previously, a second (probe) laser is aligned collinearly with the trapping beam so that the QPD device, which is basically a set of four photodetectors, can be used. Once the particle passes through the probe laser, it creates an interference pattern dependent on its relative position to the spot, as shown in Fig. 6 (left). Therefore, looking at the output signals from the four quadrants of the QPD - where S_{ul} is the up-left, S_{ur} the up-right, S_{dl} the down-left, and S_{dr} the down-right - one can obtain the following signals: $x_{QPD} = (S_{ul} + S_{dl}) - (S_{ur} + S_{dr})$, $y_{QPD} = (S_{ul} + S_{ur}) - (S_{dl} + S_{dr})$, and $SUM_{QPD} = S_{ul} + S_{dl} + S_{ur} + S_{dr}$. Whereas the Setup ENS-Lyon has four channel outputs equivalent to each quadrant, the Setup IFSC-USP has three, which correspond to x_{QPD}, y_{QPD}, and SUM_{QPD}.

As addressed in the previous section, known displacements can be applied in the trapping beam's position for the characterization of the QPD response. However, here, we look to the QPD output signals instead of tracking the particle with the camera. Again, a

---

[‡] Due to DAQ board band limitation, data are usually acquired at 100 kHz.

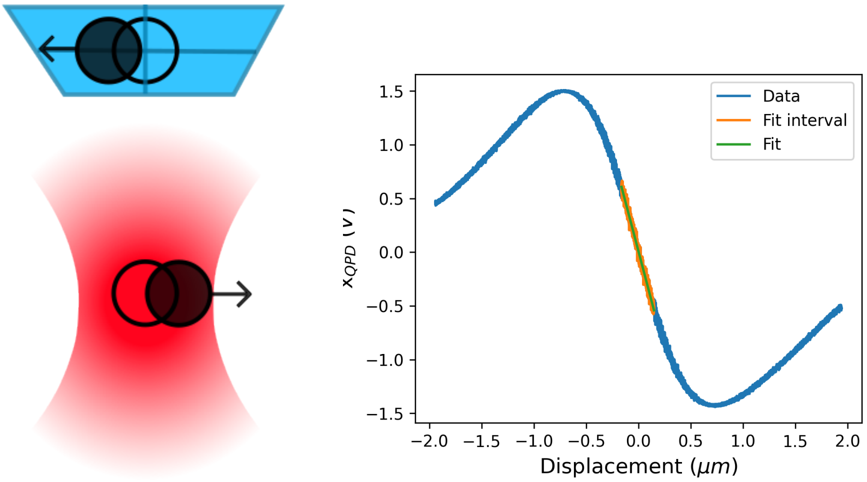

Figure 6 – Scheme of the QPD functioning (left) and QPD signal *versus* displacement of the trapping beam position (right). An input voltage from −1 V to +1 V was applied in the frequency of the RF driver, which is equivalent to a deviation from −2 MHz to +2 MHz. The calibration result from the fit, in green, is 3.698 ± 0.007 V/μm for 10 trajectories. A 2 μm trapped silica was used. Data obtained with Setup ENS-Lyon.

Source: By the author.

triangular signal is applied in the frequency of the RF driver with 0.1 Hz, corresponding to −2 MHz to +2 MHz, and the QPD signals are simultaneously acquired at 100 kHz. The modulation of the RF that feeds the AOD equivalent to the x direction leads to the curve depicted in Fig 6 (right), which shows only one ramp (half of the triangular signal) corresponding to a 3.9 μm beam displacement.

Due to the existence of an offset in the QPD output in function of electronics and a possible misalignment between the trapping and the detection laser, for each file, average value $\langle x_{QDP} \rangle$ is substracted for the original signal. According to Fig 6 (right), x_{QDP} shows a response approximately linear for displacements in the order of particle radius (≈ 1 μm). Therefore, for small displacements around the probing laser spot, the position of the particle in x corresponds to signal x_{QDP} by a calibration factor[§]. Similar results can be obtained for y direction and, depending on the experimental configuration, the perpendicular position, z, can be acquired from the sum of the four quadrants, SUM_{QDP}. However, this is not the focus of this research.

Among the various techniques for the obtaining of the amplification factor, which converts signal in volts to displacement in meters (8), it can be directly calculated from linear regression in the curve shown in Fig. 6 (right). For the presented curve, the sensitivity is equivalent to 3.698 ± 0.007 V/μm. However, this method can be sensible to the region chosen to be fitted. The following sections explore other calibration techniques for obtaining the amplification factor and the trap stiffness of the optical potential.

[§] Since the probe laser has good power stability over time, x_{QDP} is directly used for the obtaining of the particle's position. However, the signal can be normalized by dividing it by sum SUM_{QDP}. Such normalization may add some noise to the data due to the particle movement in z and will not be used.

3.2 Calibration techniques

Simple optical tweezers trap particles close to the laser's focus in approximately harmonic potentials and calculating the theoretical effective force requires the characteristics of the experimental apparatus, e.g., the shape and power of the trapping laser, objective settings, size and material of the sample, and medium where the particle is immersed. However, the optical potential curve can be estimated directly from the measured position of a particle trapped in a static optical trap. This section details some of the standard calibration techniques described in (8).

Although the trapped particle's response depends on several parameters, one will focus on characterising the potential felt by the particle by controlling the trapping beam intensity. A trapped silica microsphere is tracked with the QPD for 30 s at 100 kHz acquisition rate for different laser powers controlled by the amplitude modulation of the RF driver. Data were collected at Setup ENS-Lyon and the results are presented in one direction, x, to avoid redundancy. Similar measurements were performed for Setup IFSC-USP.

3.2.1 Equipartition theorem of energy

Let us start with one of the simplest methods derived from the equipartition theorem of energy. Assuming an optical trap has an approximately harmonic potential with force constant κ, the equipartition theorem states (8),

$$\langle U(x)\rangle = \frac{1}{2}\kappa\langle(x-x_{eq})^2\rangle = \frac{1}{2}k_B T, \tag{3.1}$$

where x_{eq} is the equilibrium position of the trap, k_B is the Boltzmann constant, and T is temperature. The trap stiffness can be obtained from a time series of positions x_j at different instants $j = 1, ..., N$[¶]:

$$\kappa_{EQ} = \frac{k_B T}{\frac{1}{N}\sum_{l=1}^{N}(x_j - x_{eq})^2}, \tag{3.2}$$

where $x_{eq} = \frac{1}{N}\sum_{j=1}^{N} x_j$, since the probability distribution is Gaussian. The method does not require a high acquisition rate to estimate the force constant and can be applied even with a simple camera. However, the amplification factor must be previously acquired for the obtaining of $x = x_{QPD}/S$ from the QPD signal. The result from the least squares fit of the linear region in Fig. 6 (right) was used.

[¶] Note the sub-index in the experimental result of trap stiffness and amplification factor corresponds to the results for each method, namely, equipartition theorem (κ_{EQ}), potential analysis (κ_U), mean squared displacement (κ_{MSD} and S_{MSD}), autocorrelation function (κ_C and S_C), and power spectrum density analysis (κ_{PSD} and S_{PSD}).

Although simple, this method is not the most reliable since possible noise can severely affect the value of $\langle x^2 \rangle$ and consequently the calculated trap stiffness. Moreover, the potential was assumed harmonic. For general cases, the optical potential is estimated from the probability distributions of the particle's positions, as discussed in the next section.

3.2.2 Position histrogram analysis

Under thermal equilibrium conditions, the probability distribution of the bead follows a Maxwell-Boltzmann distribution, according to

$$\rho(x) = \rho_0 \exp\left[- \frac{U(x)}{k_B T} \right], \tag{3.3}$$

where ρ_0 is a normalization factor such that $\int \rho(x)dx = 1$. By solving Eq. 3.3, the potential $U(x)$ can be determined by

$$U(x) = -k_B T \log[\rho(x)] + U_0, \tag{3.4}$$

where U_0 is an arbitrary additive constant.

Therefore, the estimation of the effective optical potential by the method requires the obtaining of the probability distribution from the normalized histogram of positions of a trapped particle[‖], as shown in Fig 7 (left). Since a static trap has an approximately harmonic potential, the probability distribution is expected to be Gaussian:

$$\rho(x) = \rho_0 \exp\left[- \frac{\kappa x^2/2}{k_B T} \right], \tag{3.5}$$

and its width depends on the trap stiffness. The experimental results computed by Eq. 3.4 are shown in Fig 7 (right) for three different laser powers. The force constant, κ_U, can be obtained by a quadratic regression

$$U(x) = \frac{\kappa x^2}{2}. \tag{3.6}$$

As expected, the particle confinement is bigger at higher intensities, resulting in a larger trap stiffness.

Since, in principle, the analysis does not assume the potential is harmonic, it is an interesting procedure to test the hypothesis of the harmonicity of the simple optical

---

[‖] The amplification factor was obtained from the least squares fit of the linear region in Fig. 6 (right).

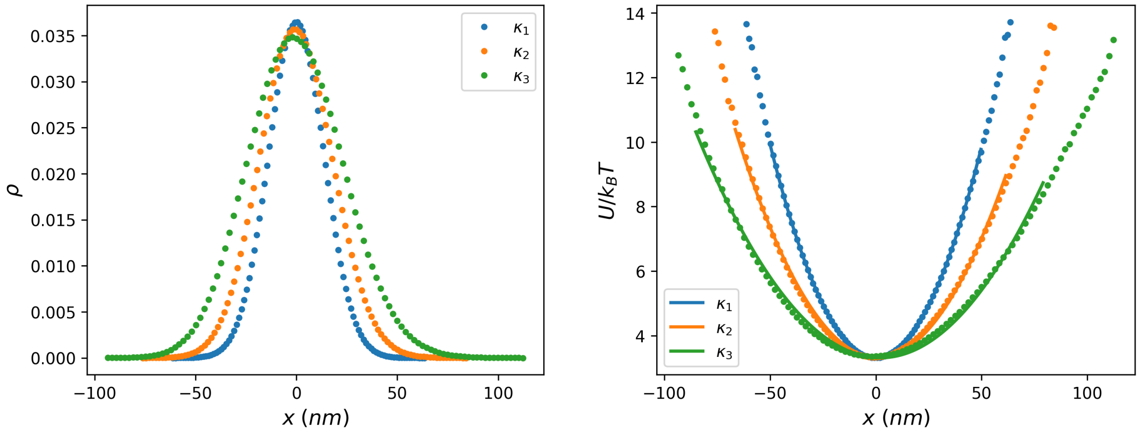

Figure 7 – Position histograms from time series data (left) and resulting potentials (right) corresponding to a 2 μm silica bead trapped with three different force constants ($\kappa_1 > \kappa_2 > \kappa_3$), from highest to lowest in blue, orange, and green, respectively. The fit (solid line) results in $\kappa_U = 21.54 \pm 0.03$, 12.69 ± 0.07 and 7.51 ± 0.07 pN/μm for the potential curve. Average curves of 10 acquisitions collected at 100 kHz for 30 s are presented.

Source: By the author.

tweezers trapping and probe more complex potentials, such as double-wells (65), asymmetric traps, among others. However, the method is also susceptible to noise and requires a previous characterization of the QPD response. Other techniques are discussed in the next section to estimate the trap stiffness and the amplification factor for a full characterization of the system. The particle behavior in a smaller time range enables studies of the autocorrelation function (ACF) and the mean squared displacement (MSD) of a trapped particle, as described in what follows.

3.2.3 Autocorrelation function and mean squared displacement analysis

The autocorrelation function (ACF) measures the correlations of the particle displacement in different instants, i.e., the time necessary for the particle to "forget" its initial position. It is given by (8)

$$C(\tau) = \langle x(t+\tau)x(t)\rangle = \frac{k_BT}{\kappa}e^{-\frac{|\tau|}{\tau_{exp}}}, \tag{3.7}$$

where $\tau_{exp} = \gamma_{exp}/\kappa$ is the decay time.

With a position time series $x_{QPD,j}$, measured directly in volts** with a given sampling frequency f_s, the discrete ACF (8) must be used:

$$C_k = \frac{1}{N-k}\sum_{j-1}^{N-k} x_{QPD,j+k}x_{QPD,j}, \tag{3.8}$$

where $\tau_k = k\Delta t$ and $\Delta t = 1/f_s$. The ACF curves are shown in Fig. 8 (left) for three different laser powers. The least squares fit provides the trap stiffness, κ_C, and the amplification

---

** The QPD signal requires no conversion to meters by previous calibration.

factor, $S_C = \sqrt{\gamma/\gamma_{exp}}$. Note the amplification factor is obtained from the experimental value of the decay time.

In contrast, the mean squared displacement (MSD) quantifies the movement of a particle from its initial position at a time τ given by (8),

$$MSD(\tau) = \langle \Big[x(t+\tau) - x(t)\Big]^2 \rangle = 2\frac{k_B T}{\kappa}\Big(1 - e^{-\frac{|\tau|}{\tau_{exp}}}\Big). \tag{3.9}$$

Discretizing Eq. 3.9 for the position time series also measured directly in volts,

$$MSD_k = \frac{1}{N-k}\sum_{j-1}^{N-k}\Big[x_{QPD,j+k} - x_{QPD,j}\Big]^2, \tag{3.10}$$

leads to the results shown in Fig. 8 (right). The curve shows the transition from linear growth due to free diffusion behavior for times shorter than the relaxation time to a plateau due to the trapping force for longer times. Here, the trap stiffness, κ_{MSD}, obtained by least squares, is inversely proportional to the height of the plateau. The amplification factor S_{MSD} can also be obtained from the exponential time, as described for the ACF method.

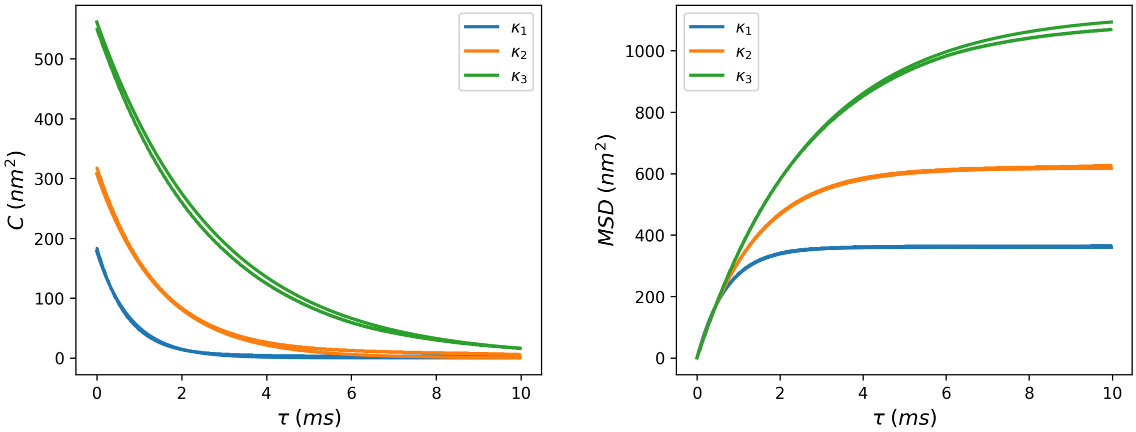

Figure 8 – Autocorrelation (left) and mean squared displacement (right) corresponding to a 2 μm silica bead trapped with three different force constants ($\kappa_1 > \kappa_2 > \kappa_3$), from highest to lowest in blue, orange, and green, respectively. The fit (solid line) results in $\kappa_C = 22.6 \pm 0.1$, 13.08 ± 0.02 and 7.170 ± 0.003 pN/μm and $S_C = 3.659 \pm 0.014$, 3.510 ± 0.004 and 3.4656 ± 0.0011 V/μm for the autocorrelation and $\kappa_{MSD} = 22.379 \pm 0.003$, 13.048 ± 0.002 and 7.1711 ± 0.0014 pN/μm and $S_{MSD} = 3.888 \pm 0.002$, 3.6123 ± 0.0011 and 3.5001 ± 0.0011 V/μm for the mean squared displacement. Average curves of 10 acquisitions collected at 100 kHz for 30 s. Both graphs are rescaled considering the amplification factor obtained for each curve.

Source: By the author.

Both methods require no previous calibration of the amplification factor. Nevertheless, they are still highly affected by noise present in data since one looks at the time domain. To contour this situation, one discusses a last method that analyses the position after a Fourier transform, the power spectrum density (PSD) analysis (8). Afterwards, we compare the results from all the different methods presented in this section.

3.2.4 Power spectrum density analysis

The basic procedure of the Power Spectrum Density (PSD) analysis is to convert the position time series of a trapped particle, $x_{QPD,j}$, to the frequency domain. Here, $x_{QPD,j} = x_{QPD}(t_j)$, where $t_j = j\Delta t$ being $j = 1, ..., N$ and $\Delta t = 1/f_s$, since data are collected at a given sampling frequency f_s for a total time T_s. A discrete Fourier transform applied in the trajectory yields[††] (8)

$$\tilde{x}_k = \Delta t \sum_{j=1}^{N} e^{i2\pi f_k t_j} x_{QPD,j}, \tag{3.11}$$

where $f_k = k/T_s$ and $k = -N/2 + 1, ..., N/2$. Then, the PSD, given by $\mathrm{PSD}_k = |\tilde{x}_k|^2/T_s$ (8), can be calculated.

Alternatively, PSD can be computed by the function *scipy.signal.welch* on Python. As described in (66), Welch's technique calculates an estimation of the power spectral density through a process that involves segmenting the data with overlaps, generating a modified periodogram for each segment, and subsequently averaging those individual periodograms. The final result is shown in Fig. 9.

The simple theoretical curve for PSD is equivalent to (8):

$$\mathrm{PSD}(f) = \frac{D_{exp}/(2\pi^2)}{f_c^2 + f}, \tag{3.12}$$

where D_{exp} is the experimental diffusion coefficient and $f_c = \kappa(2\pi\gamma)^{-1}$ is the corner frequency. From the least squares fit, we can obtain the trap stiffness and the amplification factor, $\sqrt{D_{exp}/D}$[‡‡].

However, data around f_c must be selected so that the fit can be performed. The outgoing results are very sensitive to the chosen window and the expression starts to be inefficient in characterizing bigger particles such as the ones reported in Chapter 7. Therefore, a more general model that takes into account the memory effects and the inertial term is used in this study. Reference (43) provides a complete description of this model. According to (67), memory effect should be considered for trap calibration at around 200 kHz sampling frequency and although one works with less time resolution, this approach was implemented since one needs a very accurate calibration of the potential felt by the particle.

[††] The position in the frequency domain is denoted by $\tilde{x}_k$; however, here $\tilde{x}_k \equiv \tilde{x}_{QPD,k}$. After the amplification factor has been obtained, the curve is rescaled.

[‡‡] Here, $D = k_B T/\gamma$.

Considering that the PSD, for $\omega = 2\pi f$, is given by the fluctuation-dissipation theorem (43):

$$\mathrm{PSD}(\omega) = 2k_BT\frac{\mathrm{Im}(\tilde{\chi}(\omega))}{\omega}, \tag{3.13}$$

where $\tilde{\chi}(\omega)$ is presented in Eq. 2.20 and $\tilde{\gamma}(\omega)$ is provided in Eq. 2.21. Therefore,

$$\mathrm{PSD}(\omega) = S^2 4k_BT\frac{\gamma_\omega}{(-m_p\omega^2 + \kappa + \gamma\sqrt{\tau_f/2}\omega^{3/2})^2 + (\gamma_\omega\omega)^2} + B. \tag{3.14}$$

Here, $\gamma_\omega = \gamma(1+\sqrt{\omega\tau_f/2})$, S is the amplification factor (since the PSD is obtained for the position signal in volts directly from the QPD), and B is the background that represents the smallest detectable movement in the system and determines its spatial resolution. Therefore, the amplification factor, S_{PSD}, and trap stiffness, κ_{PSD}, are obtained directly from the fit. The results are shown in Fig. 9.

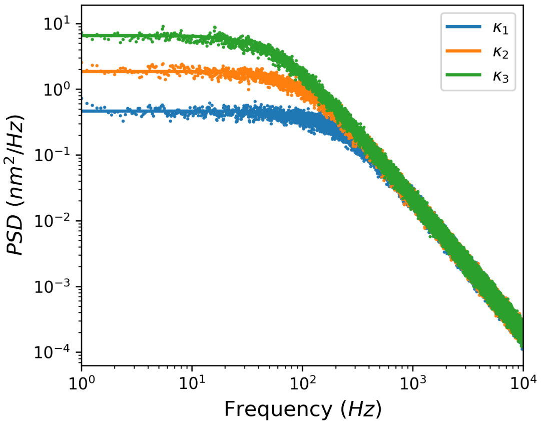

Figure 9 – Power spectrum density analysis corresponding to a 2 μm silica bead trapped for three different force constants ($\kappa_1 > \kappa_2 > \kappa_3$), from highest to lowest in blue, orange, and green, respectively. The fit (solid line) results in κ_{PSD} = 25.195, 12.589 and 6.710 pN/μm and S_{PSD} = 4.029, 3.709 and 3.560 V/μm. Average curves of 10 acquisition files collected at 100 kHz for 30 s each. The length of the Fast Fourier Transform (FFT) is $N_{FFT} = 8\ 10^5$. The graphs are rescaled considering the amplification factor obtained for each curve.

Source: By the author.

3.2.5 Comparison between calibration techniques

As discussed previously, the intensity of the trapping laser affects the confinement of the particle and a linear growth of the trap stiffness is expected as the intensity increases (8). The results for several laser intensities (linearly proportional to PD readings by a constant) are shown in Fig. 10 (left).

The relationship between the force constant obtained experimentally and the beam power is approximately linear for the PSD analysis method; however, for other methods, a deviation is observed as trap stiffness increases. Since the PSD theoretical model analyses

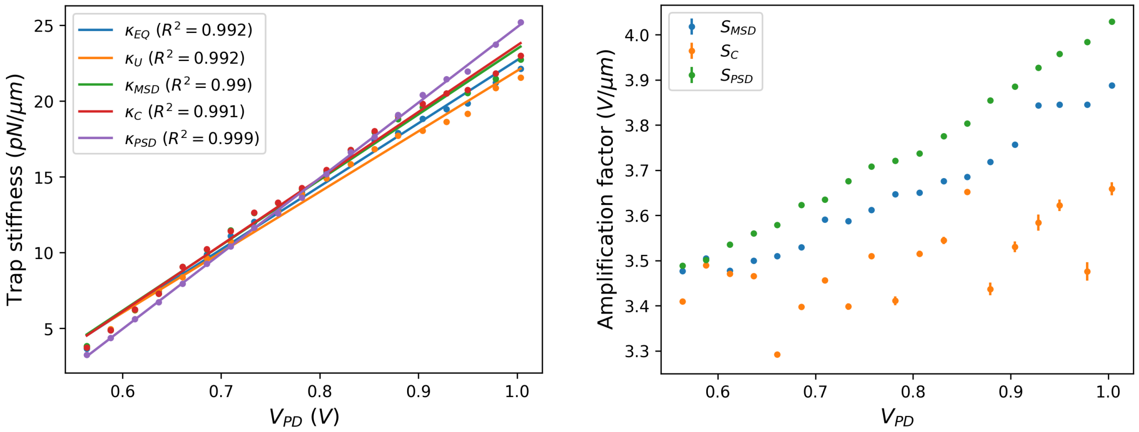

Figure 10 – Calibration curves for trap stiffness (right) and amplification factor (left) as a function of PD voltage, which is linearly proportional to the trapping beam intensity. For trap stiffness curves, one has the equipartition method in blue, potential analysis in orange, mean squared displacement in green, autocorrelation function in red and power spectrum density in purple. For the amplification factor, the mean squared displacement is blue, the autocorrelation function is orange, and the power spectrum density is green. The uncertainties are smaller than the dots.

Source: By the author.

the particle's natural thermal fluctuations in a delimited frequency window and the noise does not affect it directly, it can provide reliable results explaining the best value R^2 for the fit, which is the closest to one.

No significant noise was observed in the PSD spectrum in the data for the Setup ENS-Lyon; however, even for noisier systems such as the Setup IFSC-USP, whose PSD is provided in Appendix B, noise peaks can be easily identified and eliminated if necessary.

In addition to reliably characterizing the force constant, PSD offers less dispersed points for the amplification coefficient calibration, which clearly depends on the beam power. Such dependency can occur due to the increase in the radiation pressure when the power increases; consequently, the particle is pushed up in the direction of the laser's propagation. When the z position changes, QPD can become more or less sensitive to the bead's movement, thus affecting the amplification factor.

Given such an extensive comparative analysis, the PSD method was used for all calibrations in this research.

4 ENERGETICS OF THERMODYNAMIC PROCESSES

As discussed in the previous section, a simple optical tweezer system enables the trapping and manipulation of microscopic particles, thus being an ideal platform for studies of stochastic thermodynamics. Although, in general, the optical potential is approximately harmonic, the modulation of the trapping laser promotes the creation of various trapping shapes, which range from the basic control of the trap stiffness or equilibrium position to more complex configurations, such as double-wells (50), optical lattices (68) among others.

This chapter focuses on a straightforward case of compression of the potential via laser intensity control. The experimental application of this type of protocol enables studies of energy exchanges between the particle and the surroundings towards exploring the First Law of Thermodynamics and Fluctuation Theorems.

Firstly, the model of the protocol and its translation in our experimental apparatus are introduced, followed by calculations of stochastic thermodynamic quantities, such as work, heat, and internal energy. The experimental and theoretical expected values for those quantities are then compared. Finally, the experimental verification of Jarzynski's equality and Crooks's theorem is demonstrated and the conclusions are discussed*.

4.1 Isothermal compression in optical tweezers

One of the most ubiquitous experiments in thermodynamics textbooks is the illustration of piston compression and expansion (1). The problem involves a vessel containing an ideal gas with a large number of particles. The container is closed with a movable frictionless piston that slides up and down, as shown in Fig. 11. To decrease the container volume from equilibrium, work must be injected into the system by pushing the piston down; conversely, the system generates work during expansion. Therefore, in this model, our control parameter, which can change the state of the particles in the vessel, is the position of the piston.

Let us now consider a single particle gas in the container. In this regime, the work associated with the compression and expansion of the piston will be subject to strong fluctuations, as discussed in Sec. 2.2. By analogy, a possible way to analyze the problem is by considering a single particle in a controllable confined potential, which is exactly the

---

* All data presented in what follows correspond to one dimension and were acquired with Setup ENS-Lyon. The same experiments, with very similar results, were conducted at São Carlos in two different setups. However, since mechanical noise in the first version and (most likely) electronic high-frequency noise in the second made the noise figures and uncertainties slightly higher, the best results are shown.

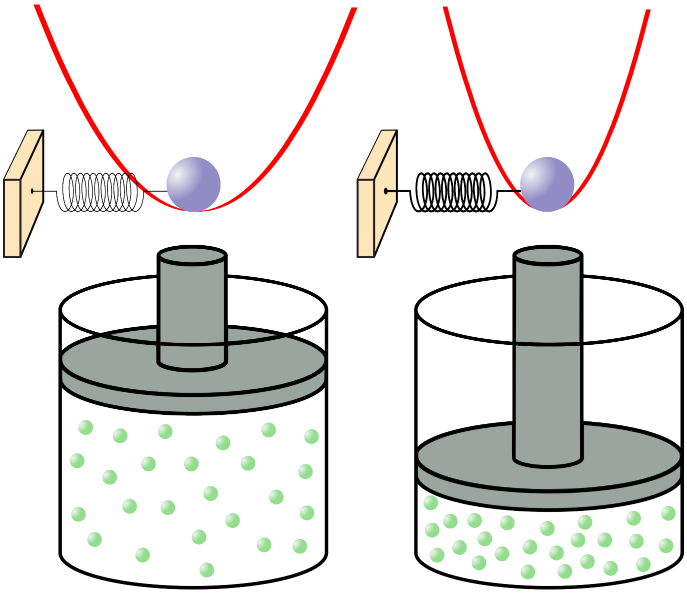

Figure 11 – Scheme of a piston with two different volumes and analogy with a particle trapped in a harmonic potential with two different trap stiffnesses.
Source: By the author.

model of an optical tweezer. On this scale, the bead is subject to thermal fluctuations from the surroundings and its probability density function can be "compressed" or "expanded" by changing, for example, the force constant of the trap (see Sec. 3.2). Then, here the control parameter is $\lambda(t) = \kappa(t)$ (see Chapter 3). Although different $\lambda(t)$ curves can be explored, this chapter focuses on one of the simplest protocols, the linear one, for testing the main principles involved in this research.

4.1.1 Linear protocol description

In linear protocols, the particle starts in equilibrium state $\lambda(0) = \lambda_i$ and goes to $\lambda(\tau_P) = \lambda_f$, according to the following equation:

$$\lambda(t) = \lambda_i + \frac{\Delta\lambda}{\tau_P} t, \tag{4.1}$$

where $\Delta\lambda = \lambda_f - \lambda_i$ is the modulation amplitude and τ_P is the protocol time. For $\Delta\lambda > 0$, one has the compression protocol, and for $\Delta\lambda < 0$, the expansion one. Since the optical potential is harmonic, $U = \lambda x^2/2$, the time dependency of work, heat, and internal energy difference can be written as (see Sec. 2.3.3)

$$W(t) = \frac{1}{2}\int_0^t dt' \frac{d\lambda(t')}{dt'} x(t')^2, \tag{4.2}$$

$$Q(t) = \int_0^t dt' F \frac{dx(t')}{dt'}, \text{with} F = -\lambda(t')x(t'), \tag{4.3}$$

$$\Delta E(t) = \frac{1}{2}(\lambda(t)x(t)^2 - \lambda(0)x(0)^2). \tag{4.4}$$

Since the particle's trajectory has a stochastic behavior, a given protocol $\lambda(t)$ must be applied several times and the distribution of values obtained for energetics - work, heat and internal energy - can be computed. The following paragraphs present the theoretical predictions of free energy difference and average values of energetics for their comparisons with the experimental results.

For a harmonic potential, the partition function of a given state is given by

$$\begin{aligned} Z &= \int_{-\infty}^{+\infty} dx e^{-U/k_B T} \\ &= \int_{-\infty}^{+\infty} dx e^{-(\lambda x^2/2)/k_B T} \\ &= \sqrt{\frac{\pi}{\lambda/2k_B T}}. \end{aligned} \tag{4.5}$$

Therefore, the Helmholtz free energy associated with λ is

$$F = -k_B T \ln(Z(\lambda)), \tag{4.6}$$

and the free energy difference between two equilibrium states, λ_i and λ_f, can be written as

$$\Delta F = F_f - F_i = -k_B T \ln \sqrt{\frac{\lambda_i}{\lambda_f}}. \tag{4.7}$$

The free energy difference is the minimum amount of energy necessary to take the system from one state to the other and is reached in quasistatic processes. However, to compute the average energy dissipated in a finite-time process, the trajectory of the particle must be considered. According to (69), the average work for an ensemble of trajectories of a linear protocol is given by

$$\langle W \rangle = \int_0^{\tau_P} dt \dot{\lambda} \langle \frac{\partial U(x,\lambda)}{\partial \lambda} \rangle = \frac{\Delta \lambda}{2\tau_P} \int_0^{\tau_P} dt \langle x^2 \rangle. \tag{4.8}$$

The value of $w \equiv \langle x^2 \rangle = \int_{-\infty}^{+\infty} dx P(x,t) x^2$ can be directly calculated by the Fokker-Plank equation (Eq. 2.22):

$$\frac{dw}{dt} = \frac{-2\lambda(t)}{\gamma} w + \frac{2k_B T}{\gamma}. \tag{4.9}$$

The initial condition can be obtained from the equipartition theorem of energy, $w(0) = \langle x^2(0) \rangle = k_B T/\lambda_i$ (Sec. 3.2.1). From the result of Eq. 4.9, which gives the time evolution of $\langle x^2 \rangle$ depicted in Fig. 12, the average work can be obtained by integrating it in Eq. 4.8.

The internal energy is given by Eq. 4.4; therefore, its mean value can be obtained by

$$\langle \Delta E \rangle = \frac{1}{2}(\lambda(t)\langle x(t)^2 \rangle - \lambda(0)\langle x(0)^2 \rangle). \tag{4.10}$$

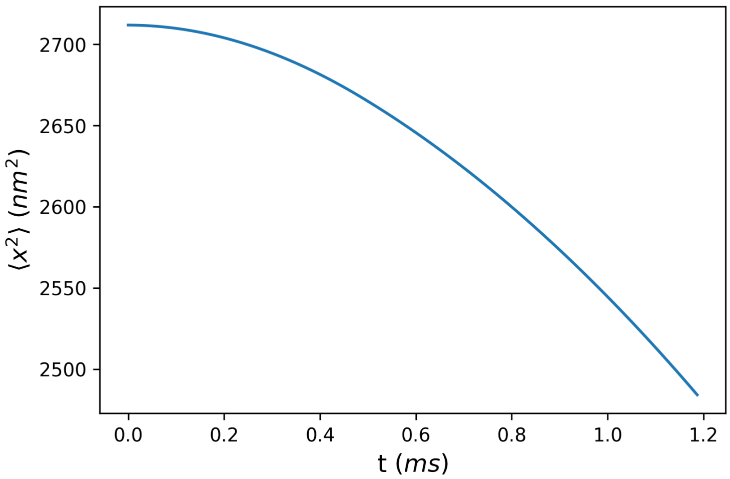

Figure 12 – Time evolution of $w(t)$ for $\Delta\lambda = 10\lambda_i$, $\lambda_i = 1.5\ pN/\mu m$, and $\tau_P = 0.1\tau_R$, where $\tau_R = \gamma/\lambda_i \approx 12$ ms is the relaxation time in the state λ_i.
Source: By the author.

Here, $\langle x^2 \rangle$ can also be obtained by Eq. 4.9. However, if the initial and final states are in equilibrium, from the equipartition theorem, one has $\langle \Delta E \rangle = 0$. The derivations of $\langle W \rangle$ and $\langle \Delta E \rangle$, enable obtaining the expected value for the average of heat, $\langle Q \rangle = \langle W \rangle - \langle \Delta E \rangle$, considering the First Law of Thermodynamics (Eq. 2.1).

4.2 Protocol application

The first step, performed before any protocol application, is to characterize the bead's response to different laser powers. The methodology described in Sec. 3.2.4 is, therefore, applied for each trapped particle. Using the PSD analysis, the trap stiffness, κ_x, and amplification factor, S_x, are obtained, as presented in Fig. 13.

Besides the characterization of κ_x and S_x, the trapping beam response as a function of PD voltage (linearly proportional to the trapping laser power) must be calibrated for the RF driver's amplitude channel control, addressed in Sec. 3.1.3. Then, applying a general control parameter curve, $\lambda_{theo}(t)$, will be equivalent to acquiring an expected response in the PD reading, V_{PD}. The obtaining of such an expected PD output requires the application of an input signal in the amplitude channel of the RF's driver that feeds one of the AODs, V_{AOD}, as shown in Fig. 14. The example demonstrates the application of two types of linear protocols, namely, compressing (forward), from λ_i to λ_f, followed by the expanding (reverse) one, from λ_f to λ_i, where $\lambda_i < \lambda_f$.

Since the particle must be in thermal equilibrium at the beginning of each protocol, during a time interval, τ_{eq}, longer than the relaxation time, $\tau_R = \gamma/\lambda_i$, the laser power is kept at a constant value equivalent to the initial state λ_i. The protocol is then applied, thus changing the state to trap stiffness λ_f. After thermalization of the particle in λ_f, the expanding protocol is run (see Fig. 14) and the loop finishes in the initial state, λ_i. The

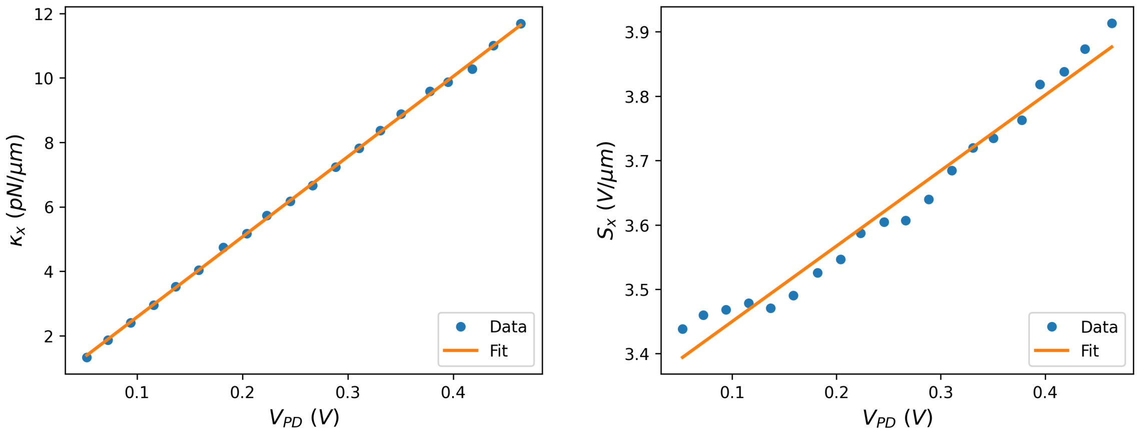

Figure 13 – Calibration curves for trap stiffness (left) and amplification factor (right) from PSD fits as a function of PD voltage. The PD voltage is linearly proportional to the trapping beam intensity. The slope is $m_{TS} = 24.89 \pm 0.14$ (pN/μm)/V and y-intercept is $b_{TS} = 0.09 \pm 0.04$ pN/μm for the trap stiffness calibration. The slope is $m_S = 1.17 \pm 0.05$ (V/μm)/V and y-intercept is $b_S = 3.333 \pm 0.014$ V/μm for the amplification factor calibration.
Source: By the author.

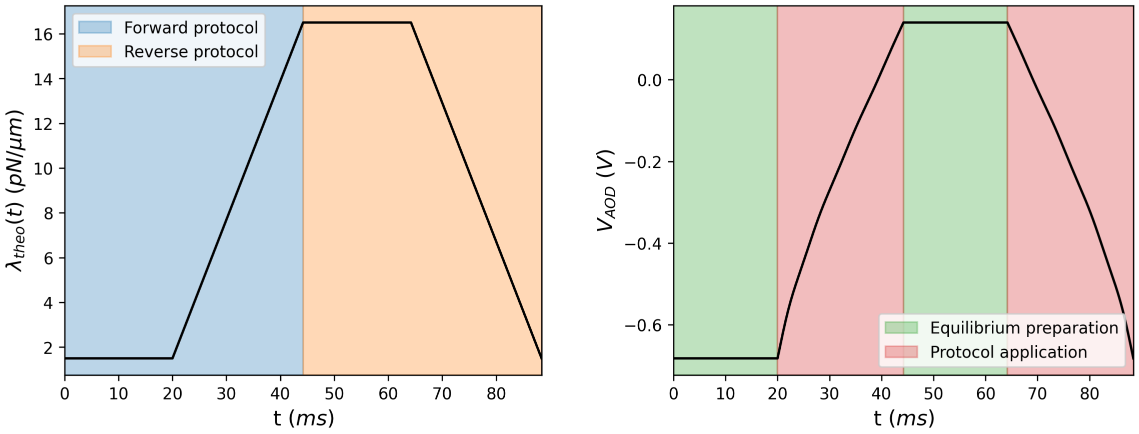

Figure 14 – Theoretical control parameter $\lambda_{theo}(t)$ (left) for a procedure with a compressing (forward) protocol, in blue, followed by an expanding (reverse) one, in orange, and corresponding voltage applied in the amplitude of RF's driver (right). Firstly, the particle is thermalized for an equilibrium time, τ_{eq}, in green, and then the linear protocol is applied in a time duration τ_P, in red. Here, $\tau_{eq} = 20$ ms, $\lambda_i = 1.5\ pN/\mu m$, $\Delta\lambda = 10\lambda_i$, and $\tau_P = 2\tau_R$, where $\tau_R = \gamma/\lambda_i \approx 12$ ms is the relaxation time in the state λ_i.
Source: By the author.

procedure is repeated ten thousand times for each set of parameters.

The simultaneous acquisition of the QPD output in one axis, x_{QPD}, and the infrared PD signal, V_{PD}, during the experiment enable obtaining the position of the centre of mass and the control parameter. Here, $x = V_{QPD}/S_x$, where the dependency of the amplification factor on the laser intensity is $S_{fit,x} = m_S V_{PD} + b_S$ where m_S and b_S are the slope and y-intercept obtained from the linear fit in Fig. 13 (right). Since the particle starts the protocol in the laser intensity corresponding to PD voltage $\langle V_{PD,eq}\rangle$, i.e. the average of the PD voltage during the equilibrium time, the initial amplification factor is given by $S_{fit,x} = m_S\langle V_{PD,eq}\rangle + b_S$. Although the particle can move in z direction due to the radiation pressure dependency on the laser intensity, as discussed in 3.2.5, we consider here that the particle remains with this amplification factor during all the protocol interval. Additionally, the estimated trap stiffness is obtained from $\lambda \equiv \kappa_{exp} = m_{TS}V_{PD} + b_{TS}$ where m_{TS} and b_{TS} are the slope and y-intercept obtained from the linear fit shown in Fig. 13 (left).

Due to a delay between modulation and acquisition, an analysis of the PD signal is performed for each file to detect the starting point of the loop sequence, as discussed in Appendix A.

The experiment design enables the control of different parameters, such as modulation amplitude and protocol time. Fig. 15 shows two compressing linear protocols, i.e. $\lambda_f > \lambda_i$, with the same modulation amplitude, $\Delta\lambda = 10\lambda_i$, and different protocol times: one completely out of equilibrium with $\tau_P = 0.1\tau_R$ (left) and the other closer to the equilibrium regime with $\tau_P = 2\tau_R$ (right). The particle trajectories clearly show the movement of the particle being compressed when the laser is taken to a higher intensity, as in the case of the piston experiment. This behavior is also depicted in Fig. 16, which shows the position histograms of the particle at different instants. While the equilibrium state is prepared, the probability distributions begin to broaden until thermalize (after approximately the relaxation time). Then, the protocol is applied, and the particle becomes more confined again. The reconstructed experimental outputs, x and λ, can be used now in calculations of quantities such as work, heat, and internal energy.

4.3 Experimental results

In the experiments, the data are usually acquired in a regular time interval $\Delta t = 10^{-5}$ s, enabling the discretization of the integrals of Eqs. 4.2 and 4.3. Therefore, the energetics during a protocol with duration $\tau_P = N\Delta t$, where $t_j = j\Delta t$ and $n = 0, 1, 2, ..., N$ are

$$W_n = \frac{1}{2}\Delta t\sum_{j=0}^{n-1}\frac{\lambda_{j+1}-\lambda_j}{\Delta t}x_j^2 = \frac{1}{2}\sum_{j=0}^{n-1}(\lambda_{j+1}-\lambda_j)x_j^2, \tag{4.11}$$

$$Q_n = \Delta t\sum_{j=0}^{n-1}\frac{(x_{j+1}-x_j)}{\Delta t}F(\bar{x}) = -\sum_{j=0}^{n-1}(x_{j+1}-x_j)\lambda_j\frac{x_{j+1}+x_j}{2} = -\frac{1}{2}\sum_{j=0}^{n-1}\lambda_j(x_{j+1}^2-x_j^2), \tag{4.12}$$

with $F(\bar{x}) = -\lambda_j(x_j + x_{j+1})/2$,

$$\Delta E_n = \frac{1}{2}(\lambda_n x_n^2 - \lambda_0 x_0^2), \tag{4.13}$$

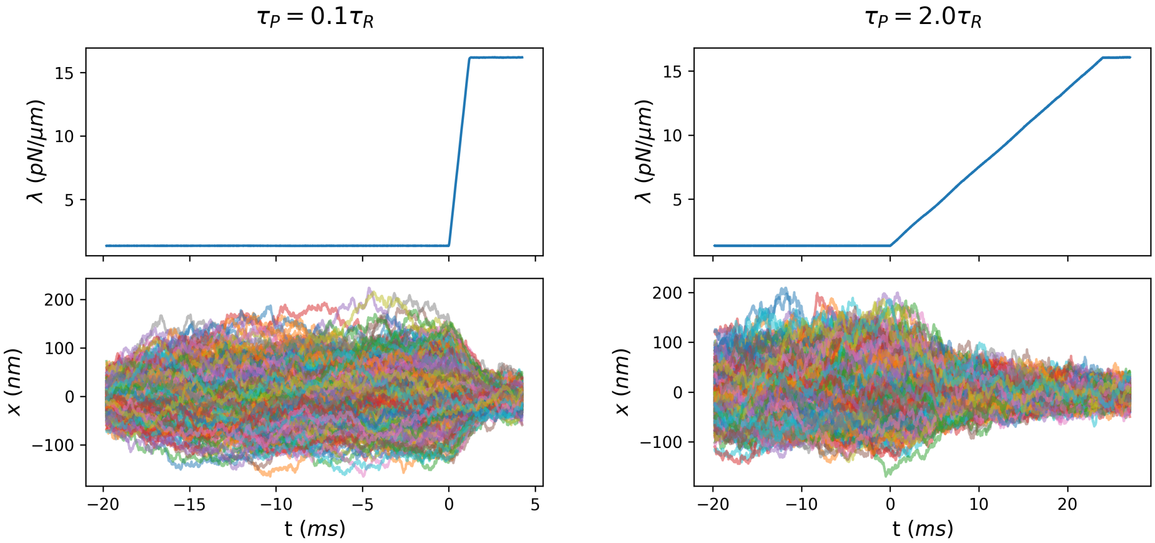

Figure 15 – Estimated trap stiffness (top) and 500 trajectories (bottom) for a compressing linear protocol with $\tau_{eq} = 20$ ms, $\lambda_i = 1.5\ pN/\mu m$, $\Delta\lambda = 10\lambda_i$ and different protocol times: $\tau_P = 0.1\tau_R$ (left) and $\tau_P = 2\tau_R$ (right), where $\tau_R = \gamma/\lambda_i \approx 12$ ms is the relaxation time in the state λ_i.

Source: By the author.

where Stratonovich convention was applied to discretize the integral of heat[†].

Besides x_j and λ_j, the values of $(x_{j+i}^2 - x_j^2)$ and $(\lambda_{j+i} - \lambda_j)$ are obtained for the computation of $W(t)$, $Q(t)$ and $\Delta E(t)$. As shown in Fig. 17, the output data from the PD voltage agree well with the input signal used to control the particle's confinement.

The temporal evolution of the energetics during one realization of a compressing protocol is displayed in Fig. 18 (left) for a short protocol and Fig. 18 (right) for a long one. During the process, the derivative of the laser intensity, a deterministic variable, substantially contributes to the shape of the work's temporal evolution, which has a smooth curve. On the other hand, the heat and internal energy difference has irregular curves due to the contribution of the stochastic position, which is a nondeterministic variable.

Considering the initial and final states are in equilibrium, the final values of $W(\tau_P + 3\gamma/\lambda_f) = W(\tau_P)$, $Q(\tau_P + 3\gamma/\lambda_f)$, and $\Delta E(\tau_P + 3\gamma/\lambda_f)$ for each trajectory are computed for an ensemble of 10^4 trajectories of the same protocol. Since the derivative

---

[†] The use of Stratonovich calculus is convenient for stochastic trajectories when the derivative of a nondeterministic quantity, in this case x, must be computed. This approach is considered an appropriate method according to references (13, 70, 71). For a given function $g(f(t))$ integrated into $f(t)$ at time t, one has:

$$\int g(f(t)) \circ df(t) = \lim_{\Delta t \to 0} \sum g(\bar{f}(t))(f(t + \Delta t) - f(t)) \tag{4.14}$$

with $\bar{f}(t) = \frac{f(t)+f(t+\Delta t)}{2}$.

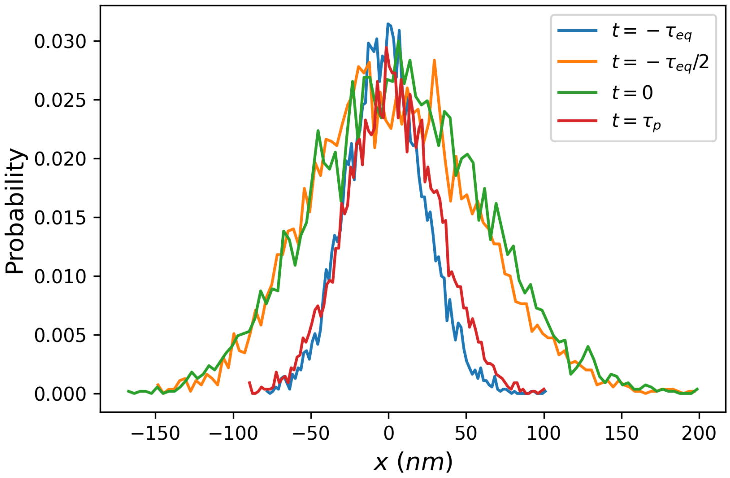

Figure 16 – Position histograms at different instants of a compressing linear protocol: $t = -\tau_{eq}$ (beginning of the equilibrium process) in blue, $t = -\tau_{eq}/2$ (middle of the equilibrium process) in orange, $t = 0$ ms (end of the equilibrium process and beginning of the protocol) in green, and $t = \tau_P$ (end of the protocol). The positions were obtained from 10^4 positions with $\tau_{eq} = 20$ ms, $\tau_P = 0.1\tau_R$, $\lambda_i = 1.5\ pN/\mu m$, $\Delta\lambda = 10\lambda_i$, where $\tau_R = \gamma/\lambda_i \approx 12$ ms is the relaxation time in the state λ_i.

Source: By the author.

of the control parameter is zero after the end of the protocol, the trajectory for $t > \tau_P$ does not contribute to the final work calculation. However, for heat and internal energy, this is not true. The particle continues exchanging energy with the bath a longer time, i.e., typically longer than the relaxation time in final state γ/λ_f is required for computing those thermodynamic quantities[‡].

The probability distributions of the energetics can be obtained from the normalized histograms of those quantities and are shown in Fig. 19 for a case completely out of equilibrium ($\tau_P = 0.1\tau_R$) and in Fig. 20 for a case closer to the equilibrium regime ($\tau_P = 2\tau_R$). For a compressing protocol, since x^2 is always positive, the work (left) signal depends only on the derivative of the trap stiffness and has positive values (the system absorbs energy). Negative and positive values are observed for heat and internal energy difference (right). Moreover, as discussed previously, the particle shows significant fluctuations of the order of k_BT in the thermodynamic quantities. However, the distributions become narrower if the same process is run more slowly, converging to equilibrium, and the work distribution should behave as a delta function in an ideal quasistatic regime, with $\tau_P \to \infty$. Another interesting point is that, although the average value of work must be bigger than the free energy difference, many individual events have a lower value.

[‡] Here, it was considered three times longer than the relaxation time in the final state for enabling particle thermalization.

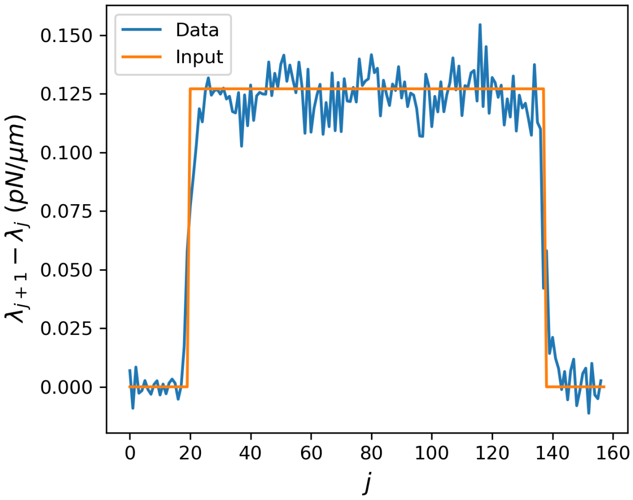

Figure 17 – Typical values for $\lambda_{j+1} - \lambda_j$ for linear protocols with $\tau_{eq} = 20$ ms, $\lambda_i = 1.5\ pN/\mu m$, $\Delta\lambda = 10\lambda_i$ and $\tau_P = 0.1\tau_R$, where $\tau_R = \gamma/\lambda_i \approx 12$ ms is the relaxation time in the state λ_i.

Source: By the author.

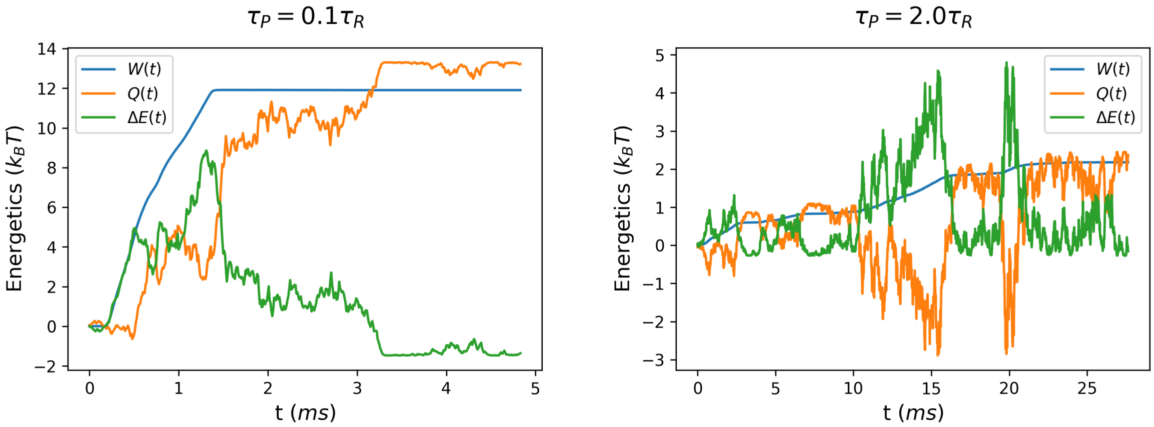

Figure 18 – Temporal evolution of work in blue, heat in orange, and internal energy difference in green during compressing linear protocols with $\tau_{eq} = 20$ ms, $\lambda_i = 1.5\ pN/\mu m$, $\Delta\lambda = 10\lambda_i$ and different protocol times: $\tau_P = 0.1\tau_R$ (left) and $\tau_P = 2\tau_R$ (right), where $\tau_R = \gamma/\lambda_i \approx 12$ ms is the relaxation time in the state λ_i.

Source: By the author.

4.3.1 Verification of the First Law of Thermodynamics

The probability distributions of the final values of work, heat, and internal energy difference enable obtaining their average values for different protocol times and modulation amplitudes. Here, the experimental results for those parameters are compared to the theoretical predictions discussed in Sec. 4.1.1[§]. As shown in Fig. 21, the agreements be-

---

[§] Note the average of a quantity Y for N samples is given by $\langle Y \rangle = \sum_{i=0}^{N} Y_i/N$. Here, it was used the uncertainty given by standard error $\delta\langle Y \rangle = \sigma_{\langle Y \rangle}/\sqrt{N}$, where $\sigma_{\langle Y \rangle}$ is the standard

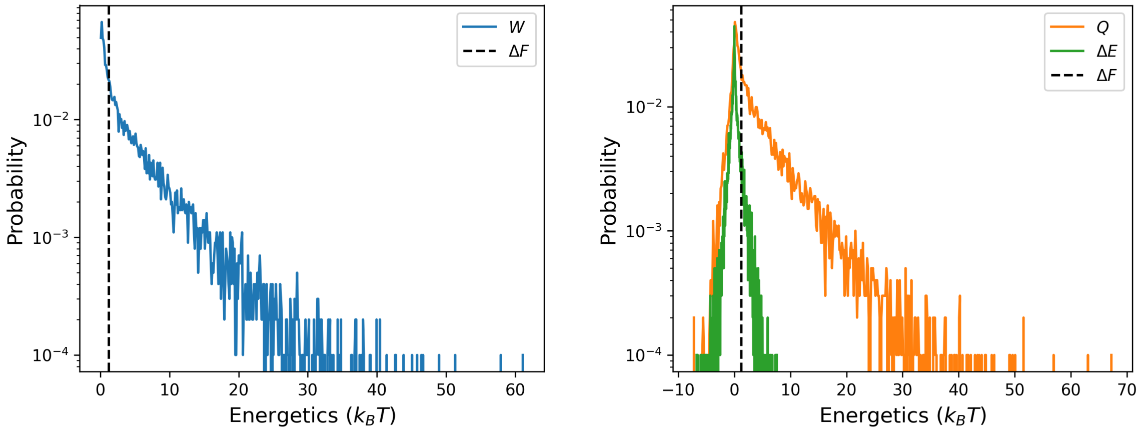

Figure 19 – Probability distribution of work (left), heat, and internal energy difference (right) for 10^4 trajectories of compressing linear protocols with $\tau_{eq} = 20$ ms, $\lambda_i = 1.5\ pN/\mu m$, $\Delta\lambda = 10\lambda_i$, and $\tau_P = 0.1\tau_R$, where $\tau_R = \gamma/\lambda_i \approx 12$ ms is the relaxation time in the state λ_i. The black dashed line represents the free energy difference.

Source: By the author.

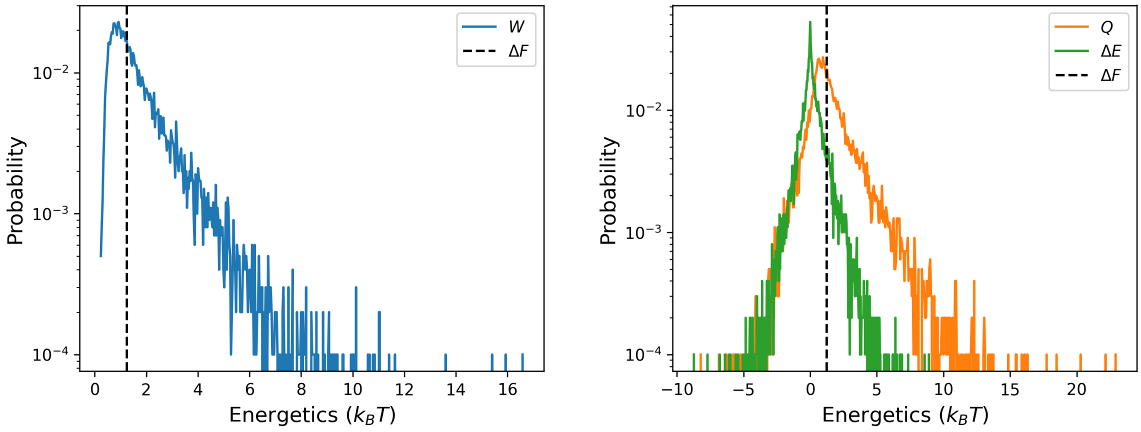

Figure 20 – Probability distribution of work (left), heat, and internal energy difference (right) for 10^4 trajectories of compressing linear protocols with $\tau_{eq} = 20$ ms, $\lambda_i = 1.5\ pN/\mu m$, $\Delta\lambda = 10\lambda_i$, and $\tau_P = 2\tau_R$, where $\tau_R = \gamma/\lambda_i \approx 12$ ms is the relaxation time in the state λ_i. The black dashed line represents the free energy difference.

Source: By the author.

tween experimental results and theoretical predictions are satisfactory for protocols with a small modulation amplitude ($\Delta\lambda = \lambda_i$) (left) and a big one ($\Delta\lambda = 10\lambda_i$) (right). Moreover, the average work decreases as the protocol time increases, converging to the free energy difference for longer protocol times, ΔF, as expected by the Clausius inequality (72) (Second Law of Thermodynamics).

Fig. 22 displays the energetics dependency on the modulation amplitude for a protocol with a fixed duration ($\tau_P = 0.145\tau_R$). Again, the experimental results are in good

---

deviation for N measurements.

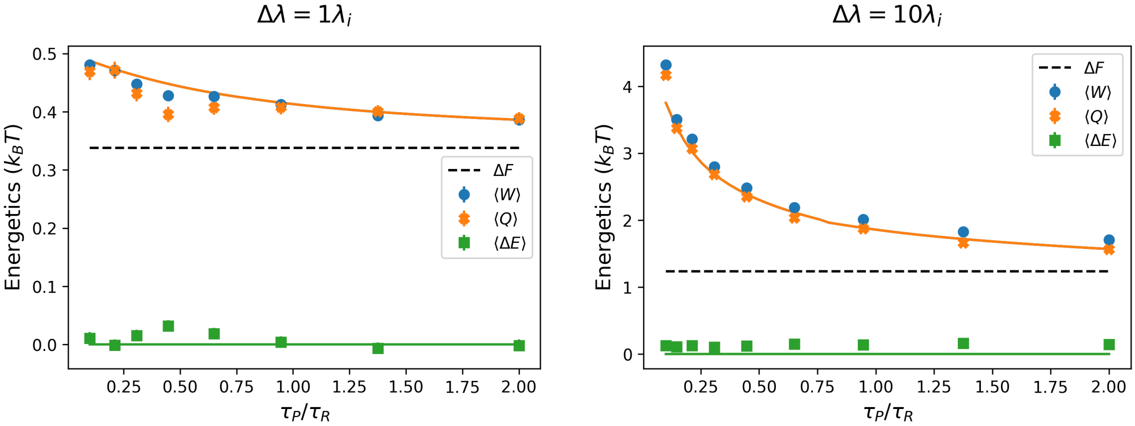

Figure 21 – Protocol time dependency of the average values of work, in blue, heat, in orange, and internal energy difference, in green, for 10^4 trajectories of compressing linear protocols with $\tau_{eq} = 20$ ms, $\lambda_i = 1.5\ pN/\mu m$ and different modulation amplitudes $\Delta\lambda = \lambda_i$ (left) and $\Delta\lambda = 10\lambda_i$ (right), where $\tau_R = \gamma/\lambda_i \approx 12$ ms is the relaxation time in the state λ_i. The black dashed line represents the free energy difference, solid lines denote theoretical predictions, and dots correspond to experimental results. Note that here, the solid curves for work and heat are the same, and the uncertainties are smaller than the dots.

Source: By the author.

agreement with the theoretical predictions. Although the mean internal energy difference remains unchanged, the mean work and heat grow as the modulation amplitude increases, as expected.

Despite the difficulty in estimating the variance of the energetics quantities¶, σ^2, Fig. 23 shows the experimental results for different parameters. Here, the variance for work and heat converges to zero when the protocols are performed more slowly, i.e., with a longer protocol time, as expected. The variance of free energy difference remains approximately constant for the explored parameters with $\sigma^2_{\Delta E} \approx (k_BT)^2$.

Then, we can compute $\langle W\rangle - \langle Q\rangle - \langle \Delta E\rangle$ dependency on the protocol time for different modulation amplitudes, as shown in Fig. 24. Since this value is close to zero for all parameters explored in this study, the First Law of Thermodynamics was also verified.

¶ The variance is given by

$$\sigma^2_Y = \frac{1}{N-1}\sum_{l=1}^{N}(Y_l - \langle Y\rangle)^2. \tag{4.15}$$

The uncertainty of variance, $\delta[\sigma^2_Y]$, is obtained computing the variance for 10 groups with 1000 trajectories each, $\{\sigma^2_Y\}_{i=1,\ldots,1000}$. The standard deviation of the results leads to the uncertainty $\delta[\sigma^2_Y] = \sigma_{\{\sigma^2_Y\}_{i=1,\ldots,1000}}/\sqrt{10}$.

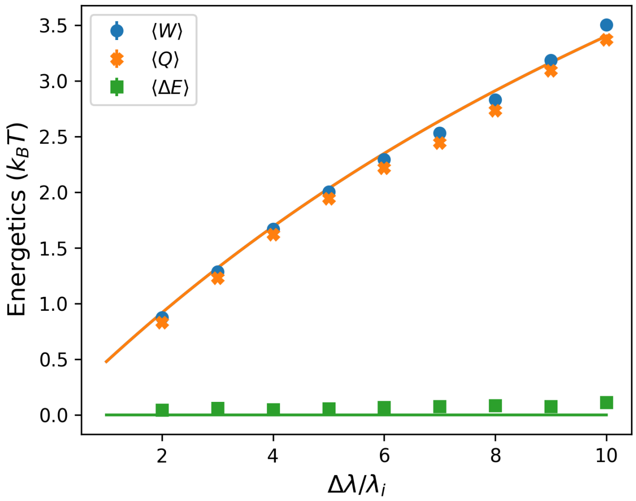

Figure 22 – Experimental (dots) and theoretical (solid lines) energetics dependency on modulation amplitude obtained from 10^4 trajectories of linear protocols with $\tau_{eq} = 20$ ms, $\lambda_i = 1.5\ pN/\mu m$ and $\tau_P = 0.145\tau_R$, where $\tau_R = \gamma/\lambda_i \approx 12$ ms is the relaxation time in the state λ_i. Average work in blue, heat in orange, and internal energy difference in green. The uncertainties are smaller than the dots.

Source: By the author.

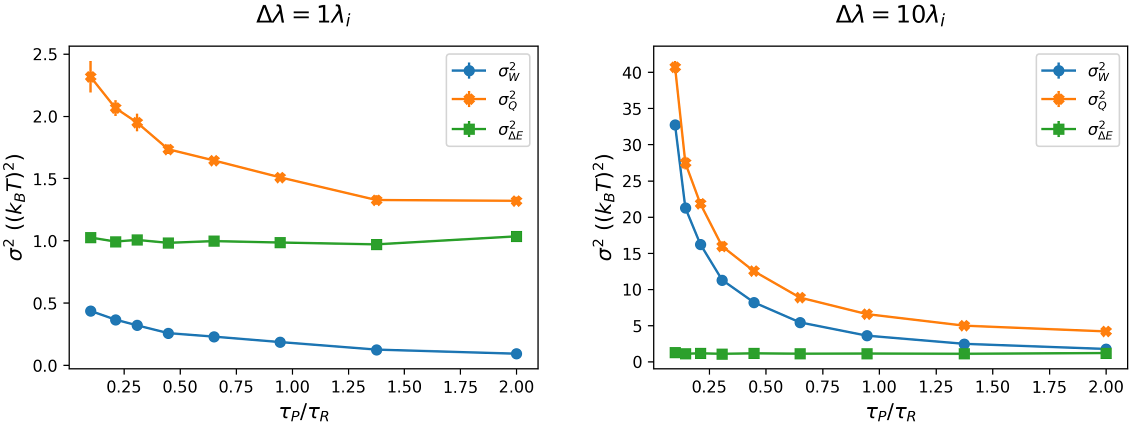

Figure 23 – Protocol time dependency of energetics variance obtained from 10^4 trajectories of linear protocols with $\tau_{eq} = 20$ ms, $\lambda_i = 1.5\ pN/\mu m$ and different modulation amplitudes $\Delta\lambda = \lambda_i$ (left) and $\Delta\lambda = 10\lambda_i$ (right), where $\tau_R = \gamma/\lambda_i \approx 12$ ms is the relaxation time in the state λ_i. Variance of work in blue, heat in orange, and internal energy difference in green. The uncertainties are smaller than the dots.

Source: By the author.

4.3.2 Verification of Jarzynski equality

As discussed in Sec. 2.2, Jarzynski equality is one of the most important results in stochastic thermodynamics due to its versatility in estimating an equilibrium quantity from nonequilibrium measurements. Therefore, it can be used experimentally as a very good estimator of the free energy difference between two equilibrium states whose theo-

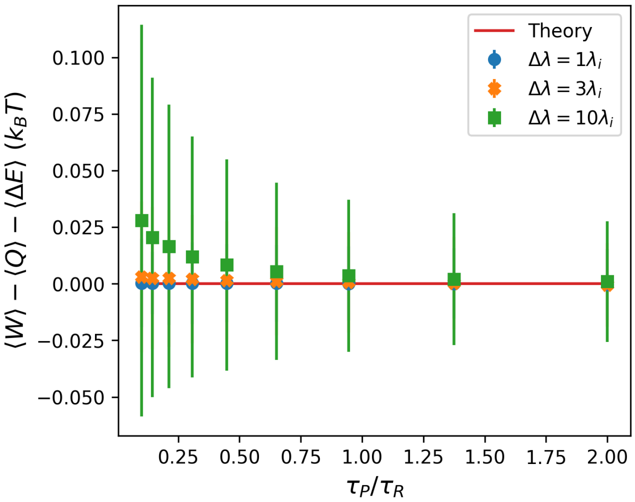

Figure 24 – Protocol time dependency of $\langle W\rangle - \langle Q\rangle - \langle \Delta E\rangle$ for 10^4 trajectories of compressing linear protocols with $\tau_{eq} = 20$ ms, $\lambda_i = 1.5\ pN/\mu m$ and different modulation amplitudes $\Delta\lambda = \lambda_i$ in blue, $3\lambda_i$ in orange, and $10\lambda_i$ in green, where $\tau_R = \gamma/\lambda_i \approx 12$ ms is the relaxation time in the state λ_i. The solid red line denotes the theoretical prediction, and the dots correspond to the experimental results.

Source: By the author.

retical computation is challenging. In our case, the analytical solution for ΔF when the confinement of the particle is changed from λ_i to λ_f is easily obtained, as shown in Eq. 4.7. Therefore, our proposal is to check the consistency of the results from the free energy difference estimation with the ones from the work distributions.

From Eq. 4.7, the left-hand term of Eq. 2.10 can be computed by

$$e^{-\Delta F/K_BT} = \frac{Z_f}{Z_i} = \sqrt{\frac{\lambda_i}{\lambda_f}}, \tag{4.16}$$

where λ_i and λ_f are obtained from the PD signal during the equilibrium time. The use of the average output value in both states leads to the estimated trap stiffness from the calibration curve shown in Fig. 13[‖].

The right-hand term of Eq. 2.10 is directly calculated from the work distributions.

[‖] The uncertainty of $e^{-\Delta F/K_BT}$ is given by

$$\delta[e^{-\Delta F/K_BT}] = \frac{1}{2\sqrt{\frac{\lambda_i}{\lambda_f}}}\sqrt{\left(\frac{1}{\lambda_f}\delta\lambda_i\right)^2 + \left(-\frac{\lambda_i}{\lambda_f^2}\delta\lambda_f\right)^2}. \tag{4.17}$$

being $\delta\lambda(t) = \sqrt{(\delta m_{TS}V_{PD}(t))^2 + (\delta V_{PD}(t)m_{TS})^2 + (\delta b_{TS})^2}$ the uncertainties of trap stiffness in initial ($\delta\lambda_i$) and final ($\delta\lambda_f$) states.

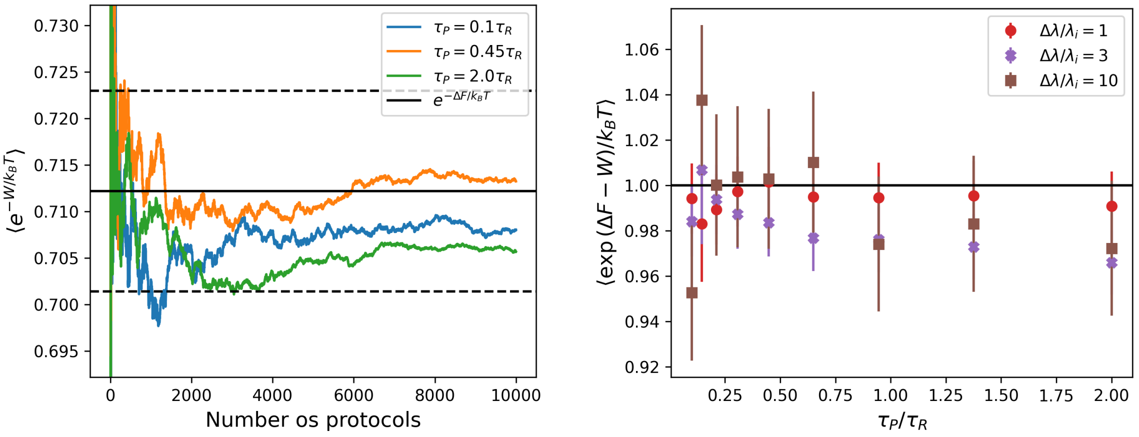

Figure 25 – On the left is the convergence of $\langle e^{-W/k_BT}\rangle$ *versus* number of experimental protocols run for $\Delta\lambda = \lambda_i$ and different protocol times, $\tau_P = 0.1\tau_R$, $0.45\tau_R$ and $2\tau_R$, in blue, orange, and green respectively. On the right are the final results of $\langle e^{\Delta F - W/k_BT}\rangle$ *versus* protocol time for different modulation amplitudes: $\Delta\lambda = \lambda_i$, $3\lambda_i$, and $10\lambda_i$ in red, purple, and brown, respectively. Results for compressing linear protocols with $\tau_{eq} = 20$ ms, and $\lambda_i = 1.5\ pN/\mu m$, where $\tau_R = \gamma/\lambda_i \approx 12$ ms is the relaxation time in the state λ_i. The black continuous line represents the expected value, and the dashed lines denote the uncertainties.

Source: By the author.

For N trajectories, where $l = 0, 1, 2...N$, one has[**]:

$$\langle e^{-W/k_BT}\rangle = \frac{1}{N}\sum_{l=0}^{N} e^{-W_l/k_BT}. \tag{4.18}$$

Fig. 25 (left) shows the results of the computation of $\langle e^{-W/k_BT}\rangle$ for different numbers of trajectories. It is notable that 10^4 repetitions are enough for the convergence of the results obtained from the work distributions to the value of $e^{-\Delta F/k_BT}$.

The final results are displayed in Fig. 25 (right), which shows a comparison of both sides of Eq. 2.10. A good agreement is reached for protocols with a small modulation amplitude ($\Delta\lambda = \lambda_i$); however, some deviation starts to appear for bigger changes in the bead's confinement ($\Delta\lambda = 3\lambda_i$ and $\delta\lambda = 10\lambda_i$), especially for slower protocols.

A possible explanation for such results is related to the amplification factor calibration displayed in Fig. 13. Since the protocol starts in a given laser power corresponding to the initial state, the particle starts with the value of the amplification factor corresponding to the PD average signal during the equilibrium position. However, when the intensity of the beam is significantly changed (for $\Delta\lambda = 3\lambda_i$ and $10\lambda_i$ cases) and the particle has enough time to move in z (on protocols with bigger τ_P), the calibration is not accurate

---

[**] For the obtaining of the uncertainty of $\delta[\exp(-W/k_BT)]$, the value of $\{\exp(-W/k_BT)\}_{i=1,\dots,1000}$ is computed for 10 groups with 1000 trajectories each. The standard deviation of these results provides $\delta[\exp(-W/k_BT)] = \sigma_{\{\exp(-W/k_BT)\}_{i=1,\dots,1000}}/\sqrt{10}$.

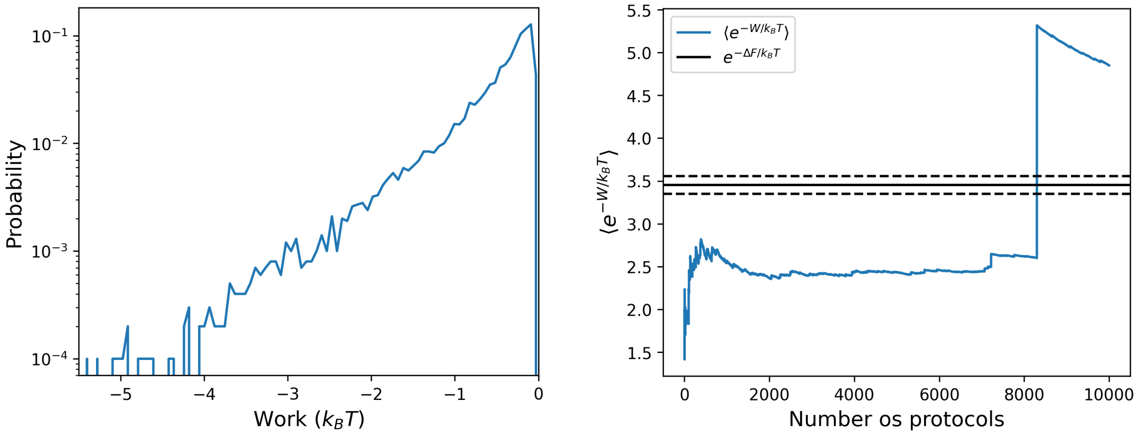

Figure 26 – Probability distribution of work (left) and results from the testing of Jarzynski's equality (right) for 10^4 trajectories of an expanding linear protocol. Here, we see the convergence of $\langle e^{-W/k_BT}\rangle$ *versus* number of protocols run for $\Delta\lambda = 10\lambda_i$, $\tau_P = 0.1\tau_R$, $\tau_{eq} = 20$ ms, and $\lambda_i = 1.5\ pN/\mu m$, where $\tau_R = \gamma/\lambda_i \approx 12$ ms is the relaxation time in the state λ_i. The black continuous line represents the expected value of $\langle e^{-\Delta F/k_BT}\rangle$ and the dashed lines denote the uncertainties.

Source: By the author.

and the position is overestimated. For an overestimation of x, the work is bigger than expected and $\langle e^{\Delta F - W/k_BT}\rangle$ becomes smaller than one.

Regarding expanding protocols, in which the particle changes its state from λ_f to λ_i ($\lambda_f > \lambda_i$), the verification of Jarzynski equality is more difficult, as discussed in (69). Since the work values become negative for this case ($d\lambda/dt < 0$ and $\langle x\rangle^2 > 0$), the rare events - corresponding to the tail of the probability distributions shown in Fig. 26 (left) - have a significant contribution in the computation of the term $\langle e^{-W/k_BT}\rangle$ and a bigger number of protocols is required for accurate results. Fig. 26 (right) shows the convergence of the exponential term for the same data set. In this case, small problems emerging during experiments (e.g., a door opening in the room, temperature drift, among others) can completely change the average of the exponential term values that are sensitive to rare events. Therefore, our proposal is to investigate the expanding protocol using the Crooks relation.

4.3.3 Verification of Crooks relation

Crooks proposed an even more general relation between the probabilities to obtain a given value of work for a forward protocol and a reverse one, as discussed in Sec. 2.2. The relation is given by (Eq. 2.13):

$$\frac{P_F(W)}{P_R(-W)} = e^{(W-\Delta F)/k_BT}, \tag{4.19}$$

where $P_F(W)$ is the probability distribution of W in the forward process (compressing) and $P_R(-W)$ is the probability distribution of $-W$ in the reverse case (expanding)[††].

As shown in Fig. 27, the forward processes always have positive values of work, since the derivative of the control parameter is always positive, i.e. $d\lambda/dt > 0$, and the reverse is always negative, since $d\lambda/dt < 0$. As expected, the work value of the crossing point W_C, $P_F(W_C) - P_R(-W_C) = 0$, is equal to the free energy difference. Such an intersection occurs in a region still with a high number of events around W_C; thus, Crooks's theorem prediction can be verified with the proposed number of trajectories.

Taking the *log* of Eq. 2.13:

$$\ln\left[\frac{P_F(W)}{P_R(-W)}\right] = (W - \Delta F)/k_BT, \tag{4.20}$$

enables the exploration of the relation validity, as depicted in Fig. 28. The points are distributed around the expected linear function $W - \Delta F = 0$, especially at the beginning of the curve, which is the region with more statistics. However, they start to spread in the region with bigger work values, corresponding to the distributions' tail (rare events). As in Jarzysnki verification, the results are more accurate for small modulation amplitudes and protocol times. The explanation is the same provided in Sec. 4.3.2.

4.4 Conclusions

This chapter addressed the implementation of a compressing and expansion protocol via modulation of the trapping beam intensity. Firstly, it described the calibrations necessary for the preparation of the experiment and the way of controlling the optical potential during the application of the protocol. The positions obtained with QPD and the force constant estimated from the infrared PD monitoring signal enabled the experimental calculation of work, heat, and internal energy difference for each trajectory.

The probability distributions of those stochastic quantities were calculated for an ensemble of 10^4 experimental trajectories. As demonstrated, for short protocol times, the work fluctuations become more pronounced, resulting in higher variance and mean value, which converges to the free energy difference in slower protocols. Also, for long protocols, the probability curves become narrower and a delta function centred at $\langle W\rangle = \Delta F$ is expected in the quasistatic limit case.

In addition, a good agreement was observed between theoretical and experimental values of $\langle W\rangle$, $\langle Q\rangle$, and $\langle \Delta E\rangle$. The First Law of Thermodynamics, as well as Fluctuation Theorems - Jarzynski's equality and Crooks' relation - were verified experimentally for the explored set of parameters.

[††] Here, $P_F(W)$ is obtained from the histrogram of W in forward protocols and $P_R(-W)$ is obtained from the histrogram of $-W$ in reverse ones.

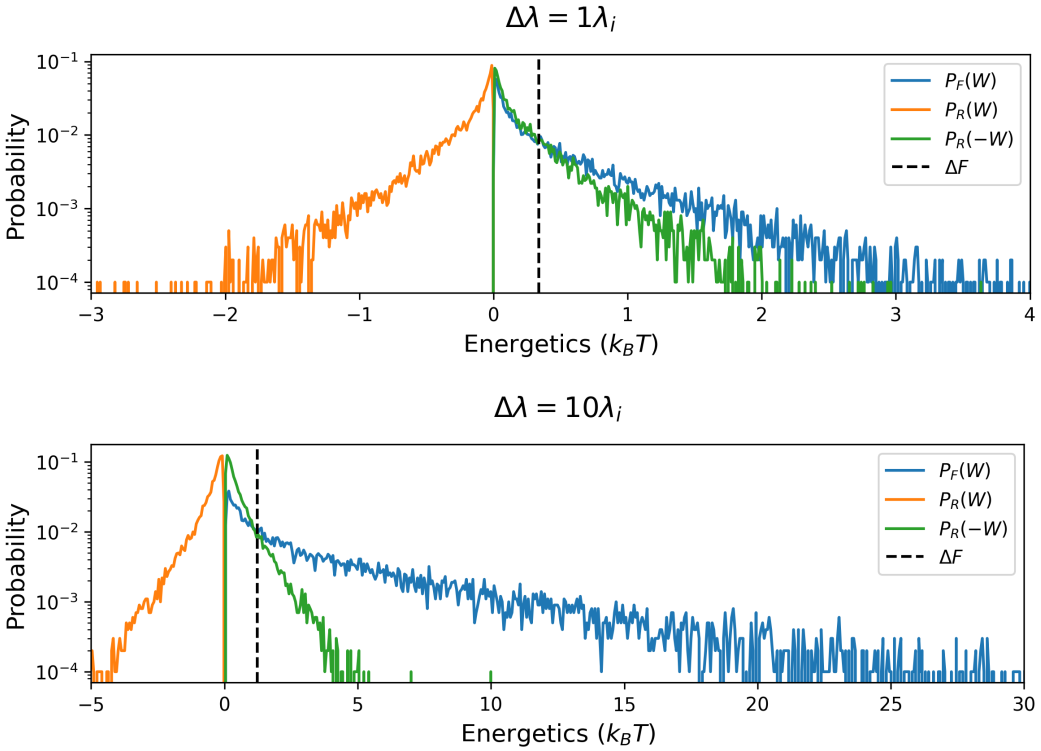

Figure 27 – Probability distributions of work $P_F(W)$ in blue, $P_R(W)$ in orange, and $P_R(-W)$ in green for different modulation amplitudes: $\Delta\lambda = \lambda_i$ (top) and $\Delta\lambda = 10\lambda_i$ (bottom). Results from 10^4 trajectories with $\tau_{eq} = 20$ ms, $\lambda_i = 1.5\ pN/\mu m$, and $\tau_P = 0.1\tau_R$, where $\tau_R = \gamma/\lambda_i \approx 12$ ms is the relaxation time in the state λ_i. The free energy difference is represented by the black dashed line.

Source: By the author.

Concerning Fluctuation Theorems, the experimental results are close to expected values with minor deviations for protocols with higher modulation amplitudes and longer protocol times. As discussed previously, such results possibly stemmed from changes in the amplification factor when the trapping beam power was modulated. Ideally, this calibration factor should have an approximately constant value; however, in our experiment, it has an approximate linear dependence on V_{PD} in the explored region.

In future work, the experiment can be repeated in a different setup, which might include a detection laser counter-propagating to the trapping laser. The beam waist in z would possibly be larger, increasing the stable zone of z around the focal position of the detection beam so that the QPD response will be less sensitive to changes in the vertical position of the particle.

The experiments proposed in this chapter were also explored in (70) and are necessary to ensure confidence in experimental data and develop more complex and new studies.

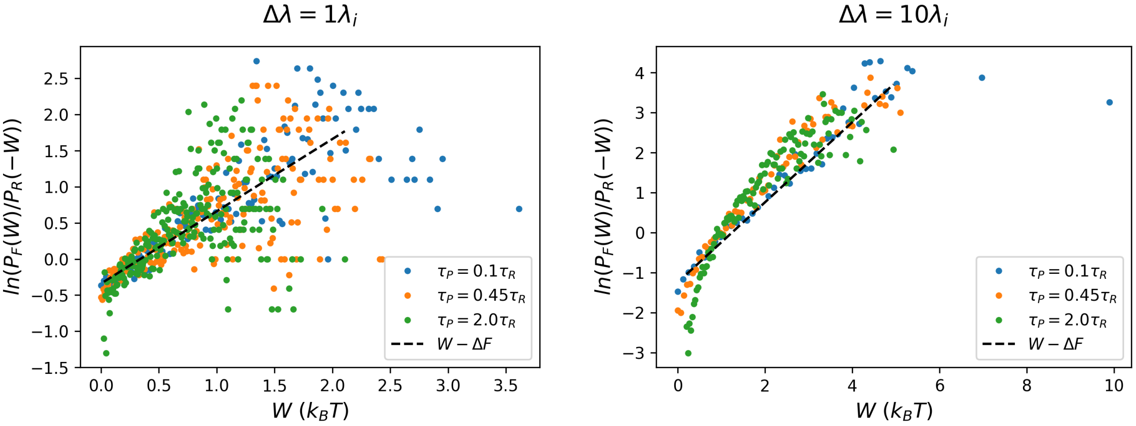

Figure 28 – Verification of Crooks theorem for different modulation amplitudes: $\Delta\lambda = \lambda_i$ (left) and $\Delta\lambda = 10\lambda_i$ (right). The results were calculated by Eq. 4.20 from 10^4 trajectories with $\tau_{eq} = 20$ ms, $\lambda_i = 1.5\ pN/\mu m$, and different protocol times: $\tau_P = 0.1\tau_R$ in blue, $0.45\tau_R$ in orange, and $2\tau_R$ in green, where $\tau_R = \gamma/\lambda_i \approx 12$ ms is the relaxation time in the state λ_i.

Source: By the author.

5 OPTIMAL PROCESSES

Fundamentally, the energy cost for performing work in a process depends on the particle's trajectory in the phase space. If the protocol time increases to larger time scales, the work value converges to Helmholtz's free energy difference, which is the minimal cost (or maximum payout) in a reversible (infinitely slow) process. However, in targeting finite-time protocols running out of thermodynamic equilibrium, the process that minimizes the average work is called optimal protocol (73–74). Efforts to find optimized tasks for different platforms may contribute to the understanding of the performance of different biological systems and provide insights into the development of more efficient devices in that regime.

Therefore, several studies have aimed to model such optimal protocols in different platforms over the past few years. Among them, some analytical results (74–76) and approximations for slowly varying processes and weak processes (77–80) have been discussed. In this scenario, this chapter is devoted to experimental tests of the analytical formulas proposed by Schmiedl and Seifert (74) for a Brownian particle trapped in a harmonic potential. Despite this work being extremely important in the context of process optimization, to the best of our knowledge, no direct experimental verification of their predictions has been conducted.

First, solutions for the optimal curves are presented in two cases, of which the first considers a moving potential and the second involves a compressing trap. Since the first case is more experimentally challenging, simulations of the stochastic trajectories were performed and are discussed. Afterwards, one will focus on the experimental verification of the second case using the Setup ENS-Lyon. For both conditions, the optimal curve results were compared with linear (suboptimal) ones and the Jarzynski equality was verified as a consistency check. Finally, the conclusions and next steps are presented.

5.1 Prediction for finite-time protocols

The model proposed in (74) considers a colloidal particle in the overdamped regime that goes from one equilibrium state to another. If the particle is trapped in a harmonic potential, $U(x)$, subject to control parameter $\lambda(t)$ for a time duration τ_P, the work is given by Eq. 2.7 and its average value is

$$\langle W[\lambda(t)]\rangle = \int_0^{\tau_P} dt\dot{\lambda}\langle\frac{\partial U(x,\lambda)}{\partial\lambda}\rangle. \tag{5.1}$$

Therefore, the protocol $\lambda^*(t)$ that minimizes $\langle W[\lambda(t)]\rangle$ for a target finite-time is the optimal one and will be implemented in the experimental system. Below is the solution of the minimization of Eq. 5.1 for the moving laser trap and the time-dependent trap stiffness protocols. A complete description can be found in (74).

5.1.1 Moving laser trap

This first case focuses on a harmonic potential with a fixed trap stiffness κ and variable equilibrium position, from $\lambda_i = 0$ to λ_f. The potential is given by

$$U(x,t) = \frac{\kappa(x-\lambda(t))^2}{2}, \tag{5.2}$$

and the average work is obtained by

$$\langle W\rangle = \int_0^{\tau_P} dt\kappa\dot{\lambda}(\lambda - u), \tag{5.3}$$

where $u(t) \equiv \langle x(t)\rangle$. Langevin equation (Eq. 2.17) leads to

$$\dot{u} = \frac{\kappa}{\gamma}(\lambda - u) \tag{5.4}$$

and consequently,

$$\langle W\rangle = \int_0^{\tau_P} dt\left(\frac{\gamma^2}{\kappa}\ddot{u} + \gamma\dot{u}\right)\dot{u} = \frac{\gamma^2}{2\kappa}\dot{u}^2|_o^{\tau_P} + \gamma\int_0^{\tau_P} dt\dot{u}^2. \tag{5.5}$$

The minimization of Eq. 5.3 by Euler-Lagrange equation (81) results in $\ddot{u} = 0$. Therefore, $u(t) = mt$, where m is a scalar, since $u(0) = 0$. The boundary conditions for Eq. 5.4 lead to $\dot{u}(0) = \frac{\kappa}{\gamma}(\lambda_i - u(0)) = 0$ and $\dot{u}(\tau_P) = \frac{\kappa}{\gamma}(\lambda_f - m\tau_P)$. Substituting those results in Eq. 5.5, one has

$$\langle W\rangle = \gamma m^2\tau_P + \frac{\kappa}{2}(\lambda_f - m\tau_P)^2. \tag{5.6}$$

The value of m that minimizes the previous equation is

$$m^* = \frac{\lambda_f}{2\frac{\gamma}{\kappa} + \tau_P}, \tag{5.7}$$

and the corresponding work is

$$\langle W^*\rangle = \frac{\lambda_f^2\gamma}{2\frac{\gamma}{\kappa} + \tau_P}. \tag{5.8}$$

Finally, the optimal protocol, obtained from Eq. 5.4, is given by

$$\lambda^*(t) = \frac{\lambda_f}{2\frac{\gamma}{\kappa} + \tau_P}\left(t + \frac{\gamma}{\kappa}\right). \tag{5.9}$$

Fig. 29 show the resulting protocols with two symmetrical jumps at the beginning and the end of the protocol*:

$$\Delta\lambda \equiv \lambda(0)^+ - \lambda_i = \lambda_f - \lambda(\tau_P)^- = \frac{\lambda_f}{2 + \tau_P\frac{\kappa}{\gamma}}. \tag{5.10}$$

The optimal curve converges to the linear protocol behavior for long processes, where $\tau_P \to \infty$.

---

[*] Remember the protocol starts in $\lambda_i = 0$ and ends in λ_f, i.e., there are two discontinuities to link both initial and final states to the protocol curve.

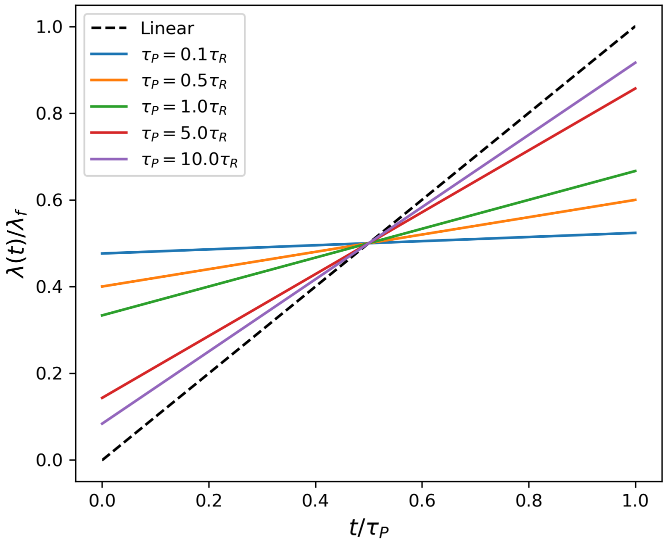

Figure 29 – Optimal protocols for the moving laser trap case obtained for $\lambda_f = 500$ nm and different protocol times. The black dashed line represents the linear protocol. Trap stiffness $\kappa = 1$ pN/μm was used for all curves.
Source: By the author.

5.1.2 Time-dependent trap stiffness

In the second case, the equilibrium position remains fixed, and the confinement of the particle is dependent on time. The potential can be written as

$$U(x,t) = \frac{\lambda(t)x^2}{2} \tag{5.11}$$

and the average work is given by

$$\langle W\rangle = \frac{1}{2}\int_0^{\tau_P} dt\dot{\lambda}\langle x^2\rangle, \tag{5.12}$$

which, integrating by parts, leads to

$$\langle W\rangle = \frac{1}{2}\left(\lambda(t)\langle x^2\rangle|_0^{\tau_P} - \int_0^{\tau_P} dt\lambda(t)\dot{\langle x^2\rangle}\right). \tag{5.13}$$

The $\langle x^2\rangle$ value is obtained from the Fokker-Plank equation (Eq. 2.22), such as $\langle x^2\rangle = \int_{-\infty}^{+\infty} dxP(x,t)x^2$. Considering $\int_{-\infty}^{+\infty} dxP(x,t) = 1$, then

$$\dot{w} = \frac{2}{\gamma}\left[-\lambda w + k_BT\right], \tag{5.14}$$

where $w = \langle x^2\rangle$. Solving it for λ and substituting it in Eq. 5.13 result in

$$\langle W\rangle = \frac{1}{2}\left(w(t)\lambda(t) - k_BT\log w(t)\right)|_0^{\tau_P} + \frac{\gamma}{4}\int_0^{\tau_P} dt\frac{1}{w}\dot{w}^2. \tag{5.15}$$

The minimization of the integral requires resorting to Euler-Lagrange equation for

$$\dot{w}^2 - 2w\ddot{w} = 0, \tag{5.16}$$

where the solution depends on constants c_1 and c_2 and is given by

$$w(t) = c_1(1 + c_2 t)^2. \tag{5.17}$$

Since the particle is in thermal equilibrium in state λ_i, its variance in the initial instant is $w(0) = k_B T/\lambda_i$ and is equivalent to constant c_1. Minimizing the total mean work leads to

$$\frac{\langle W^* \rangle}{k_B T} = \frac{\lambda_f}{2\lambda_i}(1 + \tau_P c_2^*)^2 + \frac{(\tau_P c_2^*)^2 \gamma}{\lambda_i \tau_P} - \frac{1}{2} - \ln(1 + c_2^* \tau_P), \tag{5.18}$$

leading constant c_2

$$c_2^* \tau_P = \frac{-\gamma - \lambda_f \tau_P + \sqrt{\gamma^2 + 2\lambda_i \tau_P \gamma + \lambda_f \lambda_i \tau_P^2}}{2\gamma + \lambda_f \tau_P}. \tag{5.19}$$

Therefore, Eq. 5.14 provides the protocol that minimizes the average work:

$$\lambda^*(t) = \frac{\lambda_i - c_2^* \gamma (1 + c_2^* t)}{(1 + c_2^* t)^2}. \tag{5.20}$$

As shown in Fig. 30, the protocol also implies discontinuities at the beginning and the end of the protocol.

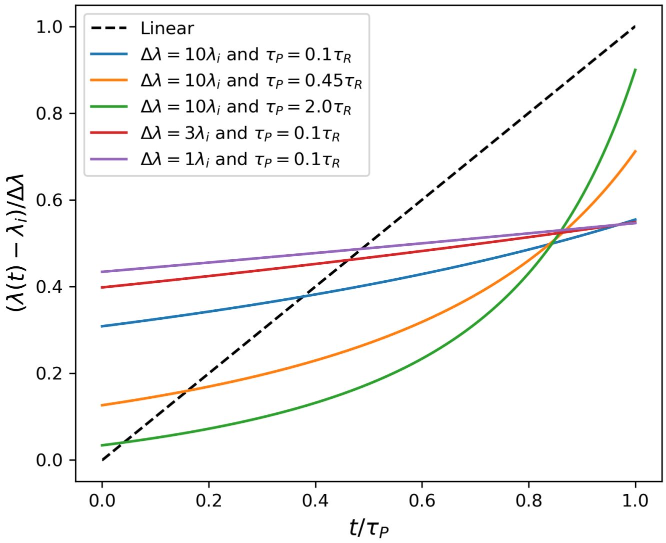

Figure 30 – Optimal protocols for the time-dependent trap stiffness case obtained for different parameters. Here, $\Delta\lambda = (\lambda_f - \lambda_i)$ with $\lambda_i = 1.5$ pN/μm. The black dashed line represents the linear protocol.

Source: By the author.

Considering the case of a process performed in a very short time, i.e. $\tau_P \to 0$, then $c_2 \tau_P \to 0$ and the average work, from Eq. 5.18, converges to

$$\lim_{\tau_P \to 0} \langle W^* \rangle = \frac{1}{2}\left(\frac{\lambda_f}{\lambda_i} - 1\right) k_B T, \tag{5.21}$$

which is the expected result for a step protocol discussed in Chapter 6.

For the opposite case, in the quasi-static limit, $\tau_P \to \infty$, hence, $c_2\tau_P \to \left(\sqrt{\lambda_f/\lambda_i} - 1\right)$ and

$$\lim_{\tau_P \to \infty} \langle W^* \rangle = \frac{1}{2} \ln \left(\frac{\lambda_f}{\lambda_i} \right) k_B T = \Delta F, \tag{5.22}$$

as expected.

5.2 Simulations for the moving potential

From an experimental point of view, the optimization of the moving trap case can be challenging, since the modulation devices (AOM/AODs) lose efficiency when the angular position is changed, i.e., when the frequency of the RF signal differs from the optimal one. Besides the loss of efficiency, keeping the same optical potential on the trap during the experiment is difficult due to the limited size of the objective entrance (the beam begins to exit the objective lens at higher beam's angular positions). Moreover, precise tracking of the bead with QPD is limited to the region of linearity around the central position (approximately the particle radius), and bigger displacements make it more complex since the QPD's response becomes non-linear. Therefore, this section explores the moving potential using adapted simulations from references (63, 82).

Since the time scale of our problem is considerably bigger than the bead's inertial time - associated with the collisions of the colloid with the molecules of the surroundings - the inertial term of the Langevin equation can be dropped (Eq. 2.17). For harmonic potentials with fixed trap stiffness, κ, and modulated equilibrium position, $\lambda = x_{eq}$, the one-dimensional dynamics is given by

$$0 = -\gamma \frac{dx(t)}{dt} - \kappa(x(t) - \lambda(t)) + \sqrt{2k_B T \gamma}\,\Xi(t). \tag{5.23}$$

Discretizing Eq. 5.23 leads to

$$0 = -\gamma \frac{x_{j+1} - x_j}{\Delta t} - \kappa(x_j - \lambda_j) + \sqrt{2k_B T \gamma}\,\Xi_j, \tag{5.24}$$

where x_j is the bead's position at instant $t = j\Delta t$, with Δt the interval between points, and $\Xi_j = \xi_j/\sqrt{\Delta t}$. ξ_j is a sequence of random numbers in a standard normal distribution, thus satisfying the physical properties for stochastic terms: $\langle \Xi(t) \rangle = 0$, and uncorrelated $\Xi(t_1)$, i.e. $\langle \Xi(t)\Xi(t') \rangle = \delta(t - t')$.

Therefore, the position of the particle for a discrete protocol is

$$x_{j+1} = x_j - \frac{\kappa(x_j - \lambda_j)\Delta t}{\gamma} + \sqrt{\frac{2k_B T \Delta t}{\gamma}}\,\xi_j. \tag{5.25}$$

Note that λ_j is given by Eq. 5.9:

$$\lambda_j = \frac{\lambda_f}{2\frac{\gamma}{\kappa} + \tau_P} \left((j\Delta t) + \frac{\gamma}{\kappa} \right), \tag{5.26}$$

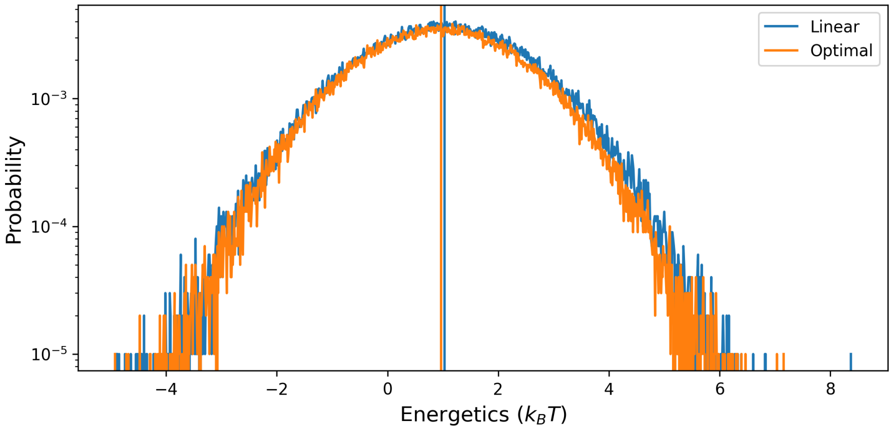

Figure 31 – Simulated probability distribution of work from 10^5 trajectories. Results for linear protocols, in blue, and optimal ones, in orange, where $T = 300$ K, $\Delta t = 10^{-5}$ s, $\lambda_f = 100$ nm, $\kappa = 1$ pN/μm, $\tau_P = 0.5\tau_R$, and $\gamma = 6\pi\eta R$, being $\eta = 0.001$ Nsm^{-2} and $R = 1$ μm.

Source: By the author.

for optimal protocols and $\lambda_j = \lambda_f(j\Delta t)/\tau_P$ for linear ones with duration τ_P. For both cases, it starts in position 0 and ends in position λ_f. Since the simulated bead must be in equilibrium at the beginning of the protocol, the initial position, x_0, is obtained from the equipartition theorem, i.e. from a random number with 0 mean and $\sqrt{k_BT/\kappa}$ standard deviation.

Simulating the trajectory enables computing the work of each cycle with duration $\tau_P = N\Delta t$. The discretization of Eq. 2.7 for $U = \kappa(x-\lambda)^2/2$ lead to

$$W_{N,prot} = -\Delta t \sum_{j=0}^{N-1} \kappa(x_j - \lambda_j)\frac{\lambda_{j+1} - \lambda_j}{\Delta t} = -\sum_{j=0}^{N-1} \kappa(x_j - \lambda_j)(\lambda_{j+1} - \lambda_j). \tag{5.27}$$

For linear protocols, $W_L = W_{N,prot}$, and for optimal ones, $W_O = W_{jump_1} + W_{N,prot} + W_{jump_2}$. Here, the contributions of the jumps are

$$W_{jump} = \frac{\kappa(x_+ - \lambda_+)^2}{2} - \frac{\kappa(x_- - \lambda_-)^2}{2}. \tag{5.28}$$

where the subindex "$-$" represents the point just before the jump and "$+$" the point just after it. This means that, for the first jump one has $\lambda_- = \lambda_i$ and $\lambda_+ = \lambda(0)$ and for the second one $\lambda_- = \lambda(\tau_P)$ and $\lambda_+ = \lambda_f$.

Fig. 31 shows the probability distribution of work obtained from linear and optimal protocols with $\lambda_f = 100$ nm for an ensemble of 10^5 trajectories. The distribution is approximately Gaussian, and the average value of work is smaller in the optimal protocol than in the linear one, as expected. Fig. 32 displays a comparison between average work results for both cases at different final positions, λ_f (left), and protocol times, τ_P (right).

For all simulated trajectories, the results show the average work value of optimal protocols is smaller than that of the linear case. However, a bigger difference between

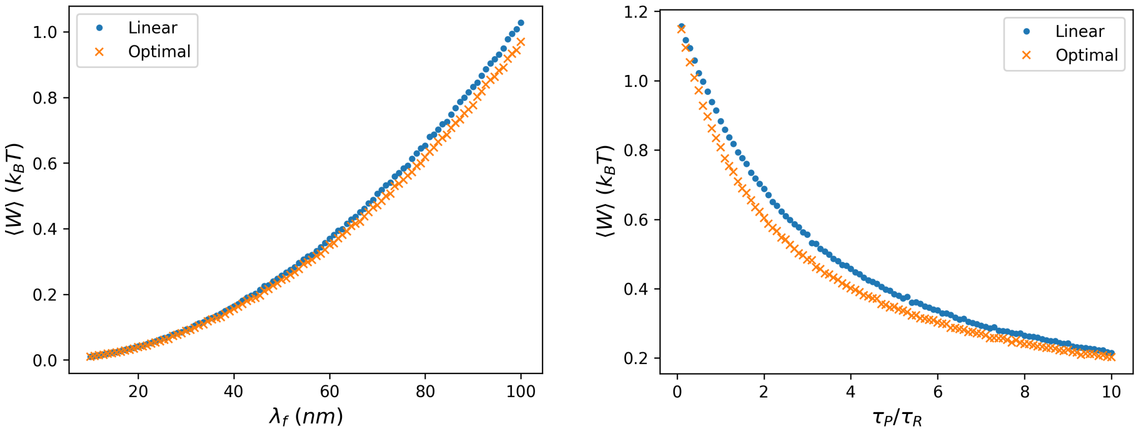

Figure 32 – Comparison of the simulated average work for linear protocols, in blue, and optimal ones, in orange. The results refer to fixed $\tau_P = 0.5\tau_R$ and different values of λ_f (left) and fixed $\lambda_f = 100$ nm and different protocol times τ_P (right). Here, 10^5 trajectories were simulated with the following parameters: $T = 300$ K, $\Delta t = 10^{-5}$ s, $\kappa = 1$ pN/μm, and $\gamma = 6\pi\eta R$, being $\eta = 0.001$ Nsm^{-2} and $R = 1$ μm.

Source: By the author.

optimal and linear (suboptimal) protocols is expected for intermediated protocol times. For quasistatic processes, where $\tau_P \to \infty$, the optimal protocol converges to the linear case, and the difference between linear and optimal results decreases again, i.e., their average work is basically the same.

As shown in Fig. 33, Jarzynski was also verified as a check. Since the partition function of a potential $U = \kappa(x-\lambda)^2/2$ is given by

$$\begin{aligned} Z &= \int_{-\infty}^{+\infty} dx e^{-U/k_BT} \\ &= \int_{-\infty}^{+\infty} dx e^{-(\kappa(x-\lambda)^2/2)/k_BT} \\ &= \sqrt{\frac{\pi}{\kappa/2k_BT}}, \end{aligned} \tag{5.29}$$

the free energy difference is $\Delta F = 0$ and Jarzynski term obtained from ΔF is $e^{-\Delta F/k_BT} = 1$.

The results show the best agreement between the terms of Jarzynski equality for smaller values of λ_f, even for a large number of simulated trajectories (10^5). Since negative work values can be obtained, rare events contribute to $\langle e^{-W/k_BT}\rangle$. The behavior of $\langle e^{-W/k_BT}\rangle$ for a fixed λ_f and different protocol times shows a better agreement in slower protocols.

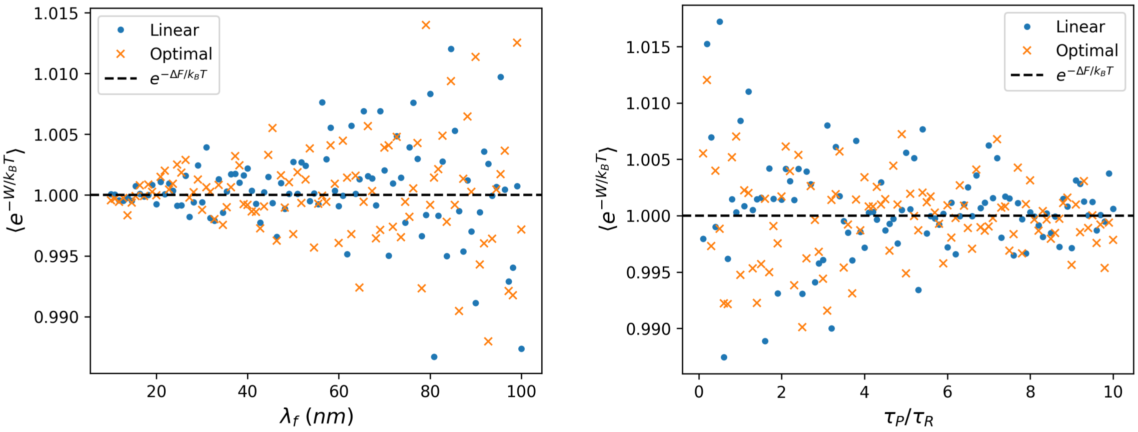

Figure 33 – Jarzynski test. Comparison of simulated $\langle e^{-W/k_BT}\rangle$ for linear protocols, in blue, and optimal ones, in orange. Results refer to fixed $\tau_P = 0.5\tau_R$ and different values of λ_f (left) and fixed $\lambda_f = 100$ nm and different protocol times τ_P (right). Here, 10^5 trajectories were simulated with the following parameters: $T = 300$ K, $\Delta t = 10^{-5}$ s, $\kappa = 1$ pN/μm, and $\gamma = 6\pi\eta R$, being $\eta = 0.001$ Nsm^{-2} and $R = 1$ μm. The black dashed line represents $e^{-\Delta F/k_BT} = 1$.

Source: By the author.

5.3 Experimental results for the compressing protocol

This section presents an experimental study of optimal protocols for the compressing trap, as described in Sec. 4.2. Similarly to the linear protocol case, the particle must be in thermal equilibrium at the beginning of the protocol in the state λ_i. After the thermalization period, the protocol is applied and the loop finishes with the trap stiffness equal to λ_f. While the linear protocol takes the particle from state λ_i to state λ_f linearly over time, the optimal protocol follows Eq. 5.20.

As described in the previous chapter, the external modulation of the function generator (Tektronix AFG3102) is used to control the RF signal that feeds the AOD. However, due to the band response limitation, a discontinuity in the amplitude of the RF signal has an around 100 μs time delay, as displayed in Fig. 34 (left). Consequently, the derivative of the control parameter, $\lambda_{j+1} - \lambda_j$, used to compute work is not similar to a delta function, as the predicted optimal ones, but has an exponential decay, as shown in Fig. 34 (right).

Similarly to linear protocols, Eq. 4.11 can be used to obtain the work values of each trajectory. Fig. 35 shows the results from a set of 10 trajectories with the same parameters. Here, the same modulation amplitude but different protocol times were applied: $\tau_P = 0.1\tau_R$ (left) and $\tau_P = 2\tau_R$ (right).

Similarly to Eq. 5.28, the work´s contributions of each jump are

$$W_{jump} = \frac{\lambda_+ x_+^2}{2} - \frac{\lambda_- x_-^2}{2}, \tag{5.30}$$

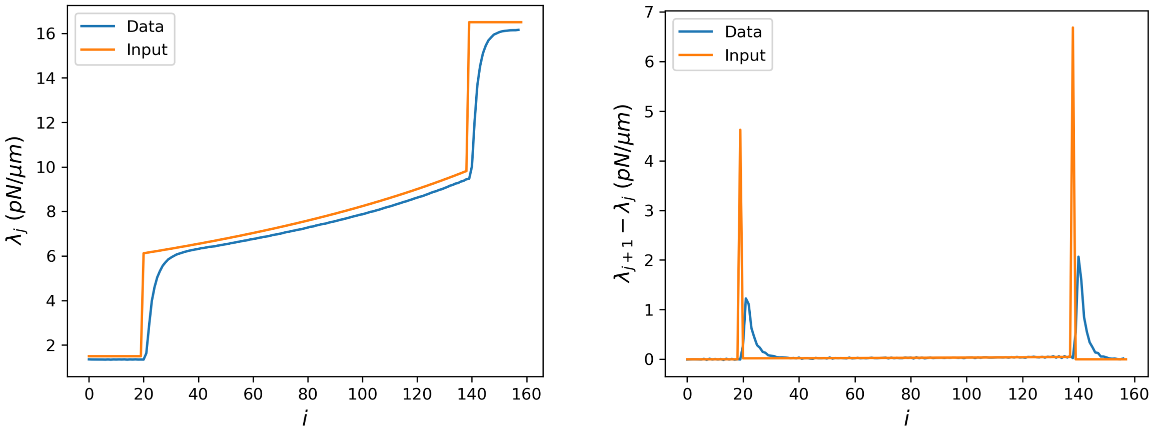

Figure 34 – Estimated trap stiffness (left), λ_j, and its derivative (right), $\lambda_{j+1} - \lambda_j$, (data from PD and input signal) for linear protocols with $\tau_{eq} = 20$ ms, $\lambda_i = 1.5\ pN/\mu m$, $\Delta\lambda = 10\lambda_i$ and $\tau_P = 0.1\tau_R$ for a single loop, where $\tau_R = \gamma/\lambda_i \approx 12$ ms is the relaxation time in the state λ_i.

Source: By the author.

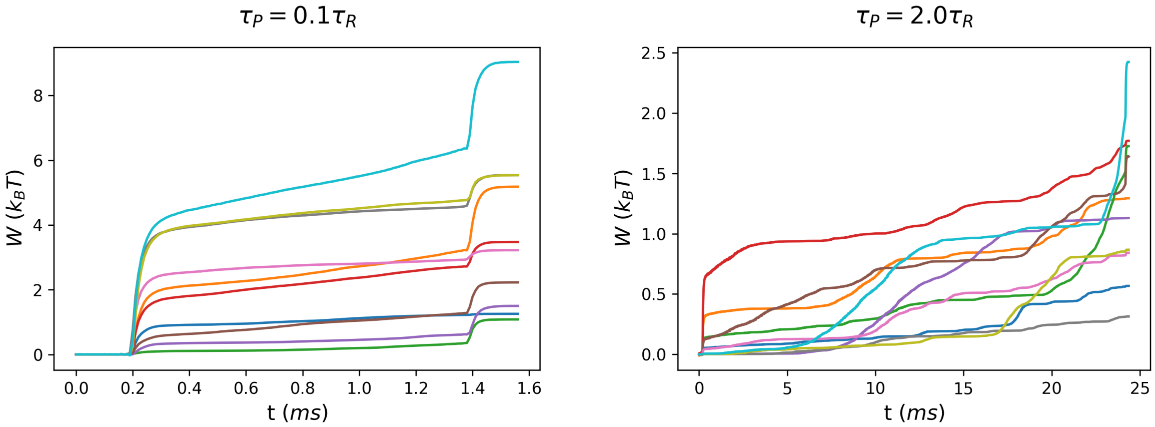

Figure 35 – Temporal evolution of work for 10 trajectories of optimal protocols with $\tau_{eq} = 20$ ms, $\lambda_i = 1.5\ pN/\mu m$, $\Delta\lambda = 10\lambda_i$ and different protocol times: $\tau_P = 0.1\tau_R$ (left) and $\tau_P = 2\tau_R$ (right), where $\tau_R = \gamma/\lambda_i \approx 12$ ms is the relaxation time in the state λ_i.

Source: By the author.

where the subindex "$-$" represents the point just before the jump, and "$+$" is the point just after it, as in Eq. 5.30. However, if the interval between acquisitions is very small, $\Delta t \to 0$, then $x_+ \approx x_-$ and Eq. 4.11 keeps its validity. The resulting curves for the temporal evolution of work have smoothened exponential growth instead of jumps and this effect is more evident in short protocols, as depicted in Fig. 35 (left).

Then, the work probability distributions of the optimal protocols can be obtained from the final value of $W(\tau_P)$ for 10^4 trajectories. A comparison of the optimal results with the linear ones (presented in Chapter 4) confirmed the best efficiency of the optimal solution. Fig. 36 compares the probability distributions in both cases for different

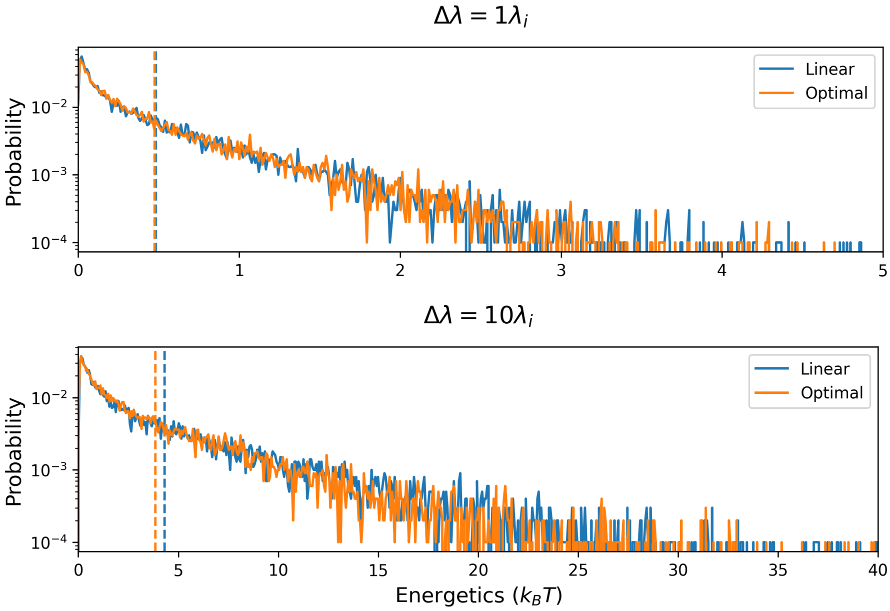

Figure 36 – Work probability distributions (solid lines) and their corresponding average values (dashed lines) for different modulation amplitudes $\Delta\lambda = \lambda_i$ (top), and $\Delta\lambda = 10\lambda_i$ (bottom). Results from 10^4 trajectories for linear protocols, in blue, and optimal ones, in orange. Here, $\tau_{eq} = 20$ ms, $\lambda_i = 1.5\ pN/\mu m$, $\tau_P = 0.1\tau_R$, where $\tau_R = \gamma/\lambda_i \approx 12$ ms is the relaxation time in the state λ_i.
Source: By the author.

modulation amplitudes $\Delta\lambda = \lambda_i$ (top), and $\Delta\lambda = 10\lambda_i$ (bottom) and fixed protocol time, $\tau_P = 0.1\tau_R$, where τ_R is the relaxation time in the state λ_i.

Looking at the dependency of the average values of work on the protocol time (Fig. 37) with different modulation amplitudes, $\Delta\lambda = \lambda_i$ (left) and $\Delta\lambda = 10\lambda_i$ (right), the optimal protocols have a smaller value of mean work than the linear ones. However, such a difference increases for intermediate protocol times. When the processes are performed very quickly, the mean work value corresponds to the one expected in a simple jump. For longer protocol times, closer to the equilibrium limit, the average work of both processes converges to ΔF, independently of the protocol type, as discussed previously. Thus, in the region between these two cases, a higher "efficiency" of the optimal curves in comparison to the linear (suboptimal) ones is observed.

Using Eq. 5.18, predictions of the average work for optimal protocols can be compared to experimental results, showing a good agreement (Fig. 37). Complementary to the analysis of the dependency of the mean work value on the protocol time, Fig. 38 displays the dependency on $\Delta\lambda/\lambda_i$, and one has similar observations. Here, the difference between optimal and suboptimal results increases as the trap is changed for larger values of λ_f, i.e., bigger modulation amplitudes.

As shown in Fig. 39, which displays the dependency of variance for different protocol times (left) and modulation amplitudes (right), the work variance of optimal protocols

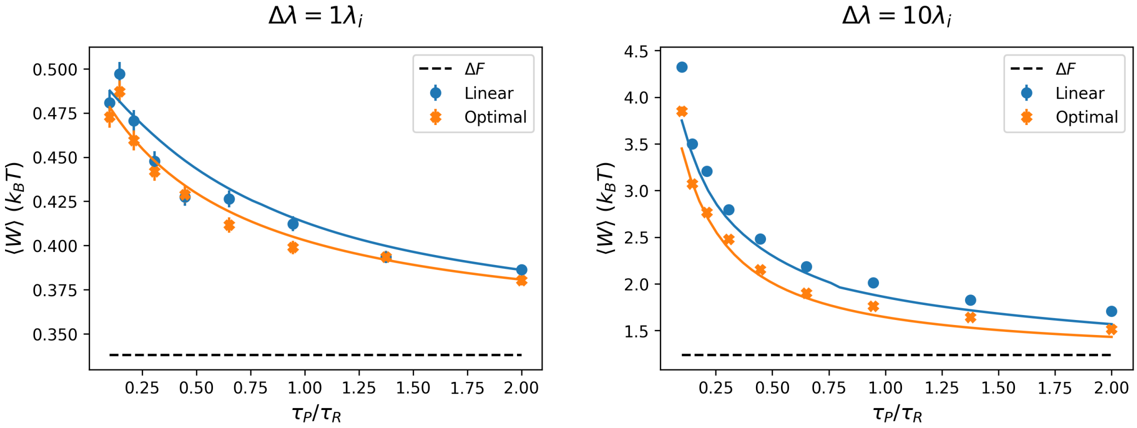

Figure 37 – Experimental measurements of the average (stochastic) work for an ensemble of 10^4 trajectories in function of protocol time. Experimental results are represented by dots and theoretical predictions are denoted by solid lines. Values obtained from linear protocols, in blue, and optimal ones, in orange, with $\tau_{eq} = 20$ ms, $\lambda_i = 1.5\ pN/\mu m$ and different modulation amplitudes $\Delta\lambda = \lambda_i$ (left), and $\Delta\lambda = 10\lambda_i$ (right), where $\tau_R = \gamma/\lambda_i \approx 12$ ms is the relaxation time in the state λ_i. The uncertainties are smaller than the dots.

Source: By the author.

is also lower than the linear ones. However, both decrease as we converge to a regime close to equilibrium, i.e., for protocols performed slowly and with small trap stiffness change.

Jarzynski's equality was also verified as an independent test. Fig. 40 shows that the results for optimal protocols are similar to those for the linear case studied in Chapter 4, as expected. Since the free energy difference depends only on initial and final states, the values of $\langle \exp(-W/k_BT) \rangle$ depend neither on the protocol time, as discussed previously, nor on the path of the particle in the phase space, i.e. if it is optimal or not. Here, a minor deviation was also observed for slower protocols with bigger modulation amplitudes, probably due to the same issue with the amplification factor calibration discussed in Chapter 4.

5.4 Conclusions

This chapter focused on the implementation of the optimization proposed by Schmiedl and Seifert (74) for moving laser traps (simulation) and compressing protocols (experiment).

Despite the experimental difficulties in maintaining a constant optical potential shape and tracking the particle during the modulation of the trapping beam position, the moving trap case was explored via numerical simulations, which are essential for gaining insights for future experiments. Therefore, the parameters chosen for the simulation correspond to those that work better for the Setup IFSC-USP requirements (low force constant and small angle modulation of the trapping beam). The results show that the

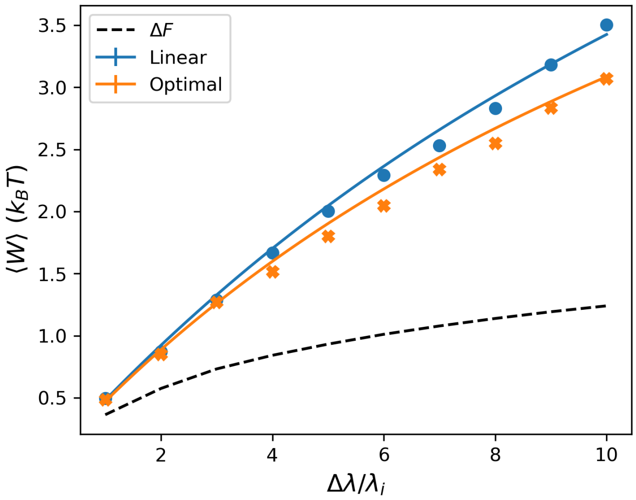

Figure 38 – Experimental measurements of the average (stochastic) work for an ensemble of 10^4 trajectories in function of the modulation amplitude. Experimental results are represented by dots and theoretical predictions are denoted by solid lines. Values obtained from linear protocols, in blue, and optimal ones, in orange, with $\tau_{eq} = 20$ ms, $\lambda_i = 1.5\ pN/\mu m$ and $\tau_P = 0.145\tau_R$, where $\tau_R = \gamma/\lambda_i \approx 12$ ms is the relaxation time in the state λ_i. The black dashed line represents the free energy difference. The uncertainties are smaller than the dots.

Source: By the author.

optimal protocols' mean work value is smaller than that of linear (suboptimal) ones for the available parameters. Besides, there exists a region concerning the protocol time where the "efficiency" of the process is more significant, which is in the order of τ_R. On the other hand, the slight difference between optimal and suboptimal in this parameter's range makes the experimental test challenging.

Although the mean value can be obtained for 10^5 trajectories, as shown in the simulated results, verifying Jarzynski's equality can generally be more complex in this case. Since work may have negative values, the rare events contribute to $\langle e^{-W/k_BT}\rangle$ and a larger number of trajectories are necessary, making it even more challenging for an experimental implementation.

However, the experimental verification for the compressing protocol case was successfully implemented. As described in Chapter 4, the test was performed via modulation of the trapping beam intensity. After the required calibrations, the optimal protocol was applied for different protocol times and modulation amplitudes. The mean value from work distributions, $\langle W\rangle$, and $\langle e^{-W/k_BT}\rangle$ were obtained for each group for ensembles of 10^4 trajectories. The results are consistent with the theoretical prediction for all cases, and, again, minor deviations occurred for more extensive modulations of the trap stiffness and shorter protocol times due, most likely due to difficulties with the amplification factor calibration, as discussed previously.

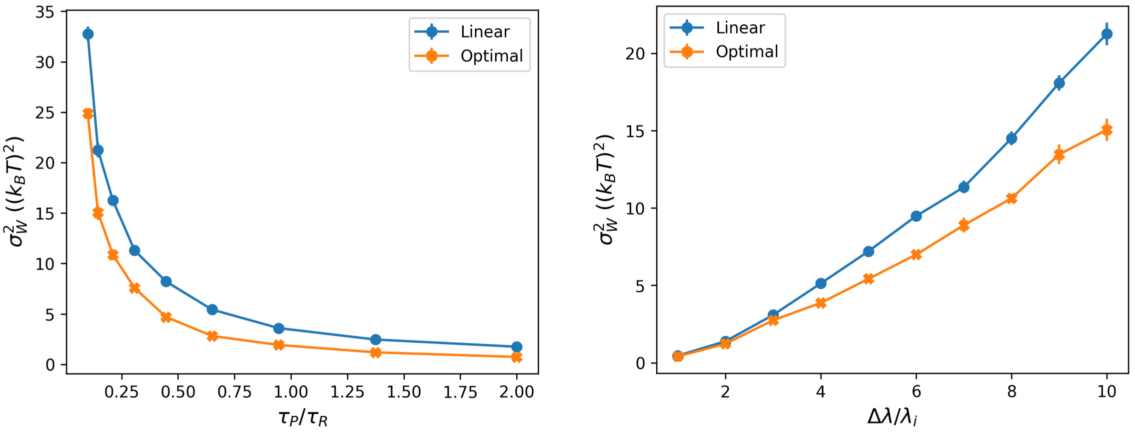

Figure 39 – Protocol time dependency of work variance for $\Delta\lambda = 10\lambda_i$ (left) and amplitude modulation dependency of work variance for $\tau_P = 0.145\tau_R$ (right). Values obtained from linear protocols, in blue, and optimal ones, in orange, from 10^4 trajectories with $\tau_{eq} = 20$ ms, $\lambda_i = 1.5\ pN/\mu m$, where $\tau_R = \gamma/\lambda_i \approx 12$ ms is the relaxation time in the state λ_i. The uncertainties are smaller than the dots.

Source: By the author.

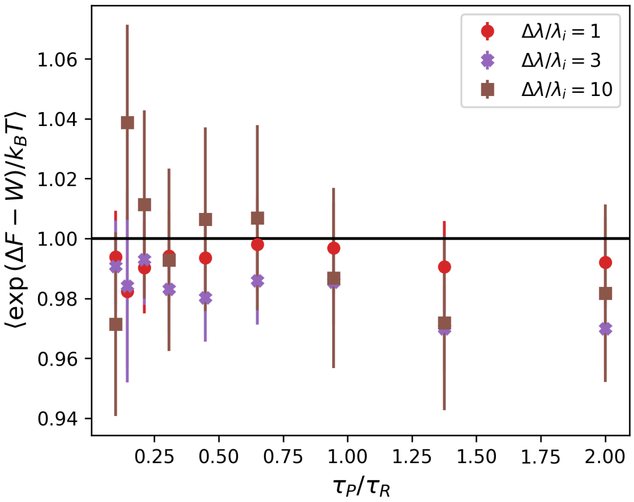

Figure 40 – Jarzynski verification for experiments with optimal protocols. Final results of $\langle e^{\Delta F - W/k_B T} \rangle$ for different protocol times and modulation amplitudes: $\Delta\lambda = \lambda_i$, $3\lambda_i$, and $10\lambda_i$ in red, purple, and brown, respectively. The black continuous line represents the expected value. Results for $\tau_{eq} = 20$ ms, and $\lambda_i = 1.5\ pN/\mu m$, where $\tau_R = \gamma/\lambda_i \approx 12$ ms is the relaxation time in the state λ_i.

Source: By the author.

Besides a comparison of experiment and theory for the optimal process (74), the work distributions of optimal and linear (suboptimal) processes were also compared[†]. As expected, the optimal processes have smaller mean work than the linear ones and efficiency increases for intermediate protocol times, such as the moving trap case.

[†] Data collected for both cases were obtained for the same trapped particle.

Therefore, our experimental test generally confirms the predictions of Schmiedl and Seifert (74) even in the presence of a relatively small delay in the implementation of jumps in the control parameter (laser intensity modulation). According to (70), such an effect adds a tiny correction to the results from protocols with discontinuities. The difference between sharp and smoothened cases depends on the rising time of the curve and can be considered negligible for our experimental parameters.

Towards further minimizing that effect, the experiments were repeated in the Setup IFSC-USP to take advantage of its faster modulation response (around 10^{-6} s). Nevertheless, due to high-frequency noise, reliable results could not be obtained for the complete set of parameters presented in this chapter. The optimal protocols were initially tested in the first version of the IFSC-USP system for a smaller set of parameters and were presented in (83). In late 2023, the experiment was repeated with the improved Setup IFSC-USP, described in Chapter 3, and around the same time, we learned about similar experiments conducted by Rosales-Cabara et al. (70, 84) in Strasbourg through slightly different protocols.

To the best of our knowledge, this is the first systematic direct experimental test for Schmiedl and Seifert's predictions (74). In addition to such a contribution, the knowledge gained from those studies provided our group with the ability to use optical tweezers to control and measure stochastic thermodynamics variables precisely, opening doors for future experiments in our laboratory, such as exploration of non-harmonic potentials based on approximations, as proposed by (77, 78, 80), or even for more complex scenarios involving feedback-control, as discussed in the next Chapter.

6 INFORMATION-TO-ENERGY CONVERSION

The use of feedback in optical tweezer systems has proven an exciting possibility for a variety of applications, such as the removal of drifts and noise through active feedback of the stage position (85), generation of generic virtual potentials based on particle position feedback (25), among others in the field of control.

In this scenario, this chapter addresses the implementation of a first feedback protocol from our laboratory at IFSC-USP using optical tweezers. The motivation behind it refers to the development of a series of new studies involving feedback and information-to-energy conversion. The experiment was based on Maxwell's demon idea, in which a given change in the optical potential is applied according to the previous particle position information.

Firstly, Maxwell's demon and the way information translates into the generalized Jarzynski equality are briefly discussed. Then, the feedback system, the calculations of work values, and the experimental results for protocols with and without feedback exploring different demon criteria are then presented. Finally, conclusions and next steps are provided.

6.1 Maxwell's demon

Maxwell's demon (86) is an emblematic thought experiment in the history of thermodynamics, presented in 1867 in *Theory of Heat* (87). To understand it, let us imagine a gas composed of a collection of molecules with different velocities. The kinetic temperature related to the gas will be proportional to the mean-square velocity of the particles that it is composed of (88). This gas is then divided into two thermally isolated chambers initially at the same temperature and separated by a frictionless door that can quickly open and close. The door is controlled by a demon capable of discerning which molecules move faster and which move slower. When a particle with higher velocity approaches the door, the demon opens it, allowing the particle to pass to the other side. After several particles with higher velocity have passed to the other chamber, the average velocity of the molecules on one side is higher than the other, leading to a difference in their kinetic temperatures. Since the system consists of two thermal reservoirs, i.e., a hot one and a cold one, a heat engine from which work could be extracted can be built, seemingly violating the Second Law of Thermodynamics.

Following Maxwell's idea, a second important thought experiment was suggested by Leo Szilard, in 1929 (89). The proposed system has a single ideal gas particle and an initially fixed piston between two chambers to replace the door of Maxwell's demon experiment. When the demon sees the chamber where the particle is located, it decides to place a mass on the piston on the left or right side – on the left if the particle is in the left chamber and on the right if it is on the right side. Consequently, the particle expands the chamber, pulling the piston so that the mass rises against gravitational force, performing work. Since the particle in this system can be in two different positions, left or right, these two states are analogous to one bit of information.

Despite such a new thought experiment and special attention on the subject, the explanation for those anomalies was a dilemma for a long time. Almost a century later, Landauer finally exorcised the demon, proposing the role of information in physical processes (90). In Landauer's prediction, the information is physical, and the minimum energy necessary to erase one bit is $k_B T \ln 2$ (91).

To understand the minimum value for energy, let us return to the Szilard engine scenario. Considering the particle has a probability $p_i = 1/2$ of being in one of the two states, Gibbs entropy is given by (92)

$$S = -k_B \sum_i p_i \ln p_i. \tag{6.1}$$

Therefore, the entropy of one bit of information is $k_B \ln 2$. Since the Second Law of thermodynamics states (Eq. 2.4)

$$\delta S > \frac{\delta Q}{T}, \tag{6.2}$$

where Q is heat and T is bath temperature, the minimum energy required for erasing one bit of information will be $k_B T \ln 2$, which is called Landauer's principle (91).

After that exciting proposal, the first experimental verifications of one bit's partial (24) and full (25) erasure were made using double wells in optical tweezers and several proposals have emerged towards converting information into useful energy (22, 28, 93).

In this scenario, as a possible way to estimate the efficiency in information-to-energy conversion for a given process, the Jarzynski equality was proposed (94):

$$\langle e^{(\frac{\Delta F - W}{k_B T})} \rangle = \alpha, \tag{6.3}$$

where α indicates the degree of control in the experiment. When $\alpha = 1$, no information on the system is provided, and the results are the same as the usual Jarzynski's equality (Eq. 2.10). However, adding feedback to the system leads to $\alpha > 1$. The following sections will explore implementing a simple feedback system to compute the generalized Jarzynski equality for our experimental apparatus.

6.2 Proposed feedback protocol

A possible system capable of converting information to energy can be developed through the implemention of a feedback control of the optical potential. Similarly to the aforementioned experiments, the stiffness of the trap will continue to be modulated (compressing protocol). However, both initial and final state changes will be discontinuous in a step protocol, i.e. the protocol time is approximately zero, as discussed in (69).

In this system, the instant at which the trapping laser intensity is increased depends on the real-time data acquisition of the particle's position. If it satisfies the demon's criterion, which in our case corresponds to being within a spatial region around the trap's equilibrium position, the change occurs. Otherwise, nothing happens.

The scheme in Fig. 41 was used for the implementation of the demon. The particle starts in a state λ_i and is kept in it towards equilibrating for a time longer than the relaxation time $\tau_{eq} > \tau_R$. Then, the particle's position, x, starts being monitored. If $|x|$ is smaller than a defined threshold, here denoted as x_S, the demon switches the potential, taking the particle to a final state $\lambda_f > \lambda_i$, as shown in Fig. 42. Otherwise, the tracking continues until the condition has been satisfied. After the particle has thermalized in the state λ_f, the system is reset by switching back to λ_i and the process repeats.

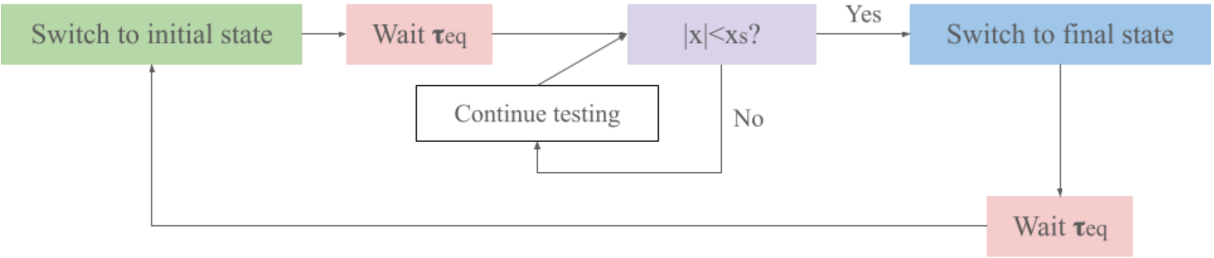

Figure 41 – Scheme of the feedback implementation. It starts with the preparation of the particle in state λ_i for an equilibrium time τ_{eq} and the bead's position is then acquired for switching the state to λ_f when $|x| < x_S$.
Source: By the author.

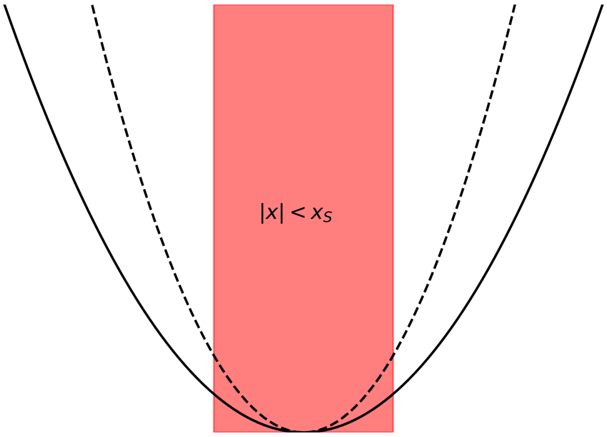

Figure 42 – Scheme of the switch in the particle's state when $|x| < x_S$. The initial state, λ_i, is represented by the solid line and the final state, λ_f, is denoted by the black dashed line.
Source: By the author.

6.3 Work calculation and time delay

For a protocol that consists of an immediate jump from λ_i to λ_f, the work (Eq. 2.7) is given by (69):

$$W = \frac{\Delta\lambda}{2} x^2, \tag{6.4}$$

and its average value is

$$\langle W \rangle = \frac{\Delta\lambda}{2} \langle x^2 \rangle, \tag{6.5}$$

where $\langle x^2 \rangle = k_B T / \lambda_i$ comes from the equipartition theorem (see Sec. 3.2.1). Then, the expected variation in trap stiffness $\Delta\lambda$ and the bead's position at the switch's instant are enough to obtain the work values for each trajectory.

In an ideal system, the switch would occur immediately after the demon has known the particle's position is in the interval of interest. However, in an actual physical system, due to limitations in processing, a delay time interval, t_{delay}, must be considered between the position reading and the real potential change. During t_{delay}, the position evolves according to the solution of the Fokker-Plank equation (Eq. 2.22), decreasing the efficiency of the demon, as discussed in (69).

For our experimental configuration, due to a lack of equipment capable of processing commands in hardware time, a *Python* code that reads the position, makes the decision, and applies the switch in software time was implemented. Therefore, the particle's position is tracked at instant t_0 and there is a delay δt_P for the processing of the input signal, i.e. for testing if the particle is located in the region of interest. If $|x| < x_S$, the switch signal is sent to the modulator at the instant $t_1 = t_0 + \delta t_P$ and there is another delay due to the AOM response, $\delta t_m \sim 10^{-6}$ s. Immediately after that, the change in the potential is implemented and another position is acquired at $t_2 = t_0 + \Delta t$, where Δt is the interval between the acquisitions.

Although the scenario enables no computation of the values of x at the instant at which the optical potential is switched, the following work values can be defined:

$$W_- = \frac{\Delta\lambda}{2} x_-^2, \tag{6.6}$$

$$W_+ = \frac{\Delta\lambda}{2} x_+^2, \tag{6.7}$$

where $x_- = x(t_0)$ corresponds to the case in which there is no delay in the experiment, i.e. $\delta_p + \delta t_m \to 0$, and $x_+ = x(t_2)$ corresponds to the worst case scenario, where $\delta_p + \delta t_m \to \Delta t$.

Although the bead's position must be acquired only after thermalization, it was collected simultaneously with the PD signal throughout the experiment. The detection of the switch instant is reported in the Appendix A.

Since the delay time is not fixed, estimating the mean interval between measurements is important and depends on the computer's processing time. After all computer settings have been optimized, the following distribution of Δt is established for the application of a set of $3 \cdot 10^4$ protocols. As shown in Fig. 43, the events with $\Delta t \approx 1$ ms are mostly likely, but much faster acquisitions are also performed. Therefore, the delay time is kept as short as possible and the region of interest is controlled with the use of different threshold values, x_S.

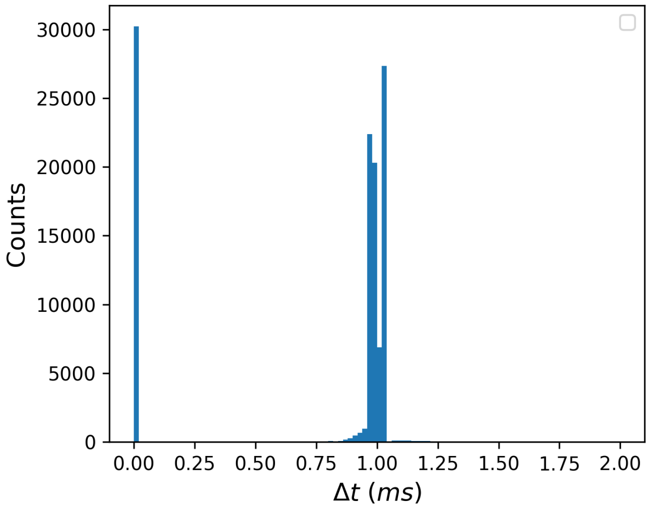

Figure 43 – Histogram of the time interval between acquisitions, Δt, for 1000 protocols. The histogram has 100 bins.

Source: By the author.

6.4 Protocol application and experimental results

The application of the feedback protocols requires the system to be characterized, as described in the previous sections. Therefore, the PSD curves were obtained from the position time-series of one trapped silica microsphere (see Sec. 3.2.4). The dependency of κ_x for different laser powers is $\kappa = m_{TS} V_{PD} + b_{TS}$, where $m_{TS} = 2.41 \pm 0.03$ (pN/μm)/V and $b_{TS} = 0.08 \pm 0.04$ pN/μm.

The amplification factor, which converts the voltage output signal from QPD to meters, was obtained in a different way. Since the experiment required the position of the particle relative to the equilibrium position, $x = (x_{QPD} - x_{offset})/S_x$, prior to each protocol application, the position time series of the particle in state λ_i was collected for 100 s at 100 kHz. Besides $x_{offset} = \langle x_{QPD} \rangle^*$, PSD was computed and $S_x = 0.705 \pm 0.003$ μm/V was obtained for all measurements presented in what follows[†].

---

[*] Note the equilibrium position has the contributions of QPD offset due to the circuit configuration and possible misalignment between trapping and detection lasers.

[†] Since $N = 30$ position time series of 100 s each at 100 kHz were acquired, 30 different results for S_x obtained from each PSD curve are provided. Therefore, the mean of these values and the uncertainty, $\delta S = \sigma_S/\sqrt{N}$, obtained from the standard deviation, σ_S, were considered.

After the system has been characterized, the protocols can be applied to different thresholds, x_S, as shown in Fig. 44. In this chapter, all protocols initiate in $\lambda_i = 1$ pN/μm for $\tau_{eq} = 40$ ms $\approx 2\tau_R$ and switch to $\lambda_f = 2$ pN/μm. As discussed in (69), due to the presence of the demon, a larger number of protocols is required for the computation of $\langle \exp\left(\frac{\Delta F - W}{k_B T}\right)\rangle$. Therefore, $3 \cdot 10^4$ protocols were performed for each threshold.

Fig. 44 shows the particle's position during the feedback protocol for different values of x_S. Notably, the switch is activated at the exact instant of the narrowing of the waist of the positions and the width of such waist will depend on the threshold x_S. However, the time delay for the detection of the change (used here to identify the starting point of the protocol) depends on the acquisition rate, as previously addressed.

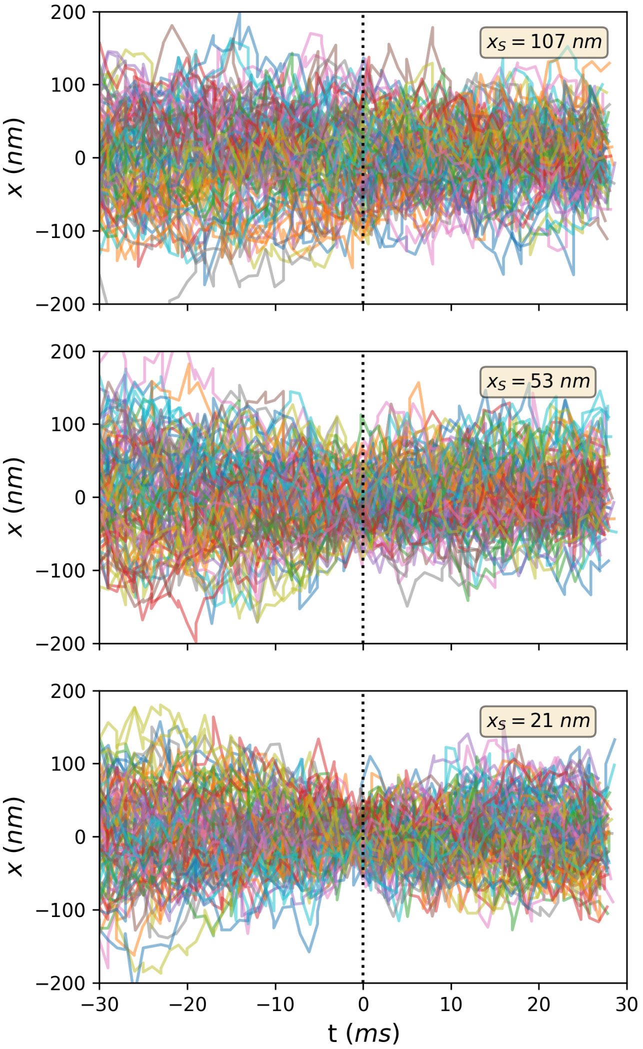

Figure 44 – Trajectories for 100 protocols with different threshold values $x_S = 107$, 53, 21 nm (from top to bottom). The black dashed line corresponds to the laser's detection moment of the switch.

Source: By the author.

Therefore, computing the values of work, W_- and W_+, for an ensemble of trajectories leads to the probability distributions of the quantities, as shown in Fig. 45. Besides the protocol with feedback, the simple step protocol, in which the switch is performed just after the thermalization period with no information on the bead's position, was also studied.

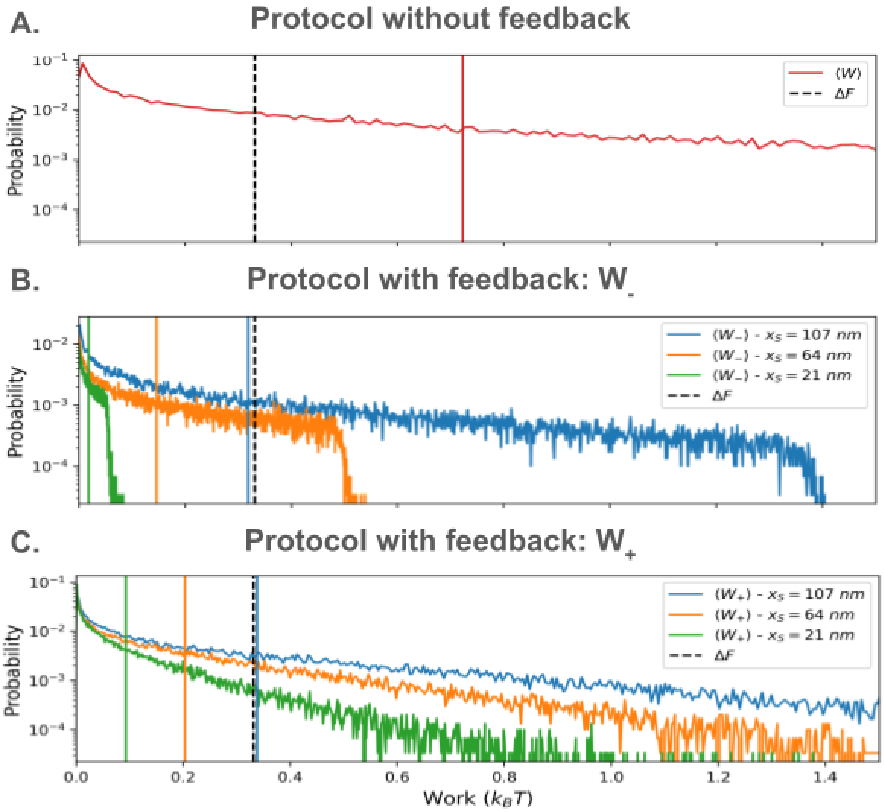

Figure 45 – Probability distributions of work and their average values (vertical solid lines) for the step protocol without feedback (A) and with feedback - W_- (B) and W_+ (C). The protocols with feedback were applied for different threshold values: $x_S = 107, 64$ and 21 nm in blue, orange and green, respectively. The Black dashed line represents the free energy difference. The original histograms have 1000 bins obtained from $3 \cdot 10^4$ trajectories. Here $\lambda_i = 1$ pN/μm, $\lambda_f = 2\lambda_i$ and $\tau_{eq} = 40$ ms.

Source: By the author.

The work distribution of the simple step protocol has a long tail, as displayed in Fig. 45 (A) and the average work value depends on $\langle x(0)^2 \rangle$ at the initial instant. According to Eq. 6.5, the theoretical value is expected to be $\langle W \rangle = 0.5$ $\mathrm{k_BT}$ and the experimental result for the average work is $\langle W \rangle = 0.723 \pm 0.006$ $\mathrm{k_BT}$[‡]. The coefficient α, from Eq. 6.3, can be computed by $\langle \exp\left(\frac{\Delta F - W}{k_B T}\right) \rangle = 0.90 \pm 0.02$ and, in case of no feedback, theoretically, it should be equal to 1. Therefore, a small deviation between experiment and theory is observed and occurs due to the noise present in the system at higher frequencies, as described in Appendix B.

[‡] The uncertainties were obtained in the way described in Sec. 4.

Here, we collected data at a reduced acquisition frequency, $f = 1/\Delta t \approx 1$ kHz, due to the limitation of the software time (Fig. 43). Consequently, no low-pass filter[§] can be applied in the particle's position during data analysis, thus clearly affecting $\langle x^2 \rangle$. If x^2 is bigger than expected due to the noise contribution, the average work is overestimated and $\langle \exp(\frac{\Delta F - W}{k_B T}) \rangle$ is underestimated. Despite this small deviation, the protocols' results can be compared with the feedback activated for different thresholds.

Fig. 45 (B) shows the work probabilities from W_- (Eq. 6.6), which is an ideal scenario since it is considered the application of the switch immediately after the particle's detection in the position of interest. The tail has an abrupt cutoff at work values bigger than $\Delta\lambda x_S^2/2$, causing the average work and variance values to decrease as x_S decreases.

The tail becomes smoother in the other extreme case, W_+ (Eq. 6.7), due to the bead's position evolving from that moment onwards, as depicted in Fig. 45 (C). Between the detection instant and the actual switch of the potential, it evolves in the trap corresponding to λ_i, after which it evolves with the trap corresponding to λ_f. Due to the difficulty in modelling the particle's behavior for those different contributions to be taken into account, the actual work, W, associated with the feedback protocol in the present system is considered to lie within $\langle W_- \rangle < \langle W \rangle < \langle W_+ \rangle$.

Fig. 46 displays the average work values from conditions W_- (Eq. 6.6) and W_+ (Eq. 6.7) for all explored thresholds. Almost all of them are smaller than ΔF and tend to zero as x_S decreases in an approximately linear dependency. Although such results seem an apparent violation of the Second Law of Thermodynamics, that is not the case, since the role of information and the use of feedback must be considered to do the information-to-energy conversion.

The convergence of term $\langle \exp(\frac{\Delta F - W}{k_B T}) \rangle$ can be examined for different numbers of trajectories under the same protocol for studies of the generalized Jarzynski equality. Although (69) predicts many repetitions for Jarzynski convergence, Fig. 47 (left) shows approximately 5000 protocols seem sufficient. Moreover, as the threshold decreases, the convergence occurs more rapidly.

The results for different threshold values show the dependency of efficiency, α, is inversely proportional to threshold x_S, as depicted in Fig. 47 (right). Again, the true value of α lies between those calculated from W_- and W_+, which are closer for large x_S and start to diverge for small x_S.

[§] To filter the high-frequency noise on data, as discussed in Appendix B, a low-pass filter with cutting frequency in 3 kHz must be applied. However, if the acquisition frequency is smaller than this value, applying this filtering process is not possible.

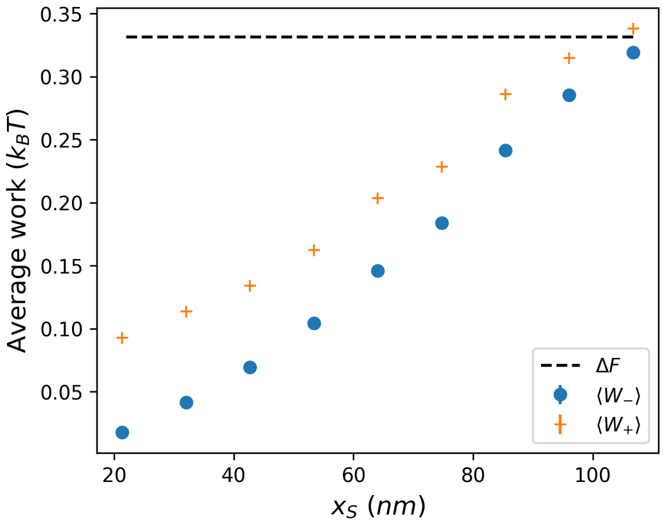

Figure 46 – Average work for W_-, in blue, and W_+, in orange, for different threshold values. Each point corresponds to the average of $3 \cdot 10^4$ trajectories. Here, $\lambda_i = 1$ pN/μm, $\lambda_f = 2\lambda_i$ and $\tau_{eq} = 40$ ms. The black dashed line represents the free energy difference. The uncertainties are smaller than the dots.
Source: By the author.

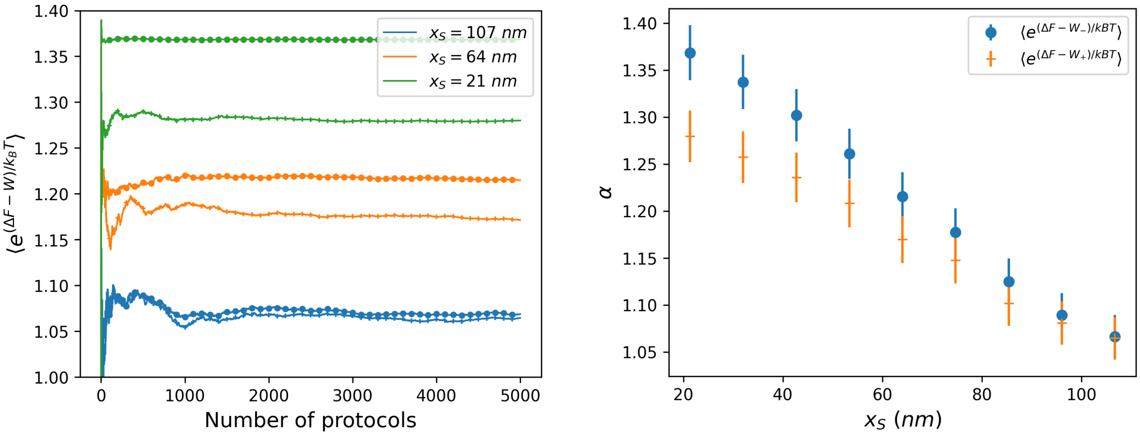

Figure 47 – Convergence of Jarzynski equality for different thresholds $x_S = 107$, 64 and 21 nm in blue, orange, and green, respectively (left). Points represent values obtained from $\langle \exp\left(\frac{\Delta F - W_-}{k_B T}\right) \rangle$ and crosses from $\langle \exp\left(\frac{\Delta F - W_+}{k_B T}\right) \rangle$. Dependency of α in the threshold x_S (right) obtained from $3 \cdot 10^4$ trajectories for $\langle \exp\left(\frac{\Delta F - W_-}{k_B T}\right) \rangle$ in blue and $\langle \exp\left(\frac{\Delta F - W_+}{k_B T}\right) \rangle$ in orange.
Source: By the author.

6.5 Conclusions

This chapter addresses the implementation of a simple feedback system in which the particle's potential is altered from a less confined state to a more confined one when the particle's position is observed in a region of interest. Summarizing, a Python code prepares the system at λ_i while keeping the potential fixed for a time τ_{eq}. Then, the particle's position starts to be checked and if $|x| < x_S$, a switch to λ_f state is performed.

After reaching equilibrium, the system returns to λ_i and the process repeats.

Since the system was implemented with no regular data acquisition and the time between collections was limited by the software loop (corresponding to approximately $\Delta t \approx 1$ ms), no verification of the particle's exact position when the laser power changes was possible. Therefore, the work values from Eq. 6.4 were analyzed considering x_- (collected position that satisfies $|x| < x_S$) and x_+ (next collected position after a time interval Δt). Therefore, the actual result should lie within the $W_- < W < W_+$ interval for the feedback protocols.

Apart from protocols with feedback, data for a simple step protocol were also acquired. Comparing the work probability distributions, it is notable that the feedback increases work efficiency compared to the simple step case. The average work values obtained in feedback protocols for the studied parameter set were lower than the free energy difference, justified by the information-to-energy conversion. The dependency of mean work on the threshold is approximately linear, with it tending to zero as the threshold decreases. As expected, for the generalized Jarzynski, the α value obtained increases as the threshold decreases. Therefore, information is used here to apply less work in the system to change its state, and the results presented in this chapter illustrate the correspondence between information and energy for compressing traps.

Despite the current hardware limitation for the demon's implementation, the experiment was a first step towards experimental explorations of feedback control in our group, thus opening possibilities for new and more complex protocols, such as creation of virtual potentials via feedback and other experiments aiming at information-to-energy conversion. The next steps include the addition of field-programmable gate arrays (FPGAs) for faster criterion-based actions, enabling more sophisticated implementations.

7 STUDY OF OPTICALLY ACTIVE SUPER-CRYSTALS IN A TRAP

Until now, our research has focused on the classical regime, in which stochastic thermodynamics was studied through different types of protocols using trapped microscopic particles with no quantum effects involved. However, this chapter proposes transitioning towards the classical-quantum interface, exploring trapped colloidal super-crystals of quantum dots.

Quantum dots are nanometric structures composed of semiconductors with notable quantum properties, such as single photon emission, originating from the quantum confinement of electrical charges. In general, semiconductor materials exhibit a significant gap (absence of energy levels or bands) between the valence band, where electrons are bound to atoms, and the conduction band, where electrons roam within the crystal. A minimum energy, often via heat or light, is required so that electrons can transition from the valence to the conduction band, leaving a hole in their original positions.

In bulk semiconductors, the energy levels between bands are continuous. However, when the size of the material decreases to the order of the nanometric scale, the levels become discrete due to the confinement of the charge carriers in all three dimensions. Such a quantum behavior, allied to the versatility of controlling absorption and emission spectra via material engineering, enables studies of different quantum phenomena using these objects. Consequently, there are numerous applications of systems with quantum dots, such as construction of displays (95–96), development of light sources (97) and photovoltaic cells (98–99), scientific advancements in imaging biological systems (100), quantum computing (101–103), and information processing (104–107), among other studies. This vast array of applications culminated in the 2023 Nobel Prize in Chemistry for the discovery and synthesis of this material (108–110).

This research focuses specifically on super-crystals formed by spherical quantum wells (SQWs) (111). Such structures have controllable arrangements and sizes - of the order of micrometres - making them easier to be trapped and manipulated with an optical tweezers system. Besides, when an ensemble of quantum objects is combined, collective quantum effects originating from the particle synchronization may be expected.

Particularly, one expects that the target particles present the so-called superradiance effect (112–113). This phenomenon occurs when a massive number of emitters interact with a common excitation source. When the distance between the emitters is smaller than the light wavelength, the emitters interact collectively, generating a high-intensity pulse coherently and directionally. This effect amplifies the emitted radiation intensity compared to uncorrelated photon emission and can be the differentiator in a system with significantly higher thermal energies, like room-temperature optical tweezers. This effect was recently observed in three-dimensional superlattices of quantum dots (114) and in a room temperature system (115). Therefore, observing possible mechanical signatures of that collective quantum phenomenon was the initial motivation for this research.

Thus, through an adapted optical tweezer setup that enables the trapping and excitation of the material of interest, our aim was to understand the interplay between those optically active microstructures' mechanical and optical properties. In particular, looking at the particle movement confined within a trap, our expectation was to detect quantum features inherent to this system and measure their effects on the particle dynamics.

First, the colloids of quantum dots used are presented and a general description of the particle dynamics is provided. Modifications performed in the experimental system necessary for the exploration of quantum properties and characterization of the optical potential felt by the particle are shown and the first experimental results, the preliminary conclusions, and future plans are reported.

7.1 CdS/CdSe/CdS quantum dots colloids

Quantum dots can contain various base elements such as cadmium, lead, and indium and, depending on their material and structure, they can be applied for different purposes. Here, our focus is on SQWs formed by Cadmium Selenide (CdSe) and Cadmium Sulfide (CdS) with the CdS/CdSe/CdS structure and synthesed according to (111), as depicted in Fig. 48 (inset). As detailed in (116), this material is an exceptional source of single photons with complex decay dynamics characterized by excitons (electron-hole pairs) and defects emission. The SQWs used were synthesized by Zhu Meng and Benoït Maller at Institut Lumière Matière.

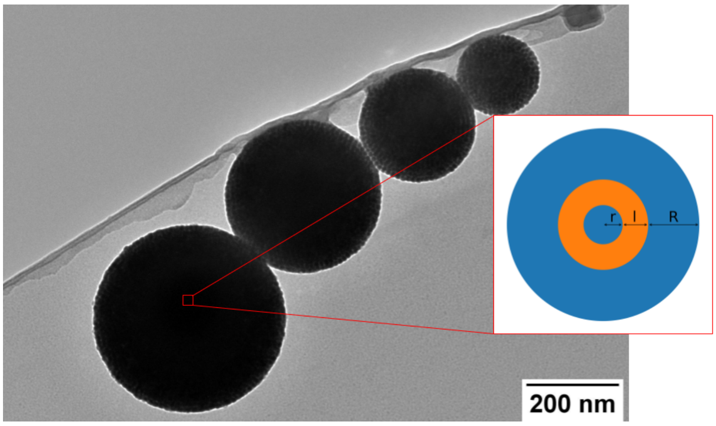

Figure 48 – TEM image for super-crystals of many SQWs of different sizes and scheme of a single SQW structure (inset). Here, the CdS is in blue, and the CdSe is in orange, and typically $r = 1.3$ nm, $l = 1.7$ nm and $R = 3.4$ nm.
Source: By the author.

The super-crystal colloids are composed of SQWs arranged in a face-centred cubic packing and can have different sizes, from tens of nanometers to micrometers. They were constructed in collaboration with Chiara Moretti and Benjamin Abécassis at Laboratoire de Chimie ENS de Lyon. Their basic synthetization consists of a self-assembly process - more details can be found in (114). Basically, droplets of SQWs formed by shaking the sample are slowly evaporated, constructing self-arranged super-crystals. The number of quantum dots is approximately $N_{SQW} \approx 10^8$ for a micrometric sphere, typically used in this research.

Fig. 48 shows the image obtained with Transmission Electron Microscopy (TEM) for super-crystals of different sizes and Fig. 49 displays the absorption and emission spectra, revealing a broad absorption band and an emission peak around 650 nm*

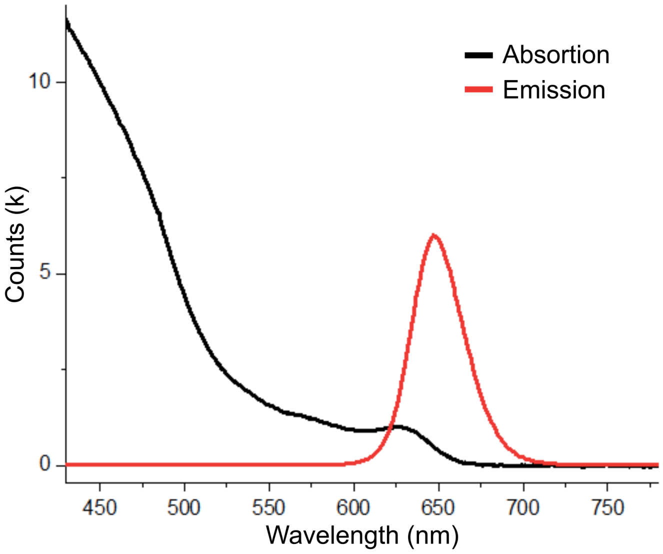

Figure 49 – Absorption and emission spectra of super-crystals formed by SQWs (CdS/CdSe/CdS).
Source: By the author.

7.2 Mechanical dynamics in the trap

This research aims to investigate the coupling between colloids' mechanical and optical properties. Therefore, a pulsed laser was used to excite the trapped particles while observing the response in the bead's centre of mass movement. Thus, this chapter describes the dynamics of our system and the expected results.

In general, when a photon of light is shone onto an optically active material, three phenomena can occur: reflection, refraction, and absorption/emission. Since photons carry momentum, as discussed in Chapter 3, a recoil force is generated in the material for each incident photon with altered direction or energy.

---

* Complementary measurements of the colloid's lifetime were performed by confocal microscopy in collaboration with Julien Laverdant and Florian Kulzer from Institut Lumière Matière. The analysis is in progress.

First, let us consider the simplest case in which N_p photons with wavevector $\vec{k}$ propagate in a plane wave. The momentum of each photon will be $\vec{p} = \hbar\vec{k}$, where $\hbar$ is the reduced Plank's constant. Therefore, the amplitude of the optical force related to the absorption of N_p photons in a time duration τ is given by $N_P\hbar\vec{k}/\tau$.

Since computing the exact force can be challenging for absorption/emission, the extreme scenario, where all photons are absorbed when the particle is illuminated with a quasi-resonant pulsed laser source, represented in Fig. 50, is considered. For this case, if the average beam power is defined as P_{mean}, the repetition frequency $1/T$, and the pulse duration τ, the approximate number of photons of each pulse is given by $N_{ppp} = P_{mean}T/E_p$, where $E_p = hc/\lambda$ is the energy of a single photon and c is the speed of light in vacuum.

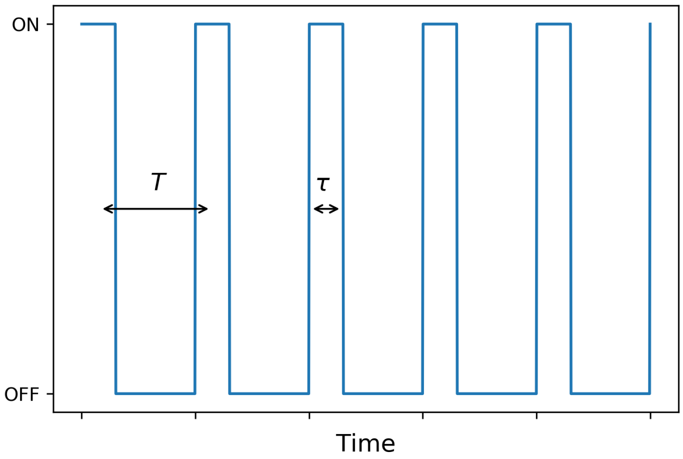

Figure 50 – Diagram of the pulsed laser temporal profile showing the periods when the laser is on and off. Here, T is the repetition time and τ is the pulse duration. Source: By the author.

The pulsed laser can be described by Dirac comb of period T:

$$\mathrm{comb}_T(t) = \frac{1}{T}\sum_{n=-\infty}^{\infty} \exp\left(2i\pi nt/T\right), \tag{7.1}$$

and its width τ is well represented by a rectangle function

$$\mathrm{rect}_\tau = \begin{cases} 1, & \text{if } |t| < \tau/2 \\ 0, & \text{otherwise} \end{cases}. \tag{7.2}$$

Therefore, the optical force due to absorption can be defined as[†]:

$$F_{\mathrm{opt}}(t) = F_p\,\mathrm{rect}_\tau(t) * \mathrm{comb}_T(t), \tag{7.3}$$

being

$$F_p = N_{\mathrm{ppp}}\frac{\hbar k}{\tau} = N_{\mathrm{ppp}}\frac{h}{\lambda\tau} = \frac{T}{\tau}\frac{P_{\mathrm{mean}}}{c}, \tag{7.4}$$

[†] Here, $*$ represents the convolution product $(f * g)(x) = \int_{-\infty}^{+\infty} f(x-t)g(t)dt$.

the amplitude of the force. On the other hand, considering a perfectly reflecting surface, the highest force achievable is double the absorbed force.

In order to have a comparative measurement during colloid excitation, a modulation in trapping beam position, Δx_{eq}, was also performed at frequency f_m, as described in Sec. 3.1.3. The resulting force is given by:

$$F_{\text{mod}}(t) = F_m \sin(2\pi f_m t) \tag{7.5}$$

where $F_m = \kappa \Delta x_{eq}$ is the amplitude of the force and κ is the trap stiffness of the optical potential.

Considering a trapped particle immersed in water, its dynamics can be described by the modified Langevin equation (Eq. 2.18). However, due to optical forces from the absorption, F_{opt}, and the modulation force, F_{mod}, then

$$m_p \ddot{x}(t) = -\kappa x(t) - \int_{-\infty}^{\infty} dt' \gamma(t-t') \dot{x}(t') + F_{\text{th}}(t) + F_{\text{mod}}(t) + F_{\text{opt}}(t). \tag{7.6}$$

For a measured time T_{exp} of the particle position, PSD can be estimated by

$$\text{PSD}(f) = \frac{< |\tilde{x}_{T_{\text{exp}}}(f)|^2 >}{T_{\text{exp}}}, \tag{7.7}$$

as discussed in Sec. 3.2.4. Besides its importance for optical potential calibration, the particle's response due to external forces can be estimated using that quantity, which measures the way the power of a signal is distributed across different frequencies.

Computing the Fourier transform of Eq. 7.6, the resulting one-sided spectrum is given by

$$\begin{aligned} \text{PSD}^{exp}(f) &= 4|\chi(f)|^2 k_B T \text{Re}\left(\tilde{\gamma}(f)\right) \\ &+ T_{\text{exp}} \frac{F_m^2}{2} |\chi(f_m)|^2 \mathbf{1}_{I(f_e)}(f) \\ &+ T_{\text{exp}} \frac{2F_p^2 \tau^2}{T^2} \sum_{n=0}^{+\infty} |\chi(f_n)|^2 sinc_\pi^2(n f_n) \mathbf{1}_{I(f_m)}(f). \end{aligned} \tag{7.8}$$

with

$$\mathbf{1}_{I(f_0)}(f) = \begin{cases} 1, & \text{if } f \in I(f_0) = [f_0 - 1/(2T_{exp}), f_0 + 1/(2T_{exp})] \\ 0, & \text{otherwise} \end{cases}. \tag{7.9}$$

The first term is a consequence of stochastic force due to the contact with the bath at temperature T, the second term results from the modulation of the equilibrium position of the trap, and the third originates from the optical force due to excitation. The theoretical analysis was developed by Benjamin Besga and is detailed in the Appendix C.

To make the link with the experimental data, one can integrate Eq. 7.8 from $-\infty$ to ∞ to end with the power spectrum in meters squared. Thus, the modulation has the computing force:

$$\int_{-\infty}^{\infty} d\omega T_{\text{exp}} \frac{F_m^2}{2} |\chi(f_m)|^2 \mathbf{1}_{I(f_m)} = \frac{F_m^2}{2} |\chi(f_m)|^2, \tag{7.10}$$

since $\int_{-\infty}^{\infty} d\omega \mathbf{1}_{I(f_m)} = 1/T_{exp}$, and the excitation:

$$\int_{-\infty}^{\infty} d\omega T_{\text{exp}} \frac{2F_p^2 \tau^2}{T^2} |\chi(f_n)|^2 sinc_{\pi}^2(nf_n) \mathbf{1}_{I(f_n)} = \frac{2F_p^2 \tau^2}{T^2} |\chi(f_m)|^2 \leq 2\frac{P_{\text{mean}}^2}{c^2} |\chi(f_m)|^2. \tag{7.11}$$

7.3 Experimental system and sample preparation

Towards taking advantage of the quantum properties of those super-crystals, a new laser source was added to the experiment (presented in Sec. 3.1.2), a red-pulsed laser of 640 nm wavelength (Thorlabs NPL64B), as shown in Fig. 51. This laser allows us to control the pulse duration within the range of 5 ± 1 ns to 39 ± 3 ns, and by using the trigger, we can modulate it with arbitrary frequencies[‡].

A set of optical densities (ODs) was aligned in the laser's output to control the beam's intensity. The fine-tuning was conducted through the addition of a polarizer with a controllable rotational angle around the propagation axis.

To increase the spot of the pulsed laser in the trapping plane and cover the entire super-crystal region, one also incorporated a high focal length lens to diverge the beam in the objective's entrance. Basically, a non-collimated beam has a focal position in z that is different from a collimated one, which is closer to the objective output for convergent beams and more distant for divergent ones. Therefore, in the position where the particle is trapped with the IR laser (that enters collimated), the diameter of the exciting beam will be larger than its focal waist. This allowed us to increase the diameter of the spot from 3 μm to approximately 7 μm while using a 400 mm lens.

It is worth mentioning that the trapping and detection lasers are aligned to be as coaxial as possible in the sample region. However, the excitation beam is slightly misaligned in the objective's entrance, intentionally creating a small angular deviation in relation to the others, as shown (inset) in Fig. 51. Such a choice was made since it is expected to have a bigger effect on the bead's movement due to absorption in the beam propagation direction. However, our experimental system is not built to properly acquire particle movement in z. Therefore, creating a small angular deviation in the exciting beam allowed that part of the effect manifests in the $x - y$ plan.

For this, after a rough initial alignment of the pulsed laser in the path, a super-crystal is trapped and the beam is moved to illuminate the bead's area. The angular deviation can be visualized by scattering the pulsed light in the glass plate with the aid of the CCD camera.

[‡] A function generator was used to create the square wave to trigger the laser.

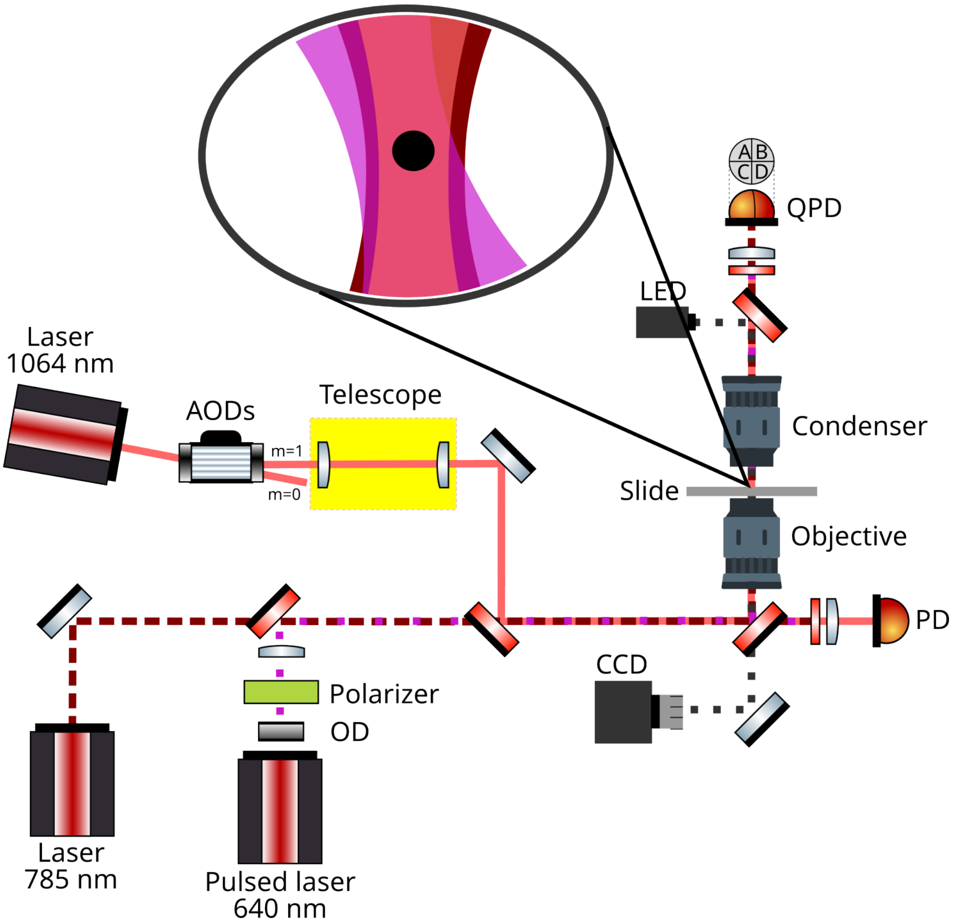

Figure 51 – Simplified description of the experimental setup described in Sec. 3.1.2, with the addition of the 640nm pulsed laser. A high focal length lens increases the beam's diameter in the trapping position and a set of ODs and one polarizer control the pulsed laser power. The inset shows the scheme of the beams' alignment after the objective with the trapping laser in orange, the probe laser in dark red, and the excitation laser in fuchsia.

Source: By the author.

Since the sample exhibits a highly diverse size distribution and our target is bigger particles to decrease the effect of pushing (due to the radiation pressure and mostly absorption), trapping the colloid more stably, the larger particles of the sample are separated. The process involves several steps, including centrifugation and sedimentation, for the removal of the lighter particles from the sample. After a substantial dilution so that only one particle can be found in an area of approximately hundreds of squared micrometres, one bead of the size of the order of micrometers is manually selected. For each particle, the size must be estimated and the optical trap must be characterized, as discussed in the next section.

7.4 Characterization of the optical trap

Since super-crystal colloids have different possible sizes, calculating the particle radius is the first step. For that, we employ a procedure involving binarizing the image of the chosen bead close to its focus and analyzing its contours, as demonstrated in Fig. 52. Using the minimum enclosing circle function and prior camera calibration, the diameter of each colloid can be estimated.

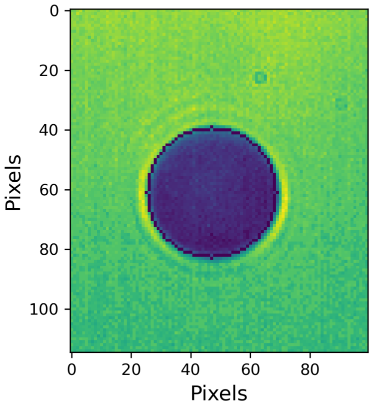

Figure 52 – Image of the microscopic super-crystal formed by SQWs and its contour. The resulting radius is approximately 2.4 μm.
Source: By the author.

To determine the trap stiffness of the bead, $\kappa_{x,y}$, and the amplification factor of the QPD, $S_{x,y}$, the PSD analysis method described in Sec. 3.2.4 was employed. The PSD curves (right) for x and y axis and the position histograms (left) of the same trajectories are depicted in Fig. 53.

During the experiments reported in this chapter (more specifically in the following section), approximately fifty position time series with 100 s each were acquired at 100 kHz. The mean trap stiffness is $\kappa_x = 1.58 \pm 0.02$ pN/μm for x direction and $\kappa_y = 1.52 \pm 0.04$ pN/μm for y direction; and the mean amplification factor results are $S_x = 4.60 \pm 0.16$ V/μm and $S_y = 3.61 \pm 0.13$ V/μm. Therefore, stable trapping with no changes in the optical potential is achieved during long measurement acquisitions.

To compute the expected modulation force, it is also necessary to characterize the beam's displacement during the modulation. The same method presented in Sec. 3.1.3 was applied for a trapped super-crystal, and the result is a calibration factor of 978 ± 7 nm/MHz.

7.5 Experimental Results

The pulsed laser is tuned in a given excitation frequency f_e and the modulation frequency is chosen to be close to the excitation one, $f_m = f_e - 10$ Hz so that the particle's response can be computed. In all measurements, the deviation in the equilibrium position is $\Delta y_{eq} = 195 \pm 2$ nm in the y direction. Therefore, the following analyses are conducted on that axis.

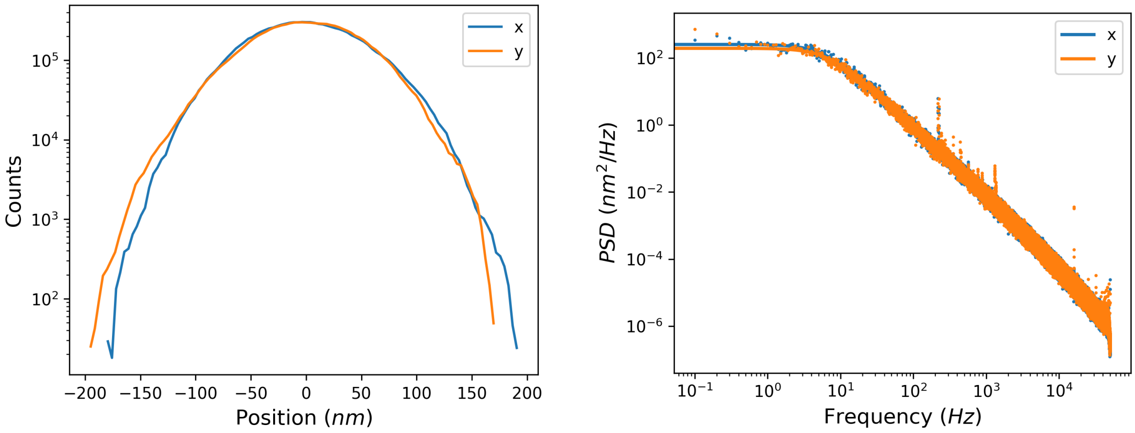

Figure 53 – Position histogram (left) and PSD (right) for x and y directions. The trap stiffnesses are $\kappa_x = 1.5$ pN/μm and $\kappa_y = 1.6$ pN/μm. Results from measurements of the time series position of a trapped particle with 2.4 μm radius for $t = 100$ s with a $f = 100$ kHz acquisition rate.
Source: By the author.

As an example, Fig. 53 (right) displays the complete spectra of a super-crystal trapped when $f_e = 16.1$ kHz and $f_m = 16.09$ kHz and Fig. 54 (left) shows a zoom in the window of interest, where the responses due to modulation and excitation are displayed as peaks in the spectra[§]. Towards estimating the frequency of the resulting peaks, first, PSD is zoomed into a sufficiently small interval, such that the Brownian noise is approximately constant, $f_e - 100$ Hz $< f < f_e + 100$ Hz. Then, the frequency corresponding to the maximum PSD value is obtained looking into an even smaller interval, $f_e - 5$ Hz $< f < f_e + 5$ Hz for the excitation and $f_m - 5$ Hz $< f < f_m + 5$ Hz for the modulation. Additionally, the thermal noise, $\langle F_{th}^2 \rangle$, is acquired by averaging the points out of the regions containing the peaks.

Since the peaks can be considerably sharp, longer measurements (100 s) were performed towards a bigger frequency resolution. The discrete integral was computed at $f = f_k \Delta f$ frequency, where $\Delta f = f_s / N_{FFT}$, f_s is the sampling frequency, and N_{FFT} is the length of the Fast Fourier Transform (FFT), as follows:

$$I = \int_{f-\delta f}^{f+\delta f} (PSD_k - \langle F_{th}^2 \rangle)\, df' = \Delta f \sum_{k=-k_i}^{k=k_i} PSD_k - \langle F_{th}^2 \rangle. \tag{7.12}$$

Here, the window $\delta f = (k - k_i)\Delta f \approx 0.2$ Hz is small enough to compute the contributions of excitation and modulation, and the thermal noise is subtracted, as shown in Fig. 54 (right). The image shows the frequency range used in the integration for both contributions around the frequency of excitation and the frequency of modulation. The peaks have a shift around 0.15 Hz from the expected (input frequency) due to the accuracy of the generator.

[§] The peaks are negligible in x direction due to the chosen pulsed laser alignment and are not shown here.

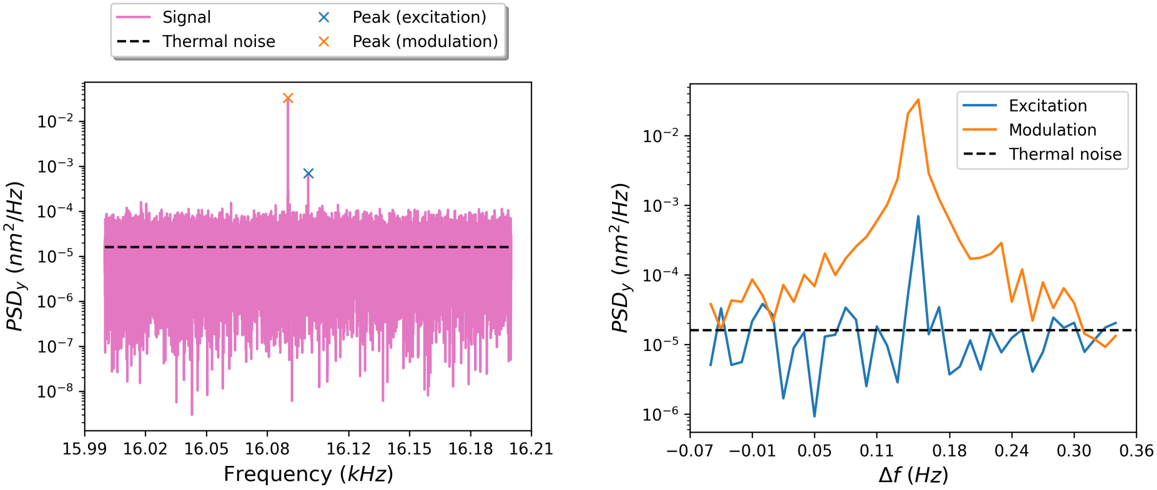

Figure 54 – PSD in y direction. First, the region $f_e - 100$ Hz $< f < f_e + 100$ Hz is zoomed to obtain the peaks and the thermal noise (left). The peaks region is then zoomed in the frequency range used in the integration, I (Eq. 7.12), around the frequency of excitation in blue, $f_e = 16.1$ kHz, and frequency of modulation in orange, $f_m = 16.09$ kHz. The black dashed line represents the thermal noise, $\langle F_{th}^2 \rangle$. Here, the pulsed laser operates at a 16.1 kHz frequency (excitation) and the trapping laser position is controlled at a 16.09 kHz frequency (modulation). Data were collected at 100 kHz for 100 s and $N_{FFT} = 10^7$.

Source: By the author.

The force of each contribution is given by

$$F = \sqrt{2\frac{I}{|\chi|^2}}, \tag{7.13}$$

where I is shown in Eq. 7.12 and χ is presented in Eq. 2.20, as described in the Appendix C. Therefore, the force can be estimated from experimental data and compared with theoretical predictions depicted in Eq. 7.10 for modulation and Eq. 7.11 for excitation.

To extract the type of dependency in each explored curve, we consider the *loglog* scale of optical force *versus* average power. The resulting angular coefficient is equivalent to the degree α. For $\alpha = 0$, the dependency is constant; for $\alpha = 1$, the behaviour is linear; for $\alpha = 2$ is quadratic etc.

Since the beam's displacement is kept the same, the modulation force should be constant in all measurements, i.e. $\alpha_{theo} = 0$. However, as presented in Eq. 7.11, the optical force has a linear dependency on the average power of the pulsed laser, i.e. $\alpha_{theo} = 1$. Experimentally, P_{mean} can be controlled by changing the frequency $f_e = 1/T$, the width τ or the rotation angle of the polarizer[¶] and the Langevin dynamics depends only on the average power regardless of $1/T$, τ or peak power. Figs. 55, 56, and 57 display a comparison between theoretical and experimental results for different parameters of the exciting beam.

[¶] The calibration curve for the frequency control is $P_{mean} = 0.131f + 0.033$, and for the width control is $P_{mean} = 0.060\tau + 0.04$. Here, the average power is in microwatts, the frequency is in kilohertz, and the width is in nanoseconds.

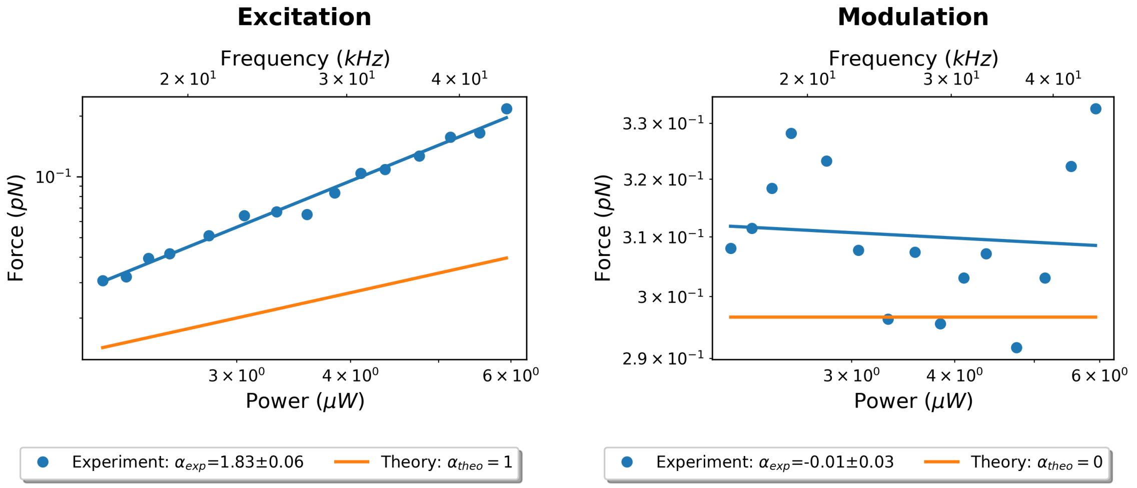

Figure 55 – Frequency control. Average power dependency of optical force (left) and modulation force (right) from $f_e = 16.1$ kHz to 45.1 kHz and $f_m = f_e - 10$ Hz. Experimental values (dots) and linear fit on *loglog* scale (solid lines) in blue and theoretical predictions in orange.

Source: By the author.

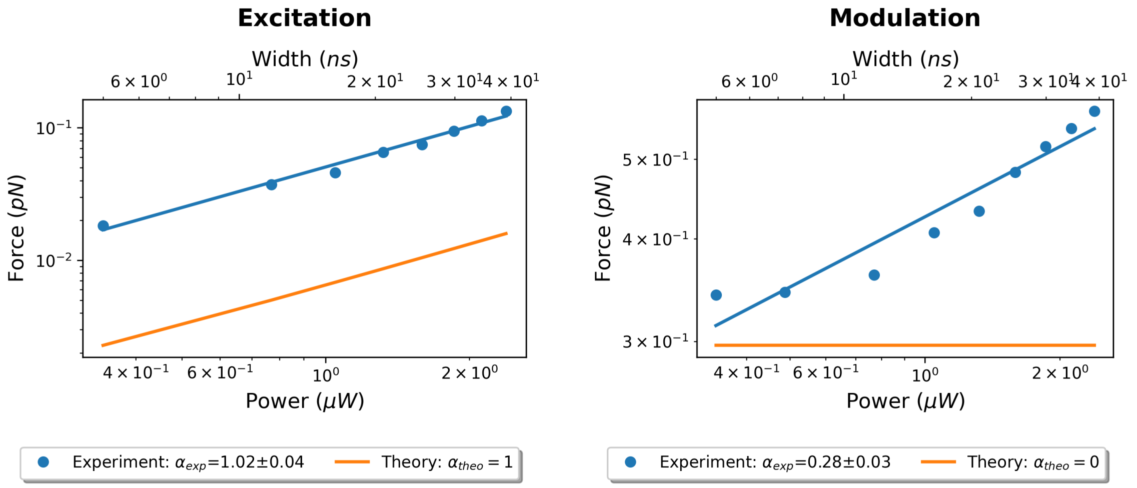

Figure 56 – Width control. Average power dependency of optical force (left) and modulation force (right) from $\tau = 5$ ns to 39 ns. Experimental values (dots) and linear fit on *loglog* scale (solid lines) in blue and theoretical predictions in orange.

Source: By the author.

For all the cases, the obtained amplitude of the modulation force is close to the theoretical prediction $F_m = 0.30$ pN, as shown in Figs 55, 56, and 57 (right). However, the value of α_{exp} deviates from the case of width control, showing a subtle growth of the particle response over time ($\alpha_{exp} = 0.28 \pm 0.03$).

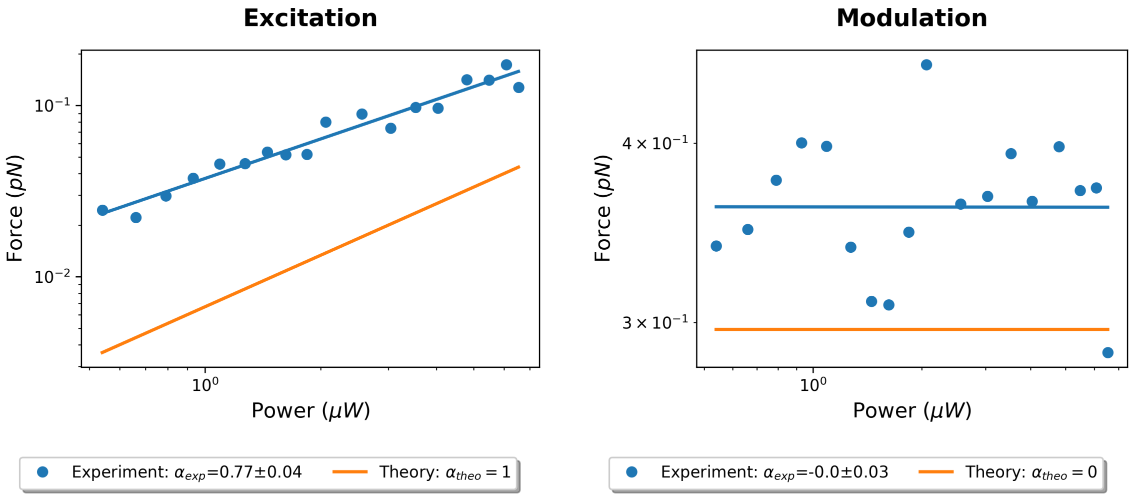

Figure 57 – Polarizer control. Average power dependency of optical force (left) and modulation force (right) for different polarizer's angular positions. Experimental values (dots) and linear fit on *loglog* scale (solid lines) in blue and theoretical predictions in orange.

Source: By the author.

Interestingly, the optical force computed from experimental data is considerably bigger than the expected value, even with the extrapolation that all photons are absorbed and the force is applied in the measured direction y. Moreover, according to Fig. 55 (left), the optical force has almost a quadratic dependency on the average power ($\alpha_{exp} = 1.83 \pm 0.06$). For the width control, shown in Fig. 56 (left), the experimental degree is close to the theoretical one, although a magnitude $F_{exp} \approx 7.5 F_{theo}$ is observed. Regarding the power dependency directly controlled by the polarizer's angular position, shown in Fig. 57 (left), again, the amplitude is larger; however, the dependency is smaller than the expected ($\alpha_{exp} = 0.77 \pm 0.04$).

Therefore, the theoretical underestimation of the resulting optical force shows that the physical model based on Langevin dynamics must be revised to better describe the particle's motion. Although the amplitude of the experimental force is considerably larger than expected, no explanation could be inferred for the average power dependencies discrepancies α_{exp} while different pulsed laser parameters were being changed. Indeed we expect the same dependency with the mean power regardless of frequency, pulse width or pulse power using this Langevin description (see Eq. 7.11).

7.6 Conclusions

This last chapter proposed extending studies, initially focused on a classical description, to investigate the validity of stochastic thermodynamics at the classical-quantum interface. To achieve this, the super-crystals formed by quantum dots were trapped with optical tweezers, and the effects of an external pulsed excitation source on their mechanical dynamics were explored. In addition to the optical force, a modulation in the beam position was also applied for complementary measurements.

The trajectory of the trapped bead was used for the computation of the Power Spectral Density (PSD), revealing resonant peaks at the expected frequencies. Therefore, the experimental optical and modulation forces for various pulsed laser parameters were calculated from those curves. In particular, one focused on studying the bead's response while altering the excitation source's average power. Such a control was performed by controlling the polarizer's angular position and adjusting the pulsed laser's frequency and width.

As a complementary measurement, a modulation in the beam position was applied with a constant trapping beam displacement throughout the experiment. In this case, the resulting force should remain constant and close to its theoretical prediction for all measurements. The experimental results showed a good agreement with the theory, with minor deviations while controlling the width of the pulsed laser possibly attributed to trapping instabilities.

However, the resulting magnitudes of the optical forces notably surpassed the theoretical predictions. It is worth noting that the model adopted assumed an extreme scenario where all particles were absorbed, resulting in recoil along the measured axis. Since measurements were not performed along the laser propagation direction, z, only the projection of that effect in the y direction was taken into account, suggesting the discrepancies are even larger. Regarding the dependency of force on average power, several α values were obtained, although the theory expects linear growth. Further investigations on both theory and experiment must be conducted to elucidate the resulting particle behavior.

Therefore, the first important result is absorption/emission phenomena can be mechanically measured with the use of adapted optical tweezers at room temperature. Although the position in the z direction could not be tracked for our experimental configuration, the effects on the plan $x - y$ were strong enough to be detected. Furthermore, our most significant finding is that the particle dynamics differ from what is expected by the Langevin description, implying the model must be improved to incorporate previously unconsidered phenomena.

Besides the possible gaps in the theoretical description, our results can deviate from the expected due to some experimental complexities. Challenges include maintaining a stable trap, given the non-homogeneous nature of the particle compared to the commercial ones, a slight misalignment in the position of the beam when the polarizer angle is varied, and difficulty in avoiding potential photodegradation of the colloid (116). Despite adjusting the pulsed laser power to minimize possible undesired effects, they do not vanish and can affect the results.

One possibility is that absorption is insufficient to explain the experimental results, and collective effects, such as superradiance, are the primary drivers of the observed recoil in the colloid. Furthermore, due to the temporally localized excitation, the particle is subjected to impulses in a very short time duration, and the viscosity behavior in this regime may deviate significantly from the typical predictions of Langevin dynamics (117). When rapid pulses are applied to a Brownian particle, the effective viscosity can be temporarily reduced, resulting in a bigger displacement due to the particle's rapid response to external changes, masking the influence of the fluid viscosity in which the particle is immersed. Such an effect may explain the difference between the absolute values predicted for the optical force and those experimentally verified.

Overall, these results have triggered new experiments performed in Lyon in order to minimize the undesired effects and pave the way for a series of experiments exploring the classical-quantum interface, such as understanding possible collective effects in these structures, developing hydrodynamics studies at short time, and investigating the extension of stochastic thermodynamics in this regime.

8 THESIS EVOLUTION AND CONCLUSIONS

In summary, this doctoral thesis comprehended experimental studies on stochastic thermodynamics as its primary scope. The first steps involved building and characterizing a homemade experimental system, which progressed to the application of the first protocols in the classical regime. Then, through collaboration, efforts were made to explore thermodynamics in the classical-quantum interface. This section reports the advances and challenges encountered during the elaboration of the thesis, chronologically, as well as the main results and possible future studies.

The assembly of the optical tweezers apparatus in the IFSC-USP laboratory began in 2017 - more details can be found in the author´s Master's dissertation (63). Despite the existence of a functional optical tweezer setup capable of trapping and manipulating micro-particles, the first step towards nanothermodynamics was the implementation of the QPD device for tracking the bead position at a higher acquisition frequency than that of the camera used up to that point. Its inclusion enabled characterizing the system through different methods, as described in Chapter 3, and started a series of experiments described in what follows.

The first project aimed to explore time-averaged optical potentials, particularly creating double-well traps by switching the laser between two nearby positions. The motivation stemmed from its various applications, such as Kramers' theory and Landauer's principle (24–25), making this type of double-well optical potential a good starting point. The first experimental tests led to the creation of multiple traps and the initial results are provided in (65). Despite good control of the beam's position, the condition for bistable operation (Krammer's transitions) could not be easily achieved; therefore, the research path was eventually changed.

It is important to mention that the world faced the coronavirus pandemic during that period. Consequently, laboratory activities were suspended for many months, and returning to normality took years. In this scenario, we started exploring stochastic thermodynamics using harmonic potentials. This decision was further reinforced by the fact that one of the fundamental works of optimization of processes in nonequilibrium regime (74), focusing on Brownian particles trapped in harmonic potentials, apparently needed to be tested experimentally. The work developed by Schimield and Seifert proposed analytical solutions for two study cases: changing the trap's equilibrium position and the force constant. Still under the lockdown imposed by the pandemic, those optimal protocols started to be explored computationally by adapting the simulations presented in (82) in collaboration with Lucas Kamizaki, a Master's student in our lab (69, 80, 83).

According to the simulations and considering the characteristics of our experimental apparatus, we concluded that it would be simpler to experimentally start with the compressing trap protocol, in which the bead is equilibrated in an initial confinement state and the protocol is then applied by increasing the trapping laser intensity. The first experimental applications of compressing protocols were conducted in the setup when in-person activities were resumed. Jarzynski's equality was used as an independent test for the calibrations and in addition to verifying it, the results for the optimal protocols were compared with those from linear (suboptimal) ones. The first findings are provided in (83).

Overall, the average work obtained for optimal control was lower in comparison to the linear case for all explored sets of parameters and Jarzynski's equality was also verified. However, due to mechanical resonances, our system had significant low-frequency noise, around 30 Hz, requiring post-acquisition data processing with a digital notch filter centered at the noise resonance. We also suspected a possible heating effect of the water (reservoir) near the laser focus (118) during the protocols (at larger laser intensities), since a 980 nm laser near a significant absorption line of water molecules was used.

Around that time, a collaboration with a well-established laboratory at ENS-Lyon, which has produced many pioneering experiments in stochastic thermodynamics, started. During the research stage in Lyon, the optimal protocols continued to be tested in conjunction with the development of the main project proposed for the exchange period (involving quantum dots). The experiments were repeated for a more extensive set of parameters, and expansion protocols were applied to test Crook's relation.

A comprehensive study on linear protocols is provided in Chapter 4, showing the experimental methodology and the resulting energetics distributions for thousands of trajectories. The set of chosen parameters includes different switching times and modulation amplitudes. The mean values of work, heat, and internal energy difference were obtained, enabling verification of the First Law of Thermodynamics and comparison with their theoretical predictions. It was verified that the mean values for heat and work converged to the free energy difference value for slower protocols, as expected by Clausius' theorem (Second Law of Thermodynamics), and the variance went to zero. Jarzynski's equality was verified for compressing protocols and due to the difficulty in obtaining those results for expansion cases, Crooks's theorem was also tested.

Although consistent with the theory, minor deviations were observed for protocols when greater modulation amplitudes were applied during longer protocol times. The origin of such uncertainty lies in the imprecision of the amplification factor calibration, which is responsible for converting the tracking signal from volts to meters. Due to the radiation pressure change as the trapping beam power is modulated, the particle is expected to move in the beam propagation axis. Even a small displacement can subtly change the

QPD response in x and y axes, and modelling its behavior can be complex.

Concerning optimal protocols, data were collected jointly with linear ones to keep the same trapped particle in both processes. The results are provided in Chapter 5 and show that optimal protocols have lower average work than the linear case, and the experimental values are consistent with the expected theoretical ones. Besides, the difference between optimal and suboptimal cases depends on the protocol time and an increase in the optimization efficiency can be observed for intermediate durations. Since in the limit in which the protocol time tends to zero, i.e., the step protocol, the work depends only on the initial value $\langle x(0)^2 \rangle$, and for more extended protocols, the average work converges to the free energy difference, in the intermediate zones it is visible a bigger difference between linear and optimal protocols. Complementarly, the Jarzynski equality was also verified for the work distributions obtained from optimal processes, since this result depends only on the initial and final states regardless of the particle's path in the phase space.

Since the moving trap case could not be experimentally tested during the available time, the simulation results are also provided towards guiding future experiments. Due to the significant contributions of rare events in the Jarzysnki equation when negative work values are expected, a very large number of trajectories must be collected. Additionally, the optimal protocols clearly showed lower average work than linear ones, as expected, and again, a higher efficiency was observed for intermediate protocol times.

In recent years, process optimization across different platforms has drawn significant attention. Therefore, our findings are expected to contribute to both the understanding of the energetics of nonequilibrium finite-time processes in small systems and future developments in the field, especially for general (non-harmonic) trapping potentials. Upcoming experiments in our group will continue exploring optimal control in different optical potentials, including those for which no analytical solutions are available (77, 78, 80).

Concomitantly with studies of classical tasks in silica micro-particles, initial investigations aiming at the quantum regime were explored in the setup of ENS-Lyon. More specifically, the aim was to study the coupling between optical and mechanical properties of optically active particles within a trap. Despite the target particles being super-crystals of quantum dots, the first steps were taken using silica beads to make the needed experimental changes and calibrations for the study.

Initially, detection and excitation lasers were added to the optical path, and the first tests with silica beads were performed. Interestingly, although a clear response was observed in the power spectrum density when the trapping beam position was modulated, no recoil due to excitation was verified. This result shows that the contributions due to the excitation laser's scattering were negligible compared to thermal noise, since no absorption effects of silica at the wavelength of the pulsed laser were expected. After those initial tests, the first super-crystals of quantum dots were trapped.

Due to the considerable contribution of absorption and radiation pressure in those particles, experiments with microscopic (larger) colloids were performed and a small trapping laser's intensity was chosen towards a more stable trap. Surprisingly, the particle's response from the excitation was easily observed from the first measurement and was very high in the PSD, with peaks much larger than the thermal noise. However, after some excitation time, the colloids began to show significant instability and their physical shape was altered. The quantum dots were possibly undergoing bleaching and the pulsed laser intensity was then reduced for minimizing such an undesired effect.

From that point on, the particle was fully characterized and its behavior was studied regarding various excitation beam parameters, such as controlling width, frequency, and power. The results are provided in Chapter 7. Essentially, the expected optical force arising from the absorption effect depends primarily on the average power of the pulsed laser, and a linear dependence is anticipated. Experimental findings showed that the computed optical force dependence on the average power varies in function of the controlled parameter (frequency, width or direct power), requiring further theoretical investigation to understand the behavior of the experimental results.

However, it is evident that the amplitude of the force obtained is significantly greater than theoretically expected, even considering an extreme scenario where all photons are absorbed, producing the bead's recoil in the beam propagation direction. A possible explanation for such discrepancies is the existence of collective phenomena in the quantum dots composing the colloid, especially the presence of the superradiance effect. Additionally, the hydrodynamics model may differ due to the short time duration of the optical force. If viscosity vanishes in that limit, a more significant response in the bead's movement is expected in the colloid, explaining the resulting experimental forces. These findings are preliminary observations and further experiments are necessary for confirming the predictions. Nevertheless, they can contribute to future developments in collective effects at room temperature and open doors for new investigations into the extension of stochastic thermodynamics in the quantum limit.

After the exchange period, pertinent changes were implemented in our experimental system at IFSC-USP to improve the apparatus' noise behavior. Firstly, the components were rearranged to decrease their height on the optical table, which was enough to make the low-frequency noise disappear. The trapping laser was also replaced with a more stable 1064 nm laser. However, as discussed in Appendix B, significant high-frequency noises remained in the system despite the attempts to remove them (e.g., working at different probe laser intensities, performing changes to the QPD amplification circuit, replacing power supplies, among others). Therefore, a low-pass filter was implemented in the acquired data to reduce noise at high frequencies.

The procedure enabled characterizing the optical tweezers and the behavior of the results was very close to that described in Chapter 3 for the calibration curves. However, high-frequency noise becomes a significant difficulty for delicate experiments like those in stochastic thermodynamics studies. Therefore, compressing and expanding protocols were reapplied to test the system's reliability. Experimental results were compared with the theoretical predictions for the average work of linear and optimal protocols and the test of Jarzynski's equality, revealing a good agreement between experiment and theory for short protocols (with protocol times around tenths of the relaxation time). On the other hand, for longer ones, the filtering procedure was insufficient to eliminate deviations, and the remaining noise contributed to the apparent displacement of the particle, which overestimated the average work. Therefore, removing high-frequency noise from the acquired signals by changing the electronics or developing better data processing is one of the current challenges to overcome for the exploration of more complex experiments.

Finally, despite dealing with the undesired noise, one of the group's main interests was to explore the information-to-energy conversion. From an idea proposed in the Master's dissertation of Lucas Kamizaki (69) and inspired by the previous work (28), a first attempt to apply Maxwell's demon was made with the use of the available system. This simple experiment proposed changing the trap force constant in a step protocol by using the information about the particle's position. Its implementation with results is discussed in Chapter 6.

Exploring work distributions for thousands of trajectories revealed significant differences between protocols with and without feedback. Due to information-to-energy conversion, the feedback increases the energetic efficiency and the resulting mean average work is proportional to the threshold applied, i.e., the region where the particle must be detected for the step protocol to be triggered. Moreover, as expected, Jarzynski's generalized equality showed a degree of control of the system inversely proportional to the threshold chosen. In the near future, the next step is to implement dedicated (fast-response) hardware to decrease the delay time in the experiment and target more complex experiments.

In conclusion, this thesis addressed the development and challenges of studies of stochastic thermodynamics in optical tweezers from classical to quantum regime. These findings can contribute to further explorations of small systems and indicate a broad open path with several exciting avenues yet to be explored.

REFERENCES

1 ZEMANSKY, M. W. **Heat and thermodynamics**: an intermediate textbook for students of physics, chemistry, and engineering. 3rd ed. New York: McGraw-Hill, 1951.

2 CALLEN, H. B. **Thermodynamics and an introduction to thermostatistics**. New York: Wiley, 1998.

3 KONDEPUDI, D.; PRIGOGINE, I. **Modern thermodynamics**: from heat engines to dissipative structures. 2nd ed. New York: John Wiley, 2015.

4 ALTANER, B. Nonequilibrium thermodynamics and information theory: basic concepts and relaxing dynamics. **Journal of Physics A**, v. 50, n. 45, p. 454001, 2017. DOI: 10.1088/1751-8121/aa841d.

5 RITORT, F. Nonequilibrium fluctuations in small systems: from physics to biology. **Advances in Chemical Physics**, Wiley Online Library, v. 137, p. 31, 2008.

6 SEIFERT, U. Stochastic thermodynamics, fluctuation theorems and molecular machines. **Reports on Progress in Physics**, v. 75, n. 12, p. 126001, 2012. DOI: 10.1088/0034-4885/75/12/126001.

7 SCHUSTER, H. G. **Nonequilibrium statistical physics of small systems**: fluctuation relations and beyond. New York: John Wiley, 2013. DOI:10.1002/978352765870.

8 JONES, P. H.; MARAGÒ, O. M.; VOLPE, G. **Optical tweezers**: principles and applications. Cambridge: Cambridge University Press, 2015.

9 GIESELER, J. *et al.* Optical tweezers—from calibration to applications: a tutorial. **Advances in Optics and Photonics**, Optica Publishing Group, v. 13, n. 1, p. 74–241, 2021.

10 EVANGELISTA, L. R. **Perspectivas em história da física**: da física dos gases à mecânica estatística. São Paulo: Editora Livraria da Física, 2014.

11 VAN WYLEN, G.; SONNTAG, R.; BORGNAKKE, C. **Fundamentals of classical thermodynamics**. New York: Wiley, 1993.

12 CLAUSIUS, R. Über eine veränderte form des zweiten hauptsatzes der mechanischen wärmetheorie. **Annalen der Physik**, v. 169, n. 12, p. 481–506, 1854.

13 GAVRILOV, M. **Experiments on the thermodynamics of information processing**. New York: Springer, 2017.

14 JARZYNSKI, C. Nonequilibrium equality for free energy differences. **Physical Review Letters**, v. 78, n. 14, p. 2690, 1997.

15 CHANDLER, D. **Introduction to modern statistical mechanics**. Oxford: Oxford University Press, 1987.

16 CROOKS, G. E. Entropy production fluctuation theorem and the nonequilibrium work relation for free energy differences. **Physical Review E**, v. 60, n. 3, p. 2721, 1999. DOI: 10.1103/PhysRevE.60.2721.

17 BUSTAMANTE, C.; LIPHARDT, J.; RITORT, F. The nonequilibrium thermodynamics of small systems. **Physics Today**, v. 58, n. 7, p. 43–48, 2005.

18 SEIFERT, U. Stochastic thermodynamics: principles and perspectives. **European Physical Journal B**, v. 64, n. 3, p. 423–431, 2008.

19 CILIBERTO, S. Experiments in stochastic thermodynamics: short history and perspectives. **Physical Review X**, v. 7, n. 2, p. 021051, 2017. DOI: org/10.1103/PhysRevX.7.021051.

20 KOSKI, J. V. *et al.* Experimental observation of the role of mutual information in the nonequilibrium dynamics of a maxwell demon. **Physical Review Letters**, v. 113, n. 3, p. 030601, 2014. DOI:10.1103/PhysRevLett.113.030601.

21 CAMATI, P. A. *et al.* Experimental rectification of entropy production by maxwell's demon in a quantum system. **Physical Review Letters**, v. 117, n. 24, p. 240502, 2016. DOI: 10.1103/PhysRevLett.117.240502.

22 SAHA, T. K. *et al.* Maximizing power and velocity of an information engine. **Proceedings of the National Academy of Sciences**, v. 118, n. 20, 2021. DOI:10.1073/pnas.202335611.

23 KOSKI, J. V. *et al.* Experimental realization of a szilard engine with a single electron. **Proceedings of the National Academy of Sciences**, v. 111, n. 38, p. 13786–13789, 2014.

24 BÉRUT, A. *et al.* Experimental verification of landauer's principle linking information and thermodynamics. **Nature**, v. 483, n. 7388, p. 187–189, 2012.

25 JUN, Y.; GAVRILOV, M.; BECHHOEFER, J. High-precision test of landauer's principle in a feedback trap. **Physical Review Letters**, v. 113, n. 19, p. 190601, 2014. DOI:10.1103/PhysRevLett.113.190601.

26 YAN, L. *et al.* Single-atom demonstration of the quantum landauer principle. **Physical Review Letters**, v. 120, n. 21, p. 210601, 2018. DOI:10.1103/PhysRevLett.120.210601.

27 LIPHARDT, J. *et al.* Equilibrium information from nonequilibrium measurements in an experimental test of jarzynski's equality. **Science**, v. 296, n. 5574, p. 1832–1835, 2002.

28 TOYABE, S. *et al.* Experimental demonstration of information-to-energy conversion and validation of the generalized jarzynski equality. **Nature Physics**, v. 6, n. 12, p. 988–992, 2010.

29 HOANG, T. M. *et al.* Experimental test of the differential fluctuation theorem and a generalized jarzynski equality for arbitrary initial states. **Physical Review Letters**, v. 120, n. 8, p. 080602, 2018. DOI:10.1103/PhysRevLett.120.080602.

30 AN, S. *et al.* Experimental test of the quantum jarzynski equality with a trapped-ion system. **Nature Physics**, v. 11, n. 2, p. 193–199, 2015.

31 COLLIN, D. *et al.* Verification of the crooks fluctuation theorem and recovery of rna folding free energies. **Nature**, v. 437, n. 7056, p. 231–234, 2005.

32 TOUSSAINT, O.; SCHNEIDER, E. D. The thermodynamics and evolution of complexity in biological systems. **Comparative Biochemistry and Physiology A:** molecular & integrative physiology, v. 120, n. 1, p. 3–9, 1998.

33 ALTANER, B.; WACHTEL, A.; VOLLMER, J. Fluctuating currents in stochastic thermodynamics. ii. energy conversion and nonequilibrium response in kinesin models. **Physical Review E**, v. 92, n. 4, p. 042133, 2015. DOI:10.1103/PhysRevE.92.042133.

34 TANIGUCHI, Y. *et al.* Entropy rectifies the brownian steps of kinesin. **Nature Chemical Biology**, v. 1, n. 6, p. 342–347, 2005.

35 TOYABE, S.; MUNEYUKI, E. Single molecule thermodynamics of atp synthesis by f1-atpase. **New Journal of Physics**, v. 17, n. 1, p. 015008, 2015. DOI: 10.1088/1367-2630/17/1/015008.

36 MAST, C. B.; BRAUN, D. Thermal trap for dna replication. **Physical Review Letters**, v. 104, n. 18, p. 188102, 2010. . DOI:10.1103/PhysRevLett.104.188102.

37 POULTON, J. M.; OULDRIDGE, T. E. Edge-effects dominate copying thermodynamics forfinite-length molecular oligomers. **New Journal of Physics**, v. 23, p. 1–14, 2021. DOI: 10.1088/1367-2630/ac0389.

38 AUFFÈVES, A. A short story of quantum and information thermodynamics. **SciPost Physics Lecture Notes**, v. 27, p. 1–13, 2021. DOI:10.21468/SciPostPhysLectNotes.27.

39 BINDER, F. *et al.* Thermodynamics in the quantum regime. **Fundamental Theories of Physics**, v. 195, p. 1–2, 2018.

40 VINJANAMPATHY, S.; ANDERS, J. Quantum thermodynamics. **Contemporary Physics**, v. 57, n. 4, p. 545–579, 2016.

41 MODAK, R. A simple model for the study of free brownian motion. **American Journal of Physics**, v. 52, n. 1, p. 43–46, 1984.

42 REICHL, L. E. **A modern course in statistical physics**. New York: John Wiley & Sons, 2016.

43 FRANOSCH, T. *et al.* Resonances arising from hydrodynamic memory in brownian motion. **Nature**, v. 478, n. 7367, p. 85–88, 2011.

44 SEKIMOTO, K. Langevin equation and thermodynamics. **Progress of Theoretical Physics Supplement**, v. 130, p. 17–27, 1998.

45 ASHKIN, A. *et al.* Force generation of organelle transport measured in vivo by an infrared laser trap. **Nature**, Nature Publishing Group UK London, v. 348, n. 6299, p. 346–348, 1990.

46 BLOCK, S. M.; GOLDSTEIN, L. S.; SCHNAPP, B. J. Bead movement by single kinesin molecules studied with optical tweezers. **Nature**, Nature Publishing Group UK London, v. 348, n. 6299, p. 348–352, 1990.

47 BUSTAMANTE, C. *et al.* Entropic elasticity of λ-phage dna. **Science**, American Association for the Advancement of Science, v. 265, n. 5178, p. 1599–1600, 1994.

48 FINER, J. T.; SIMMONS, R. M.; SPUDICH, J. A. Single myosin molecule mechanics: piconewton forces and nanometre steps. **Nature**, Nature Publishing Group UK London, v. 368, n. 6467, p. 113–119, 1994.

49 BUAJARERN, J. *et al.* Controlling and characterizing the coagulation of liquid aerosol droplets. **The Journal of Chemical Physics**, v. 125, n. 11, 2006.

50 MCCANN, L. I.; DYKMAN, M.; GOLDING, B. Thermally activated transitions in a bistable three-dimensional optical trap. **Nature**, v. 402, n. 6763, p. 785–787, 1999.

51 GRIER, D. G. A revolution in optical manipulation. **Nature**, Nature Publishing, v. 424, n. 6950, p. 810–816, 2003.

52 MARAGO, O. M. *et al.* Optical trapping and manipulation of nanostructures. **Nature Nanotechnology**, Nature, v. 8, n. 11, p. 807–819, 2013.

53 DHOLAKIA, K.; ČIŽMÁR, T. Shaping the future of manipulation. **Nature Photonics**, Nature, v. 5, n. 6, p. 335–342, 2011.

54 POLIMENO, P. *et al.* Optical tweezers and their applications. **Journal of Quantitative Spectroscopy and Radiative Transfer**, Elsevier, v. 218, p. 131–150, 2018.

55 JONÁŠ, A.; ZEMANEK, P. Light at work: The use of optical forces for particle manipulation, sorting, and analysis. **Electrophoresis**, Wiley Online Library, v. 29, n. 24, p. 4813–4851, 2008.

56 ASHKIN, A. Acceleration and trapping of particles by radiation pressure. **Physical Review Letters**, v. 24, n. 4, p. 156, 1970.

57 ASHKIN, A.; DZIEDZIC, J. Optical levitation by radiation pressure. **Applied Physics Letters**, v. 19, n. 8, p. 283–285, 1971.

58 ASHKIN, A. *et al.* Observation of a single-beam gradient force optical trap for dielectric particles. **Optics Letters**, v. 11, n. 5, p. 288–290, 1986.

59 NETO, P. M.; NUSSENZVEIG, H. Theory of optical tweezers. **Europhysics Letters**, v. 50, n. 5, p. 702, 2000.

60 NIEMINEN, T. A. *et al.* Physics of optical tweezers. **Methods in Cell Biology**, v. 82, p. 207–236, 2007.

61 RIBEZZI-CRIVELLARI, M.; HUGUET, J. M.; RITORT, F. Counter-propagating dual-trap optical tweezers based on linear momentum conservation. **Review of Scientific Instruments**, v. 84, n. 4, 2013.

62 HORST, A. Van der *et al.* High trapping forces for high-refractive index particles trapped in dynamic arrays of counterpropagating optical tweezers. **Applied Optics**, v. 47, n. 17, p. 3196–3202, 2008.

63 MARTINS, T. T. **Aprisionamento óptico de micropartículas e desenvolvimento de potenciais ópticos dinâmicos**. 2019. 161p. Dissertação (Mestrado) — Instituto de Física de São Carlos, Universidade de São Paulo, São Carlos, 2019.

64 CHANG, I. Acousto-optic devices and applications. **Handbook of optics**. New York: McGraw-Hill, 1995. v. 2. p. 12–1.

65 MARTINS, T. T.; MUNIZ, S. R. Dynamically controlled double-well optical potential for colloidal particles. *In*: : SBFOTON INTERNATIONAL OPTICS AN PHOTONICS CONFERENCE, 2021. São Carlos, SBFoton, 2021. p. 1–4. DOI:10.1109/SBFotonIOPC50774.2021.9461866.

66 WELCH, P. The use of fast fourier transform for the estimation of power spectra: a method based on time averaging over short, modified periodograms. **IEEE Transactions on Audio and Electroacoustics**, v. 15, n. 2, p. 70–73, 1967.

67 LUKIĆ, B. *et al.* Motion of a colloidal particle in an optical trap. **Physical Review E**, APS, v. 76, n. 1, p. 011112, 2007.

68 PIN, C. *et al.* Optical tweezing using tunable optical lattices along a few-mode silicon waveguide. **Lab on a Chip**, v. 18, n. 12, p. 1750–1757, 2018.

69 KAMIZAKI, L. P. **Studies of stochastic thermodynamics with optical tweezers** . 2022. 94p. Dissertação (Mestrado) — Instituto de Física de São Carlos, Universidade de São Paulo, 2022.

70 ROSALES-CABARA, Y. **Acting on a brownian probe:** from optical forces to optimal thermodynamic protocols. 2020. Tese (Doutorado) — Université de Strasbourg, Strasbourg, 2020.

71 MARTÍNEZ, I. A. *et al.* Colloidal heat engines: a review. **Soft Matter**, v. 13, n. 1, p. 22–36, 2017.

72 CLAUSIUS, R. On the treatment of differential equations which are not directly integrable. In: CLAUSIUS, R. (ed.) **The mechanical theory of heat, with its applications to the steam engine and to the physical properties of bodies.** London: Taylor and Francis, 1867. p. 1–13.

73 AURELL, E.; MEJÍA-MONASTERIO, C.; MURATORE-GINANNESCHI, P. Optimal protocols and optimal transport in stochastic thermodynamics. **Physical Review Letters**, APS, v. 106, n. 25, p. 250601, 2011.

74 SCHMIEDL, T.; SEIFERT, U. Optimal finite-time processes in stochastic thermodynamics. **Physical Review Letters**, v. 98, n. 10, p. 108301, 2007. DOI:10.1103/PhysRevLett.98.108301.

75 GOMEZ-MARIN, A.; SCHMIEDL, T.; SEIFERT, U. Optimal protocols for minimal work processes in underdamped stochastic thermodynamics. **The Journal of Chemical Physics**, v. 129, n. 2, p. 024114, 2008. DOI:10.1063/1.294894.

76 SCHMIEDL, T. *et al.* Optimal protocols for hamiltonian and schrödinger dynamics. **Journal of Statistical Mechanics:** theory and experiment, v. 2009, n. 07, p. P07013, 2009. DOI: 10.1088/1742-5468/2009/07/P07013.

77 BONANÇA, M. V.; DEFFNER, S. Minimal dissipation in processes far from equilibrium. **Physical Review E**, v. 98, n. 4, p. 042103, 2018. DOI:10.1103/PhysRevE.98.042103.

78 BONANÇA, M. V.; DEFFNER, S. Optimal driving of isothermal processes close to equilibrium. **The Journal of Chemical Physics**, v. 140, n. 24, p. 244119, 2014. DOI:10.1063/1.4885277.

79 LARGE, S. J.; SIVAK, D. A. Optimal discrete control: minimizing dissipation in discretely driven nonequilibrium systems. **Journal of Statistical Mechanics:** theory and experiment, v. 2019, n. 8, p. 083212, 2019. DOI 10.1088/1742-5468/ab342b.

80 KAMIZAKI, L. P.; BONANÇA, M. V.; MUNIZ, S. R. Performance of optimal linear-response processes in driven brownian motion far from equilibrium. **Physical Review E**, v. 106, n. 6, p. 064123, 2022. DOI:10.1103/PhysRevE.106.064123.

81 FOX, C. **An introduction to the calculus of variations**. New York: Courier Corporation, 1987.

82 VOLPE, G.; VOLPE, G. Simulation of a brownian particle in an optical trap. **American Journal of Physics**, v. 81, n. 3, 2013. DOI: 10.1119/1/4772632.

83 MARTINS, T. T.; KAMIZAK, L. P.; MUNIZ, S. R. Thermodynamic measurement of non-equilibrium stochastic processes in optical tweezers. DOI: 10.48550/arXiv.2209.05606.

84 ROSALES-CABARA, Y. *et al.* Optimal protocols and universal time-energy bound in brownian thermodynamics. **Physical Review Research**, American Physical Society, v. 2, p. 012012, Jan 2020. DOI: 10.1103/PhysRevResearch.2.012012.

85 CARTER, A. R. *et al.* Stabilization of an optical microscope to 0.1 nm in three dimensions. **Applied Optics**, v. 46, n. 3, p. 421–427, 2007.

86 MOUE, A. S. The thought experiment of maxwell's demon and the origin of irreversibility. **Journal for General Philosophy of Science**, v. 39, n. 1, p. 69–84, 2008.

87 MAXWELL, J. C.; PESIC, P. **Theory of heat**. New York: Courier Corporation, 2001.

88 LUTZ, E.; CILIBERTO, S. Information: from Maxwell's demon to Landauer's eraser. **Physics Today**, v. 68, n. 9, p. 30–35, 2015. DOI: 10.1063/PT.3.2912.

89 SZILARD, L. On the decrease of entropy in a thermodynamic system by the intervention of intelligent beings. **Behavioral Science**, Wiley Online Library, v. 9, n. 4, p. 301–310, 1964.

90 PARRONDO, J. M.; HOROWITZ, J. M.; SAGAWA, T. Thermodynamics of information. **Nature Physics**, v. 11, n. 2, p. 131–139, 2015.

91 LANDAUER, R. Irreversibility and heat generation in the computing process. **IBM Journal of Research and Development**, IBM, v. 5, n. 3, p. 183–191, 1961.

92 JAYNES, E. T. *et al.* Gibbs vs boltzmann entropies. **American Journal of Physics**, v. 33, n. 5, p. 391–398, 1965.

93 KOSKI, J. V. *et al.* On-chip maxwell's demon as an information-powered refrigerator. **Physical Review Letters**, v. 115, n. 26, p. 260602, 2015. DOI:10.1103/PhysRevLett.115.260602.

94 SAGAWA, T.; UEDA, M. Generalized jarzynski equality under nonequilibrium feedback control. **Physical Review Letters**, v. 104, n. 9, p. 090602, 2010.

95 SHU, Y. *et al.* Quantum dots for display applications. **Angewandte Chemie**, v. 132, n. 50, p. 22496–22507, 2020.

96 CHEN, H.; HE, J.; WU, S.-T. Recent advances on quantum-dot-enhanced liquid-crystal displays. **IEEE Journal of Selected Topics in Quantum Electronics**, v. 23, n. 5, p. 1–11, 2017.

97 FRECKER, T. *et al.* Quantum dots and their application in lighting, displays, and biology. **ECS Journal of Solid State Science and Technology**, v. 5, n. 1, p. R3019–R30312015, 2015. DOI: 10.1149/2.003160jss.

98 SEMONIN, O. E.; LUTHER, J. M.; BEARD, M. C. Quantum dots for next-generation photovoltaics. **Materials Today**, v. 15, n. 11, p. 508–515, 2012.

99 CONIBEER, G. *et al.* Silicon quantum dot nanostructures for tandem photovoltaic cells. **Thin Solid Films**, v. 516, n. 20, p. 6748–6756, 2008.

100 SUTHERLAND, A. J. Quantum dots as luminescent probes in biological systems. **Current Opinion in Solid State and Materials Science**, v. 6, n. 4, p. 365–370, 2002.

101 LOSS, D.; DIVINCENZO, D. P. Quantum computation with quantum dots. **Physical Review A**, v. 57, n. 1, p. 120, 1998. DOI:10.1103/PhysRevA.57.120.

102 KLOEFFEL, C.; LOSS, D. Prospects for spin-based quantum computing in quantum dots. **Annual Review Condensed Matter Physics**, v. 4, n. 1, p. 51–81, 2013.

103 BURKARD, G.; ENGEL, H.-A.; LOSS, D. Spintronics and quantum dots for quantum computing and quantum communication. **Fortschritte der Physik:** progress of physics, v. 48, n. 9-11, p. 965–986, 2000.

104 KRENNER, H. J. *et al.* Recent advances in exciton-based quantum information processing in quantum dot nanostructures. **New Journal of Physics**, v. 7, n. 1, p. 184, 2005. DOI:10.1088/1367-2630/7/1/184.

105 IMAMOG, A. *et al.* Quantum information processing using quantum dot spins and cavity QED. **Physical Review Letters**, v. 83, n. 20, p. 4204, 1999. DOI:10.1103/PhysRevLett.83.4204.

106 GAZZANO, O.; SOLOMON, G. S. Toward optical quantum information processing with quantum dots coupled to microstructures. **Journal of Optical Society of America B**, v. 33, n. 7, p. C160–C175, 2016.

107 YAMAMOTO, Y. Quantum communication and information processing with quantum dots. **Quantum Information Processing**, v. 5, p. 299–311, 2006.

108 EFROS, A. L.; BRUS, L. E. Nanocrystal quantum dots: from discovery to modern development. **ACS Nano**, ACS Publications, v. 15, n. 4, p. 6192–6210, 2021.

109 KORTAN, A. *et al.* Nucleation and growth of cdse on zns quantum crystallite seeds, and vice versa, in inverse micelle media. **Journal of the American Chemical Society**, ACS Publications, v. 112, n. 4, p. 1327–1332, 1990.

110 MURRAY, C.; NORRIS, D. J.; BAWENDI, M. G. Synthesis and characterization of nearly monodisperse cde (e= sulfur, selenium, tellurium) semiconductor nanocrystallites. **Journal of the American Chemical Society**, ACS Publications, v. 115, n. 19, p. 8706–8715, 1993.

111 JEONG, B. G. *et al.* Colloidal spherical quantum wells with near-unity photoluminescence quantum yield and suppressed blinking. **Acs Nano**, v. 10, n. 10, p. 9297–9305, 2016.

112 DICKE, R. H. Coherence in spontaneous radiation processes. **Physical Review**, APS, v. 93, n. 1, p. 99, 1954.

113 GROSS, M.; HAROCHE, S. Superradiance: An essay on the theory of collective spontaneous emission. **Physics Reports**, Elsevier, v. 93, n. 5, p. 301–396, 1982.

114 RAINÒ, G. *et al.* Superfluorescence from lead halide perovskite quantum dot superlattices. **Nature**, Nature Publishing Group UK London, v. 563, n. 7733, p. 671–675, 2018.

115 BILIROGLU, M. *et al.* Room-temperature superfluorescence in hybrid perovskites and its origins. **Nature Photonics**, Nature Publishing Group UK London, v. 16, n. 4, p. 324–329, 2022.

116 ALLEMAND, A. *et al.* Optical properties of individual cds/cdse/cds nanocrystals: spherical quantum wells as single-photon sources. **Nanotechnology**, IOP Publishing, v. 33, n. 27, p. 275703, 2022. DOI. 10.1088/1361-6528/ac5ee3.

117 PADDING, J.; LOUIS, A. Hydrodynamic interactions and brownian forces in colloidal suspensions: Coarse-graining over time and length scales. **Physical Review E**, APS, v. 74, n. 3, p. 031402, 2006.

118 DENG, R. *et al.* Measuring pure water absorption coefficient in the near-infrared spectrum(900–2500 nm). **Yaogan Xuebao - Journal of Remote Sensing**, Kexue Chubanshe, v. 16, n. 1, p. 192–206, 2012.

APPENDIX

APPENDIX A – PROTOCOL'S STARTING POINT

To apply the protocols described in Chapters 4, 5, and 6, one controls the trapping laser intensity, as shown in Fig. 58. However, when a given output signal is applied in the RF driver, the control and the reading of the QPD and PD show a delay between them. Consequently, the data acquisition does not start at the beginning of a given protocol. The identification of the starting point requires analyses of the trapping laser's PD voltage signal, $V_{PD,j}$, for $j = 0, 1, 2, \ldots, N$ where N is the number of data acquisition points in a file.

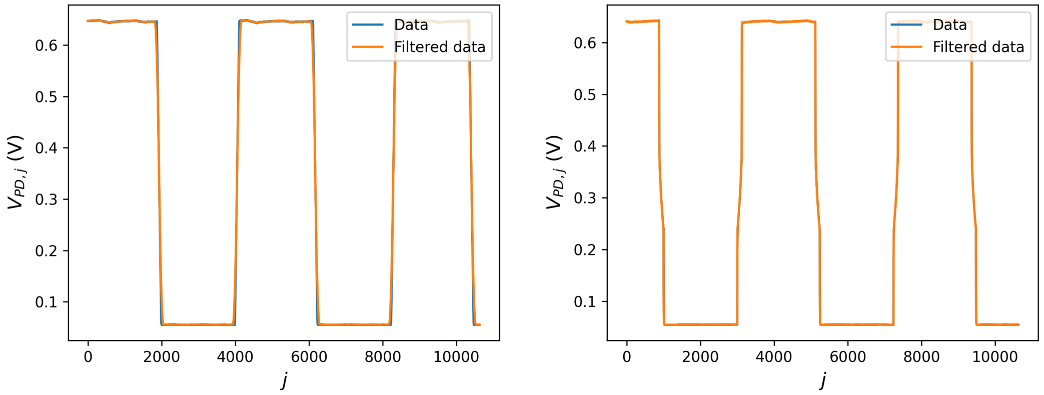

Figure 58 – Typical PD voltage signal (original one in blue and filtered one in orange) as a function of the sample number for linear (left) and optimal (right) protocols with $\tau_{eq} = 20$ ms, $\lambda_i = 1.5$ $pN/\mu m$, $\Delta\lambda = 10\lambda_i$ and $\tau_P = 0.1\tau_R$, where $\tau_R = \gamma/\lambda_i \approx 12$ ms is the relaxation time in the state λ_i.
Source: By the author.

The procedure consists of the application of a filter[*] to make the signal less noisy, as shown in Fig. 58, and the computation of the differential value of the PD voltage signal given by $V_{PD,j+1} - V_{PD,j}$. The peaks shown in Fig. 59 represent the linear protocols' middle points and the optimal protocols' starting points. Positive peaks are related to forward processes (compressing) and negative ones refer to reverse processes (expansion).

---

[*] It was used the Python function *scipy.signal.savgol_filter*.

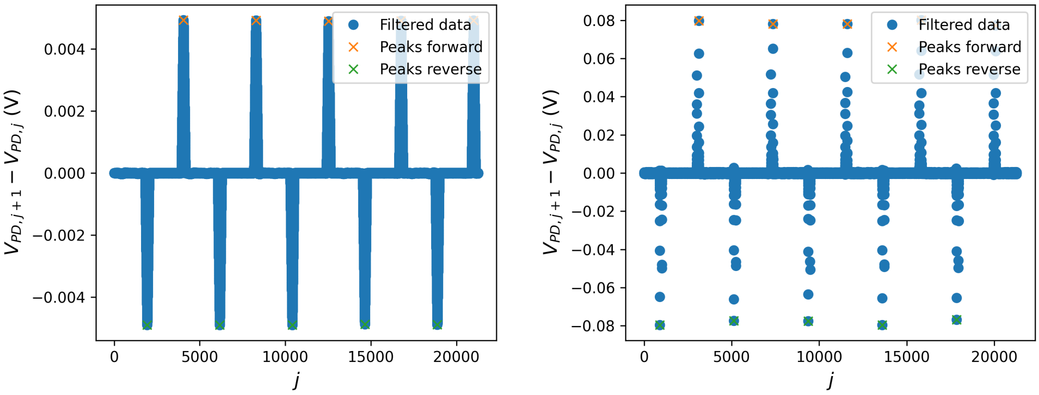

Figure 59 – Typical differential of the PD voltage signal for linear (left) and optimal (right) protocols as a function of sample number, with $\tau_{eq} = 20$ ms, $\lambda_i = 1.5\ pN/\mu m$, $\Delta\lambda = 10\lambda_i$ and $\tau_P = 0.1\tau_R$, where $\tau_R = \gamma/\lambda_i \approx 12$ ms is the relaxation time in the state λ_i. The peaks corresponding to the identification of the forward process are crossed in orange, and the reverse processes are crossed in green.

Source: By the author.

APPENDIX B – CHARACTERIZATION OF THE SYSTEM'S NOISE

The setup IFSC-USP has undergone several improvements over the years, as described in more detail in Chapter 8. Despite the efforts to minimise high-frequency noise, it has not been eliminated. Towards using the system in spite of unwanted effects, a digital low-pass filter was implemented in the outputs of the QPD at a 3 kHz cutoff frequency*. Figure 60 (left) shows the original and the filtered PSDs for x_{QPD}, demonstrating data below the cutoff frequency remain unchanged. Despite its simplicity, the measure is efficient and makes the signal cleaner, minimizing contributions from noise in the apparent displacement of the particle, as depicted in the histograms of Fig. 60 (right).

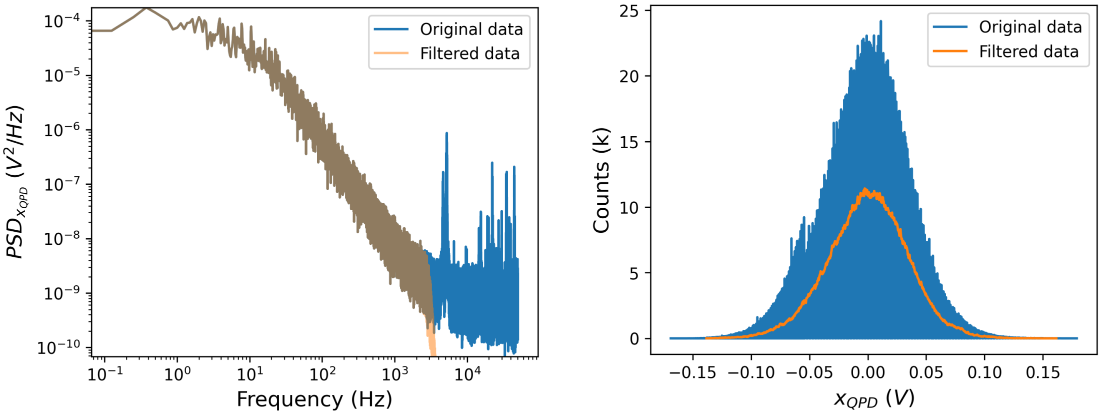

Figure 60 – Typical PSD (left) and position histogram with 1000 bins (right) for original data in blue and filtered data in orange. Measuring time is $t = 30$ s and data were acquired at a $f = 100$ kHz acquisition rate for a 2 μm silica trapped particle.

Source: By the author.

Since that noise is far from the corner frequency, the calibration of the optical potential is not affected and a linear dependence of the force constant on the PD reading (proportional to the trapping laser's intensity) is observed, as shown in Fig. 61 (left) and discussed in Sec. 3.2.4. However, the resulting curve for the amplification factor, depicted in Fig. 61 (right), is different from the one presented in Sec. 3.2.5, possibly due to differences in the alignment of the detection laser relative to the trapping one.

---

* The filter was implemented during the post-acquisition processing by the *scipy.signal.butter* function in Python.

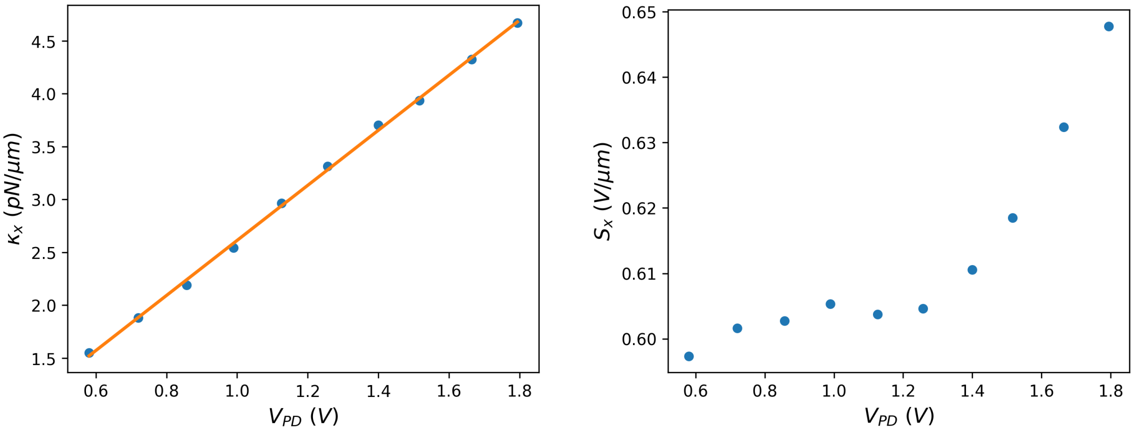

Figure 61 – Calibration curves for trap stiffness (right) and amplification factor (left) from PSD fits. The angular coefficient is $m_{TS} = 2.60 \pm 0.03$ (pN/μm)/V and y-intercept is $b_{TS} = 0.01 \pm 0.04$ pN/μm for the trap stiffness calibration. The average of 10 files was calculated from PSD curves, and the interval 0 Hz $< f <$ 2 kHz was used for the fit.

Source: By the author.

APPENDIX C – MECHANICAL DISPLACEMENT IN THE TRAP

The two-sided* power spectrum density (PSD) for displacement x is calculated as follows:

$$\mathrm{PSD}_x(\omega) = \lim_{T_m \to +\infty} \frac{\langle |\tilde{x}_{T_m}(\omega)|^2 \rangle}{T_m}, \tag{C.1}$$

where T_m represents theoretical measurement time and $\tilde{x}_{T_m}$ is the Fourier transform of $x_{T_m}(t) = x(t)\mathrm{rect}(2t/T_m)$, with

$$\mathrm{rect}(2t/T_m) = \begin{cases} 1, & \text{if } |t| < T_m/2 \\ 0, & \text{otherwise} \end{cases}. \tag{C.2}$$

Computing the Fourier transform of the particle position on $\omega = 2\pi f$, here denoted as $\mathrm{FT}[f](\omega) = \int_{-\infty}^{+\infty} dt f(t) \mathrm{e}^{-i\omega t}$, gives

$$\tilde{x}_{T_m}(\omega) = \mathrm{FT}\left[x(t)\mathrm{rect}(2t/T_m)\right](\omega) = \frac{1}{2\pi}\left(\tilde{x}(\omega) * T_m \mathrm{sinc}_\pi\left(\frac{\omega T_m}{2\pi}\right)\right). \tag{C.3}$$

Now, computing the Fourier transform of the Langevin equation (Eq. 7.6) results in

$$\begin{aligned} -\omega^2 m_p \tilde{x}(\omega) &= -k\tilde{x}(\omega) - i\omega\tilde{\gamma}(\omega)\tilde{x}(\omega) + \tilde{F}_{\mathrm{th}}(\omega) + \tilde{F}_{\mathrm{mod}}(\omega) + \tilde{F}_{\mathrm{opt}}(\omega) && \text{(C.4)} \\ \tilde{x}(\omega) &= \chi(\omega)\left(\tilde{F}_{\mathrm{th}}(\omega) + \tilde{F}_{\mathrm{mod}}(\omega) + \tilde{F}_{\mathrm{opt}}(\omega)\right), && \text{(C.5)} \end{aligned}$$

where the susceptibility is given by Eq. 2.20.

For the calibration force, one has:

$$\tilde{F}_{\mathrm{mod}}(\omega) = F_m \int_{-\infty}^{+\infty} dt\, \sin(2\pi f_m t)\mathrm{e}^{-i\omega t} = -i\pi F_m\left(\delta(\omega - 2\pi f_m) - \delta(\omega + 2\pi f_m)\right), \tag{C.6}$$

and for the optical force,

$$\tilde{F}_{\mathrm{opt}}(\omega) = F_p\, \mathrm{FT}\left[\mathrm{rect}_\tau\right](\omega)\, \mathrm{FT}\left[\mathrm{comb}_T\right](\omega) = F_p \tau \mathrm{sinc}_\pi\left(\frac{\omega\tau}{2\pi}\right)\frac{2\pi}{T}\mathrm{comb}_{\frac{2\pi}{T}}(\omega). \tag{C.7}$$

Therefore, $\tilde{x}_{T_m}(\omega)$ can be expressed as the sum of three terms:

$$\tilde{x}_{T_m}(\omega) = A + B + C, \tag{C.8}$$

where A is the contribution of the stochastic force:

$$A = \chi(\omega)\tilde{F}_{\mathrm{th}}(\omega) * \frac{T_m}{2\pi}\mathrm{sinc}_\pi\left(\frac{\omega T_m}{2\pi}\right), \tag{C.9}$$

---

[*] A two-sided PSD has both positive and negative frequencies and exhibits equal energy on each side.

B is the contribution of the modulation force:

$$\begin{aligned} B &= \chi(\omega)\tilde{F}_{\text{mod}}(\omega) * \frac{T_m}{2\pi}\text{sinc}_\pi(\frac{\omega T_m}{2\pi}) \\ &= -\frac{iF_m T_m}{2}\left(\chi(\omega_m)\text{sinc}_\pi(\frac{(\omega-\omega_m)T_m}{4\pi}) - \chi(-\omega_m)\text{sinc}_\pi(\frac{(\omega+\omega_m)T_m}{4\pi})\right), \end{aligned} \tag{C.10}$$

and C the optical force:

$$\begin{aligned} C &= \chi(\omega)\tilde{F}_{\text{opt}}(\omega) * \frac{T_m}{2\pi}\text{sinc}_\pi(\frac{\omega T_m}{2\pi}) \\ &= \frac{F_p \tau T_m}{T}\sum_{n=-\infty}^{+\infty}\chi(n2\pi/T)\text{sinc}_\pi(\frac{n\tau}{T})\text{sinc}_\pi(\frac{\omega T_m}{2\pi} - n\frac{T_m}{T}). \end{aligned} \tag{C.11}$$

The computation of the mean square displacement in the frequency domain is given by

$$\langle|\tilde{x}_{T_m}(\omega)|^2\rangle = \langle|A|^2\rangle + |B|^2 + |C|^2 + 2\text{Re}(BC^*) \tag{C.12}$$

since $\langle A\rangle = 0$ and the terms B and C are associated with deterministic forces.

Therefore, let us compute each term of Eq. C.12, starting with the first $\langle|A|^2\rangle$:

$$\langle|A(\omega)|^2\rangle \;=\; \langle|\int_{-\infty}^{+\infty} d\omega'\chi(\omega'-\omega)\tilde{F}_{\text{th}}(\omega'-\omega)\frac{T_m}{2\pi}\text{sinc}_\pi(\frac{\omega' T_m}{2\pi})|^2\rangle. \tag{C.13}$$

Since sinc_π goes to 0 for big values of ω', the main contribution to the integral is given for $\omega' \ll 2\pi/T_m$, which represents the resolution in the frequency domain for a measurement time T_m. Therefore, in the limit where $T_m \to +\infty$, the following approximation is valid:

$$\begin{aligned} \frac{\langle|A(\omega)|^2\rangle}{T_m} &\approx \frac{1}{T_m}|\chi(\omega)|^2\langle|\tilde{F}_{\text{th}}(\omega)|^2\rangle\left|\frac{T_m}{2\pi}\int_{-\infty}^{+\infty} d\omega'\text{sinc}_\pi(\frac{\omega' T_m}{2\pi})\right|^2 \\ &= \frac{1}{T_m}|\chi(\omega)|^2\langle|\tilde{F}_{\text{th}}(\omega)|^2\rangle. \end{aligned} \tag{C.14}$$

Considering the particle is in equilibrium in the trap at temperature T and the excitation and modulation forces are initially zero, then

$$\text{PSD}_x^{\text{eq}}(\omega) = -\frac{2k_B T}{\omega}\text{Im}\left(\tilde{\chi}(\omega)\right) \tag{C.15}$$

from the fluctuation-dissipation theorem (Eq. 3.13). Looking in the limit case where $T_m \to +\infty$,

$$\lim_{T_m\to+\infty}\frac{\langle|\tilde{F}_{\text{th}}(\omega)|^2\rangle}{T_m} = 2k_B T\text{Re}\left(\tilde{\gamma}(\omega)\right), \tag{C.16}$$

hence, Eq. C.15 becomes

$$\text{PSD}_x^{\text{eq}}(\omega) = 2k_B T|\chi(\omega)|^2\text{Re}\left(\tilde{\gamma}(\omega)\right). \tag{C.17}$$

The second term of Eq. C.12 gives

$$\begin{aligned}\frac{|B|^2}{T_m} = \frac{F_m^2 T_m}{4}\Big[&|\tilde{\chi}(\omega_m)|^2 \mathrm{sinc}_\pi^2(\frac{(\omega-\omega_m)T_m}{2\pi}) + |\tilde{\chi}(-\omega_m)|^2 \mathrm{sinc}_\pi^2(\frac{(\omega+\omega_m)T_m}{2\pi}) \\ &- 2\mathrm{Re}(\tilde{\chi}(\omega_m)\tilde{\chi}^*(-\omega_m))\,\mathrm{sinc}_\pi(\frac{(\omega-\omega_m)T_m}{2\pi})\,\mathrm{sinc}_\pi(\frac{(\omega+\omega_m)T_m}{2\pi})\Big].\end{aligned} \tag{C.18}$$

Neglecting the last term, since the overlap of the sinc_π functions is insignificant and focusing on the resonance, $\omega = \omega_m$, then

$$\frac{|B|^2}{T_m} = \frac{F_m^2 T_m}{4}|\tilde{\chi}(\omega_m)|^2. \tag{C.19}$$

The third term of Eq. C.12 is given by

$$\frac{|C|^2}{T_m} \approx \frac{F_p^2 \tau^2 T_m}{T^2}\sum_{n=-\infty}^{+\infty}|\chi(n2\pi/T)|^2 \mathrm{sinc}_\pi^2(\frac{n\tau}{T})\mathrm{sinc}_\pi^2(\frac{\omega T_m}{2\pi} - n\frac{T_m}{T}). \tag{C.20}$$

Here, the product of sinc_π functions related to frequencies different than $\omega_n = n\frac{2\pi}{T}$ was neglected. Looking specifically to the first resonance, $\omega_1 = 2\pi/T$, we have:

$$\frac{|C|^2}{T_m} \approx \frac{F_p^2 \tau^2 T_m}{T^2}|\chi(2\pi/T)|^2 \mathrm{sinc}_\pi^2(\frac{\tau}{T}). \tag{C.21}$$

The last term of Eq. C.12 can be neglected as long as the modulation and excitation frequencies are distant, i.e. $\forall n\, |\omega_m - \omega_n| \gg 2\pi/T_m$.

Finally, PSD can be expressed as

$$\begin{aligned}\mathrm{PSD}_x(\omega) \approx\ & 2|\chi(\omega)|^2 k_B T \mathrm{Re}\,(\tilde{\gamma}(\omega)) \\ &+ \lim_{T_m \to +\infty}\Bigg[\frac{F_m^2 T_m}{4}(|\tilde{\chi}(\omega_m)|^2 \mathrm{sinc}_\pi^2(\frac{(\omega-\omega_m)T_m}{2\pi}) + |\tilde{\chi}(-\omega_m)|^2 \mathrm{sinc}_\pi^2(\frac{(\omega+\omega_m)T_m}{2\pi})) \\ &+ \frac{F_p^2 \tau^2 T_m}{T^2}\sum_{n=-\infty}^{+\infty}|\chi(n2\pi/T)|^2 \mathrm{sinc}_\pi^2(\frac{n\tau}{T})\mathrm{sinc}_\pi^2(\frac{\omega T_m}{2\pi} - n\frac{T_m}{T})\Bigg].\end{aligned} \tag{C.22}$$

Passing Eq. C.22 to frequency dependecy and computing the averaged value of the PSD over the measured interval $I(f) = [f - 1/(2T_{\mathrm{exp}}), f + 1/(2T_{\mathrm{exp}})]$ lead to the one-sided spectrum:

$$\begin{aligned}\mathrm{PSD}_x^{exp}(f) &= \int_I df' \mathrm{PSD}_x(f') T_{\mathrm{exp}} \\ &= 4|\chi(f)|^2 k_B T \mathrm{Re}\,(\tilde{\gamma}(f)) \\ &+ T_{\mathrm{exp}}\frac{F_m^2}{2}|\chi(f_m)|^2 \mathbf{1}_{I(f_m)} \\ &+ T_{\mathrm{exp}}\frac{2F_p^2\tau^2}{T^2}\sum_{n=0}^{+\infty}|\chi(f_n)|^2 sinc_\pi^2(nf_n)\mathbf{1}_{I(f_n)}.\end{aligned} \tag{C.23}$$

since

$$\int_I df' \lim_{T_m \to +\infty} T_m \mathrm{sinc}_\pi^2(f'T_m) = 1, \tag{C.24}$$

and

$$\lim_{T_m \to +\infty} \frac{T_m}{2\pi} \mathrm{sinc}_\pi^2(\frac{(\omega - \omega_m)T_m}{2\pi}) = \delta(\omega - \omega_m) = \frac{1}{2\pi}\delta(f - f_m) \tag{C.25}$$

for long measurements.